

**Nanostructure based neuron degenerative disease biomarker detection and drug release**

by

**Chao Song**

A dissertation submitted to the graduate faculty  
in partial fulfillment of the requirements for the degree of

DOCTOR OF PHILOSOPHY

Major: Electrical and Computer Engineering

Program of Study Committee:

Long Que, Major Professor

Rana Biswas

David Jiles

Meng Lu

Gil Ben-Shlomo

The student author, whose presentation of the scholarship herein was approved by the program of study committee, is solely responsible for the content of this dissertation. The Graduate College will ensure this dissertation is globally accessible and will not permit alterations after a degree is conferred.

Iowa State University

Ames, Iowa

2019

Copyright © Chao Song, 2019. All rights reserved.

## TABLE OF CONTENTS

	Page
ACKNOWLEDGEMENT.....	iv
ABSTRACT .....	v
CHAPTER 1. INTRODUCTION.....	1
Alzheimer’s Disease.....	2
Current Literatures on Symptoms and Pathology Related to AD .....	3
Diagnostic Methods with Neuron Imaging MRI, PET, SPECT, Principles and Costs .....	6
Other Sensing Methods, including MEMS and Nanotechnology Sensors.....	14
Glaucoma.....	29
Current Literatures on Glaucoma: Age, Symptoms, Species and Medication .....	29
Diagnostic Method of Scanning Laser Tomography.....	31
Methods Involving Contact Lenses, Implantable Devices for Eye Pressure Measurement ..	35
Dissertation Organization .....	37
References .....	40
CHAPTER 2. RAPID MULTIPLEXED DETECTION OF BETA-AMYLOID AND TOTAL-TAU AS BIOMARKERS FOR ALZHEIMER'S DISEASE IN CEREBROSPINAL FLUID.....	44
Abstract.....	44
Introduction .....	44
Methods .....	46
Results .....	52
Discussion.....	58
References .....	59
CHAPTER 3. NANOPORE THIN FILM ENABLED OPTICAL PLATFORM FOR DRUG LOADING AND RELEASE.....	61
Abstract.....	61
Introduction .....	61
Materials and Methods .....	63
Results and Discussion.....	65
Conclusions .....	70
References .....	71
CHAPTER 4. A FLEXIBLE NANOPORE THIN FILM ENABLED DEVICE FOR PRESSURE SENSING AND DRUG RELEASE.....	72
Abstract.....	72
Introduction .....	72

Materials, Methods and Device Description .....	73
Experimental Results and Discussion .....	77
Summary.....	83
References .....	84
<b>CHAPTER 5. HIGH-RESOLUTION, FLEXIBLE, AND TRANSPARENT NANOPORE THIN FILM SENSOR ENABLED BY CASCADED FABRY–PEROT EFFECT .....</b>	<b>85</b>
Abstract.....	85
Introduction .....	85
Fabrication of pTF-nanopore Sensors.....	87
Operational Principle of the pTF-nanopore Sensor.....	88
Thick pTF Effect in a pTF-nanopore Sensor.....	89
Thin pTF Effect in a pTF-nanopore Sensor .....	91
Angle Sensing.....	92
Temperature Sensing .....	94
Summary.....	95
References .....	95
<b>CHAPTER 6. MULTIFUNCTIONAL SMART SOFT CONTACT LENS DEVICE ENABLED BY NANOPORE THIN FILM FOR GLAUCOMA DIAGNOSTICS AND IN SITU DRUG DELIVERY .....</b>	<b>97</b>
Abstract.....	97
Introduction .....	97
Contact Lens Device Description.....	100
Material and Methods.....	101
Chemicals and Materials .....	101
Optical Measurement for Biomarker.....	102
Florescence Images and Analysis.....	102
Results .....	103
Fabrication of Contact Lens and Characterization of Optical and Mechanical Properties .	103
In Vitro Detection of Biomarker in Artificial Tears by Means of the Novel Contact Lens	106
Drug Release .....	107
Ex Vivo Monitoring of Intraocular Pressure (IOP).....	109
IOP Sensors at the Central Region and Surrounding the Central Region on Contact Lens	112
Discussions and Conclusion.....	113
References .....	114
<b>CHAPTER 7. GENERAL CONCLUSIONS AND FUTURE WORK.....</b>	<b>117</b>

## ACKNOWLEDGEMENT

Foremost, my advisor Dr. Long Que deserves most credits for helping me complete this thesis. Dr. Long Que not only provides financial support for assisting me during my PhD period, but also offers continuous and insightful suggestions regarding my research projects. He always guides me with enthusiasm, great encouragement, timely response, extreme patience, and wide range of interdisciplinary knowledge. Working with him, I feel highly motivated, yet not stressful all the time. I am really lucky enough to have him as my PhD advisor.

I also want to express my appreciation to my committee members: Dr. Rana Biswas, Dr. David Jiles, Dr. Meng Lu, and Dr. Gil Ben-Shlomo, for their extremely suggestive comments on my research. And many thanks to Dr. Meng Lu, Dr. Liang Dong, Dr. Gil Ben-Shlomo for their kindness to allow me access equipment in their lab. Special thanks to Dr. Gil Ben-Shlomo for coaching me IOP measuring machine hand by hand.

Thanks to my fellow lab mates who I spend most of PhD time with, hanging out, doing sports and discussing research projects: Huawei Jiang, Qiugu Wang, Zhen Xu, Longju Liu, Yunfei zhao, Yuan He, Xiangchen Che, Shenmin Gong, Qiang Li, Xinran Wang, Yifei Wang, Yueyi Jiao, Junhao Zhu, Yuncong Chen, Jiayan Huo, Jikang Qu, Yang Tian, Le Wei, Zijian Zhao, Silu Feng, Renyuan Yang, Xiaoke Ding, Subin Mao, Jingjing Qian, Yu, Zhang, Bhuwan Kashyap from Iowa State University. Thanks for their invaluable advices and help in experiments.

I want to express thanks to Dr. Wai Leung and Mr. Max Noack in Microelectronic Research Center for training me with microfabrication and testing equipment.

I definitely owe thanks to my family.

## ABSTRACT

Neurodegenerative diseases have been becoming increasingly threatening to human life and living quality, especially to elderly people. Ideally, such diseases can be diagnosed using simple diagnostic methods and treated at their early stages using efficient drug delivery methods. Toward these goals, some new MEMS/microfluidic devices have been developed for diagnosing and treating these neurodegenerative diseases including Alzheimer's Disease and Glaucoma.

One focus of this thesis is the multiplexed monitoring of two promising biomarkers, beta-amyloid (A $\beta$ 42) and total tau (T-tau), in both buffer and cerebrospinal fluid (CSF) for Alzheimer's disease (AD) using label-free optical nanosensors. It has been found that 7.8 pg/ml of A $\beta$ 42 in buffer and 15.6 pg/ml of T-tau in buffer can be readily detected with very good specificity. Based on our measurements, the purchased CSF itself contains A $\beta$ 42, whose concentration is estimated to be about 400 pg/ml. A $\beta$ 42 and T-tau in the mixtures of A $\beta$ 42 and T-tau spiked in CSF have been detected successfully, indicating the feasibility of the optical nanosensors to detect these biomarkers in clinical samples. For these measurements, only a small amount ( $\sim 1 \mu\text{l}$ ) of the samples is required. This type of sensor is suitable for point-of-care application to diagnose the AD due to its low cost and ease-of-operation.

The other focus of this thesis is to develop a new power-free multifunctional soft contact lens device that can measure intraocular pressure (IOP), achieve extended drug delivery *in situ*, and detect glaucoma biomarkers, all within the same device. Experiments demonstrate that the contact lens sensor can detect Interleukin 12p70, one possible biomarker for glaucoma, in a concentration as low as 2 pg/ml in artificial tears. The sustained drug release of the contact lens device can last up to 30 days. In *ex vivo* tests using cadaver pig eyes, the sensor can detect the IOP in a range of 10 to 50 mmHg.

## CHAPTER 1. INTRODUCTION

Worldwide, the elderly population is growing. Within the next 30 years, 30 percent or more of the population will be aged 60 or more, in Europe, Canada, Japan, China, Chile and many other regions all over the world, as shown in Fig. 1.1. In the US, the percentage of people age 65 or more is expected to reach 20 percent by 2030 [1]. Elderly people, whose contributions have made the world better, although living longer than before, are more likely to be affected by diseases, such as glaucoma, hypertension, Alzheimer's Disease (AD), Parkinson's disease (PD), Huntington's disease (HD), cardiac disease and cancers. Of these, glaucoma, AD, PD, and HD could be classified as neurodegenerative diseases, due to degeneration loss of functions, and death of neurons with aging. Neurodegeneration is the progressive loss of structure or function of neurons, including death of neurons. These diseases are usually incurable, leading to progressive degeneration and/or death of neurons. However, diagnosis and treatment of these diseases in their early stages could be critical to improve life for the elderly.

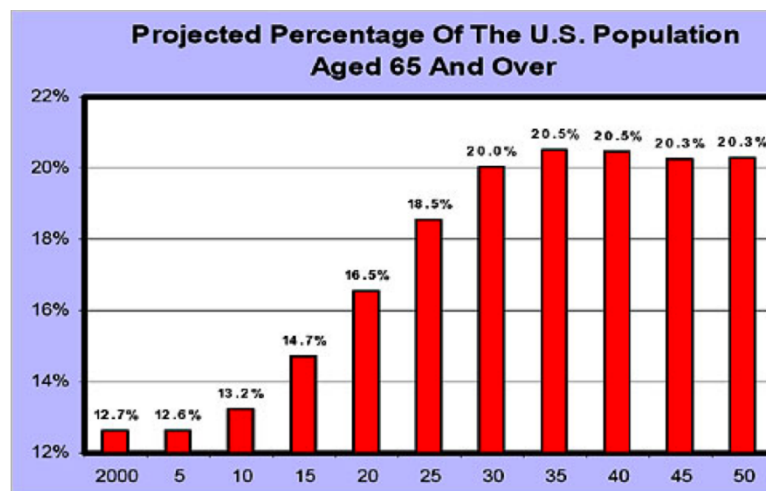


Fig. 1.1. World population of aged 65 or more is growing [1].

## Alzheimer's Disease

Alzheimer's disease, a chronic progressive neurodegenerative disease, is the most prevalent type of dementia. Its most common early symptom is short-term memory loss. As the disease progresses, symptoms including problems with language, disorientation (including the likelihood of getting lost), mood swings, loss of motivation, lack of managing self-care, and behavior issues may develop. According to the recent data, the number of cases of AD is increases annually. In 2015, an estimated 29.8 million people worldwide were afflicted with AD, and the number may be presumed to be approximately 100 million by 2050, as shown in Fig. 1.2a. Current diagnostic methods for AD are based on neuron imaging, as shown in Fig. 1.2b. They include MRI imaging, PET and SPECT [2], and are expensive and time consuming. The challenge for such methods is for increased sensitivity and specificity in the diagnosis of Alzheimer's disease. Other methods therefore are urgently needed for diagnosing AD, particularly in the early stages or before symptoms occur.

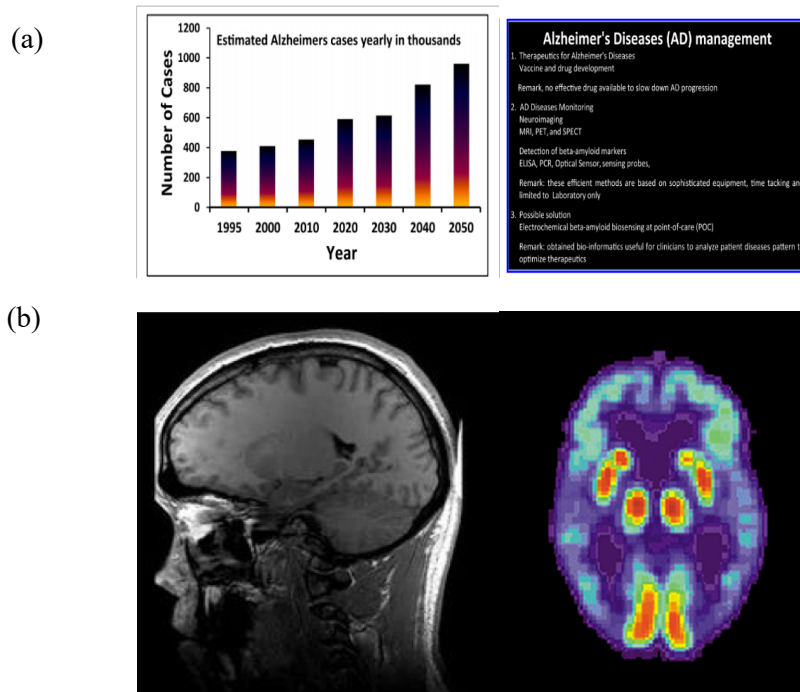


Fig. 1.2. (a) World's AD patients' number is growing; (b) MRI and PET image of human brain [2-3].

## **Current Literatures on Symptoms and Pathology Related to AD**

The death of neurons is an irreversible progress and even worse, no method can stop the loss of neurons by medication or surgery once AD is diagnosed. The early symptoms may include short term memory loss, followed by other symptoms already described. Such symptoms may occur unpredictably and cause serious problems for both patients themselves and their families. In numerous cases elderly people have gone missing or accidentally hurt themselves, as a result of undiagnosed Alzheimer's diseases. This makes early diagnosis of such diseases essential for managing patients before their symptoms become severe.

The inequality of distribution of dementia in six racial and ethnic groups in the U.S. has been studied to obtain data to support the work authorized by the National Alzheimer's Project Act (NAPA) for reducing racial/ethnic disparities [4]. Researchers from University of California, San Francisco (UCSF) studied dementia incidences from Jan 1, 2000 to Dec 31, 2013 and 25-year cumulative risk in a total of 274283 health care facility members, shown in Fig. 1.3. All cases are aged 64+, with population size varying for different races: 18778 African-American; 4543 American Indian/Alaska Native; 21000 Latino; 440 Pacific Islander; 206490 in white and 23032 Asian-Americans. The dementia incidence was highest among African-Americans at 26.6/1000 (person-years) and American Indian/Alaskan Natives at 22.2/1000 (person-years); medium for Latinos, at 19.6/1000 (person-years) and Pacific Islanders, at 19.6/1000 (person-years), and whites, at 19.3/1000 (person-years); and lowest for Asian-Americans, at 15.2/1000 (person-years). Thus, dementia incidence was 65% higher for the African-American group (95% confidence) than for the Asian-American group. The cumulative totals reveal that in every race/ethnic group, there is a 25 percent incidence of dementia eventually. Females were found to have a higher dementia incidence in all race/ethnic groups, indicating higher risk of dementia for females than for males.

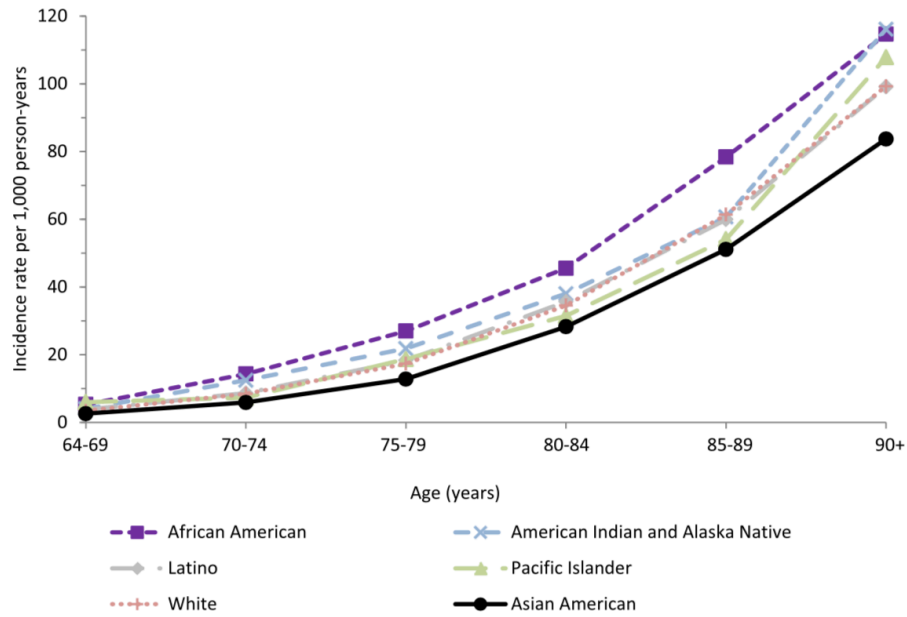


Fig. 1.3. Dementia incidence by race/ethnicity and sex [4].

Alzheimer's disease has been extensively studied in recent years to understand the disease producing mechanisms and potential ways to treat or cure this disease. The AD mechanisms have been well established; the main features of the disease are disfunction of neurons, loss of connections between neurons in close proximity, and subsequent death of neurons, as shown in Fig. 1.4. In the early stages of AD, these phenomena occur in the hippocampus and the entorhinal cortex, causing short term memory loss and mild cognitive impairment. As the disease progresses, an increased number of neurons and other parts of the brain are affected. Memory loss and cognitive impairment become more severe, and normal living can be seriously impaired. Death of neurons can finally spread through the entire brain, causing significant shrinkage of brain tissues. Following is a depiction of a healthy brain and a severely damaged brain, in which Alzheimer's disease has caused shrinkage brain compared to a healthy brain.

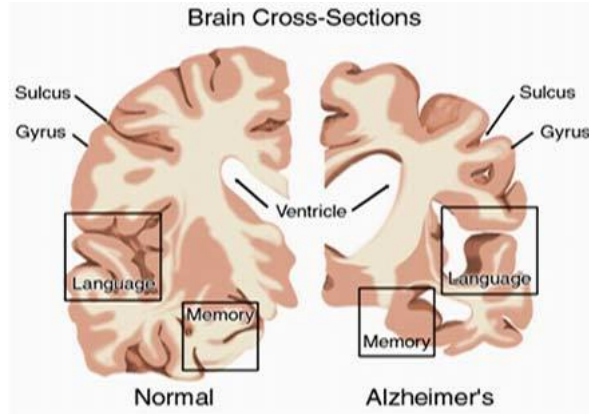


Fig. 1.4. Sketch showing brain cross-sections of healthy control and AD patient [2].

Neuron death is attributed mainly to deposition of  $A\beta_{42}$  protein fibril aggregates onto neurons, which can be observed during the progress of Alzheimer's disease. Three forms of  $A\beta_{42}$  protein exist in human cerebrospinal fluid: monomer, oligomer and fibrillar in composition. The monomer form of  $A\beta_{42}$  is dissolved in the cerebrospinal fluid, circulating in the system. The oligomer  $A\beta_{42}$  is the bonding form or crosslinked form of monomer  $A\beta_{42}$ , which can also be dissolved in cerebrospinal fluid and can potentially be crosslinked, forming insoluble fibrillar  $A\beta_{42}$ . The insoluble fibrillar  $A\beta_{42}$  deposited onto neurons, would disrupt connections between adjacent neurons. Once these connections are lost, neurons die, forming large areas of plaque in the brain. After formation of oligomers and fibrillar  $A\beta_{42}$ , the concentration of monomer  $A\beta_{42}$  in cerebrospinal fluid would thus be decreased.

A related phenomenon of AD is the significantly increased concentration of Ttau biomarker in cerebrospinal fluid and blood, as shown in Fig. 1.5. Ttau consists of proteins that could stabilize microtubules, existing mainly in neural cells of central nervous system. Ttau, like  $A\beta_{42}$ , is considered toxic to neurons under certain circumstances. The tau hypothesis proposes that excessive or abnormal phosphorylation of tau in cerebrospinal fluid may result in the transformation of normal adult tau into paired helical filament-tau and neurofibrillary tangles (NFT)

[5]. The accumulation of hyperphosphorylated tau in neurons is believed to lead to neurofibrillary degeneration [6]. Such tangles are toxic to cells, leading to cell death and cognitive decline. Tau could also be toxic to neurons by accumulation inside the cells, through a process involving enzyme stimulated phosphorylation of tau [7].

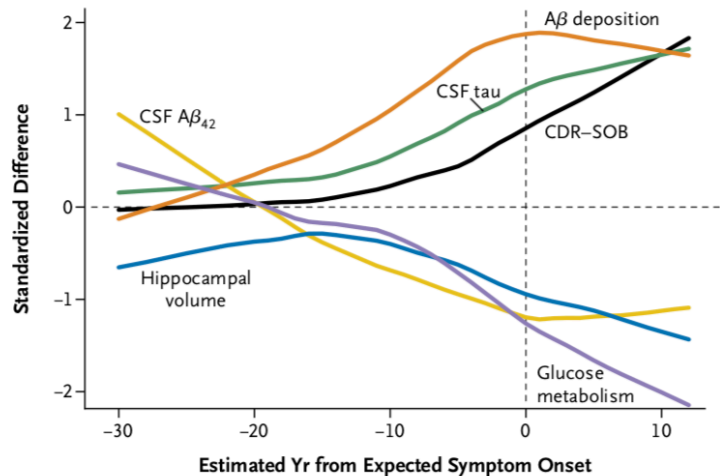


Fig. 1.5. Trending of related biomarkers and structural changes before AD symptoms onset [5].

### Diagnostic Methods with Neuron Imaging MRI, PET, SPECT, Principles and Costs

The most widely used diagnostic method for AD before development of neuron imaging methods was based on NINCDS-ARADA criteria, established by the National Institute of Neurological and Communicative Disorders and Stroke (NINCDS) and the Alzheimer's Disease and Related Disorders Association (ADRDA) in 1984 [8]. The following figure Fig. 1.6 shows criteria for clinical diagnosis of AD. The main goal is to identify dementia on the basis of these criteria and classify it as to the stage of Alzheimer's disease: PROBABLE, POSSIBLE, DEFINITE. In each stage, different symptoms are described as present or absent to support the presumed stage of Alzheimer's disease. The standard examination methods consist of the medical history; neurologic, psychiatric, and clinical examinations; neuropsychological tests; and laboratory tests. The criteria are imperfect as to specificity, as other neuron degenerative diseases or brain diseases

(HD, PD, manic-depressive disorder, brain tumors) may have symptoms similar to those of AD. To improve the specificity for diagnosis of AD, neuron imaging has been introduced into clinical practice as a means of further examination.

<p>I. The criteria for the clinical diagnosis of PROBABLE Alzheimer's disease include:</p> <p>dementia established by clinical examination and documented by the Mini-Mental Test,<sup>1</sup> Blessed Dementia Scale,<sup>2</sup> or some similar examination, and confirmed by neuropsychological tests;</p> <p>deficits in two or more areas of cognition;</p> <p>progressive worsening of memory and other cognitive functions;</p> <p>no disturbance of consciousness;</p> <p>onset between ages 40 and 90, most often after age 65; and</p> <p>absence of systemic disorders or other brain diseases that in and of themselves could account for the progressive deficits in memory and cognition.</p> <p>II. The diagnosis of PROBABLE Alzheimer's disease is supported by:</p> <p>progressive deterioration of specific cognitive functions such as language (aphasia), motor skills (apraxia), and perception (agnosia);</p> <p>impaired activities of daily living and altered patterns of behavior;</p> <p>family history of similar disorders, particularly if confirmed neuropathologically; and</p> <p>laboratory results of:</p> <p>normal lumbar puncture as evaluated by standard techniques,</p> <p>normal pattern or nonspecific changes in EEG, such as increased slow-wave activity, and</p> <p>evidence of cerebral atrophy on CT with progression documented by serial observation.</p> <p>III. Other clinical features consistent with the diagnosis of PROBABLE Alzheimer's disease, after exclusion of causes of dementia other than Alzheimer's disease, include:</p> <p>plateaus in the course of progression of the illness;</p> <p>associated symptoms of depression, insomnia, incontinence, delusions, illusions, hallucinations, catastrophic verbal, emotional, or physical outbursts, sexual disorders, and weight loss;</p>	<p>other neurologic abnormalities in some patients, especially with more advanced disease and including motor signs such as increased muscle tone, myoclonus, or gait disorder;</p> <p>seizures in advanced disease; and</p> <p>CT normal for age.</p> <p>IV. Features that make the diagnosis of PROBABLE Alzheimer's disease uncertain or unlikely include:</p> <p>sudden, apoplectic onset;</p> <p>focal neurologic findings such as hemiparesis, sensory loss, visual field deficits, and incoordination early in the course of the illness; and</p> <p>seizures or gait disturbances at the onset or very early in the course of the illness.</p> <p>V. Clinical diagnosis of POSSIBLE Alzheimer's disease:</p> <p>may be made on the basis of the dementia syndrome, in the absence of other neurologic, psychiatric, or systemic disorders sufficient to cause dementia, and in the presence of variations in the onset, in the presentation, or in the clinical course;</p> <p>may be made in the presence of a second systemic or brain disorder sufficient to produce dementia, which is not considered to be <i>the</i> cause of the dementia; and</p> <p>should be used in research studies when a single, gradually progressive severe cognitive deficit is identified in the absence of other identifiable cause.</p> <p>VI. Criteria for diagnosis of DEFINITE Alzheimer's disease are:</p> <p>the clinical criteria for probable Alzheimer's disease and</p> <p>histopathologic evidence obtained from a biopsy or autopsy.</p> <p>VII. Classification of Alzheimer's disease for research purposes should specify features that may differentiate subtypes of the disorder, such as:</p> <p>familial occurrence;</p> <p>onset before age of 65;</p> <p>presence of trisomy-21; and</p> <p>coexistence of other relevant conditions such as Parkinson's disease.</p>
---	--

Fig. 1.6. Criteria for clinical diagnosis of AD [8].

The current diagnostic method for AD consists of two parts: diagnosis of dementia, and specificity examination with neuron imaging. Neuron imaging includes magnetic resonance imaging, positron emission tomography and single photon emission computed tomography.

**Magnetic Resonance Imaging (MRI):** A typical MRI machine is shown in Fig. 1.7a. It can provide indirect but solid evidence to help doctors with the diagnosis of certain diseases. MRI is based on changes of proton spin state. Certain radio wave frequencies would be absorbed by protons under a uniform magnetic field stimulation, changing the spin state from one to a higher level. Certain radio frequencies would be emitted after proton spin transfer from the upper level state to the relaxation state. Such signals can be captured and processed by means of Fourier transforms to obtain an intensity profile across an entire tissue region with automated scanning, as shown in Fig. 1.7b. The final image can be reconstructed to obtain cross-sectional intensity, providing biological information useful in disease diagnosis. The detected signal frequency is related to applied magnetic field intensity, which polarizes proton spin. The density of protons in different areas of tissue cross-sections would lead to differences in the emitting signal intensity, generating contrast in the gray scale image. Knowing the proton distribution would significantly increase the ability to diagnose tissue and organ variations in the targeted sample. Following are sketches showing how static magnetic field and gradient magnetic field would affect the signal in the frequency domain. As shown, broadband signal frequency varies with magnetic field intensity, indicating information on different cross section positions.

An MRI image comparison of a healthy person and one with Alzheimer's disease is shown in Fig. 1.7c. The gray scale image shows a cross section of a human brain under the same MRI conditions. White/black color indicates density of protons in specific areas, with whiter areas meaning higher intensity and more protons. The black areas indicate many fewer protons compared with whiter areas, meaning less tissue. As shown, compared to the healthy control brain, much less tissue is seen in the Alzheimer's disease brain, which shows significant tissue shrinkage, resulting from massive death of neurons related to cognitive regions of the human brain.

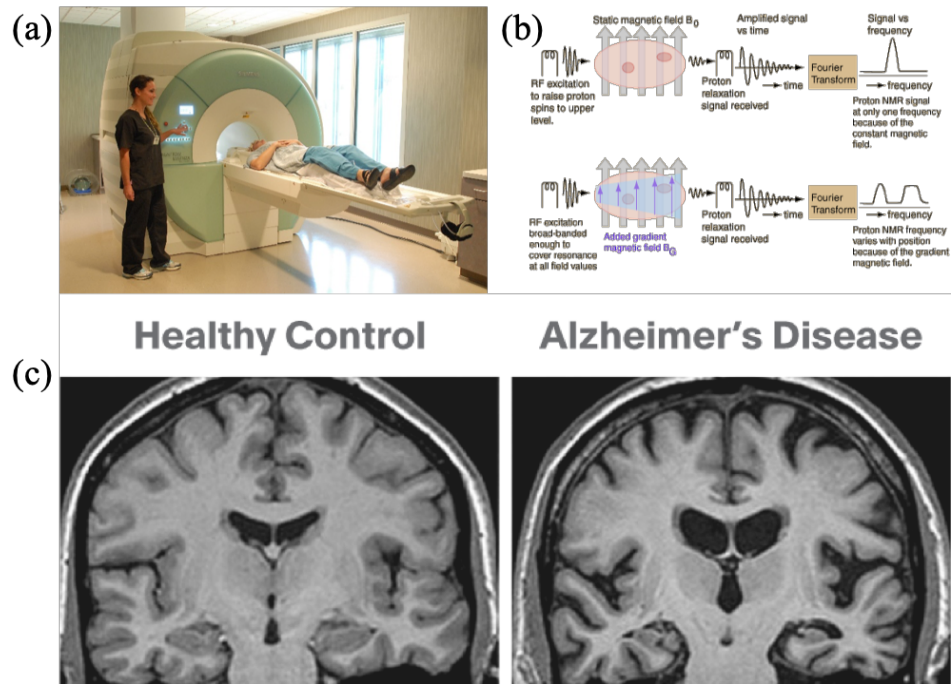


Fig. 1.7. (a) MRI machine; (b) principle of MRI; (c) MRI brain comparison of control and AD patient [9].

**Positron Emission Tomography (PET):** PET, imaging method for diagnosis of Alzheimer's disease, as shown in Fig. 1.8a, is based on detection of gamma rays from positron emission. When a positron collides with an electron in a low energy state, gamma rays are emitted. This method is usually used to observe metabolic activities in human tissues, especially related to glucose oxidation, as shown in Fig. 1.8b. To monitor metabolic activities related to glucose uptake, two molecules are required: a positron emitting radioligand which emits pairs of gamma rays, typically fluorine-18; and a radioactive tracer, typically fludeoxyglucose (FDG), which binds with radioligand to trace glucose. Intensity of gamma rays would reflect FDG concentration in a specific region, and the FDG concentration would indicate extent of glucose uptake, and thus the extent of metabolic activity in that specific region. The FDG tracer is commonly used to aid in the diagnosis of diseases of metabolic activities; cancer may be reflected by higher FDG concentration, whereas dementia, as Alzheimer's disease may be reflected by lower FDG concentration.

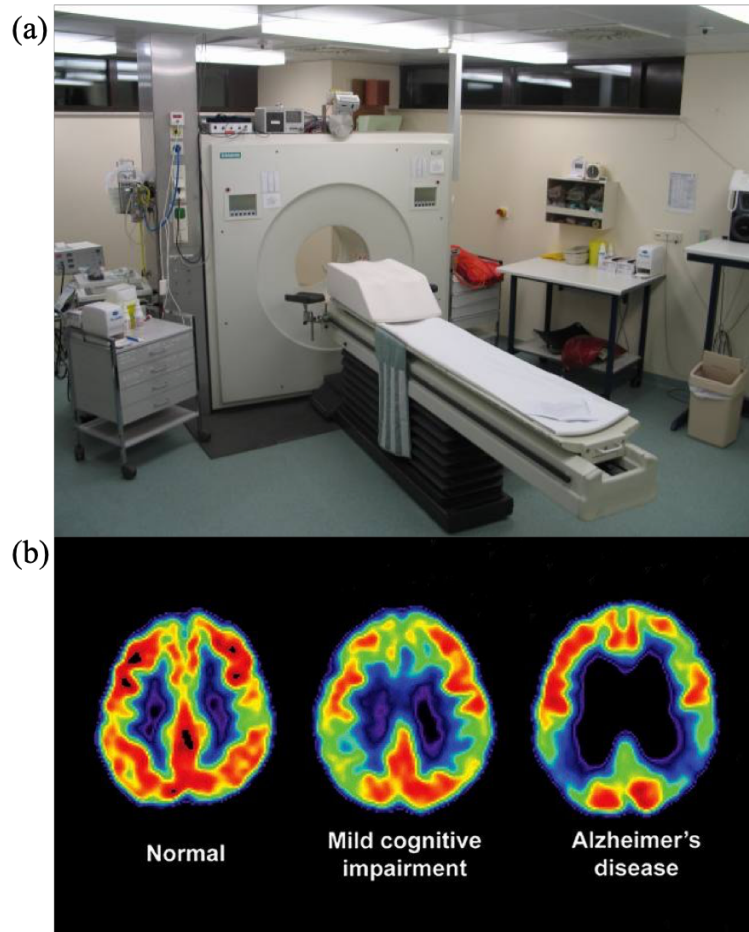


Fig. 1.8. (a) PET machine; (b) PET brain images comparison of Normal, MCI and AD patient [10].

The metabolic activities PET, although effective, is an indirect method of diagnosing disease. Different diseases may result in similar changes of metabolic activities, which compromises the specificity of such methods in diagnosing certain diseases. As more studies confirm the direct relationship of certain biomarkers with Alzheimer's disease in human brain tissue and cerebrospinal fluid, such as Ttau and  $A\beta_{42}$ , more advanced PET systems have been developed that directly reveal concentrations/distributions of such biomarkers in human brain tissue. Fig. 1.9 shows the Ttau PET signal and  $A\beta$  PET signal obtained with healthy human brains and the brains of Alzheimer's disease patients. The Ttau PET image indicates a much higher density of Ttau in Alzheimer's disease patients, compared with the density of Ttau in controls.  $A\beta$  PET images show

more A $\beta$ 42 deposition in brain tissue of AD patients than in healthy human brains. As already illustrated stated, A $\beta$  deposition in brain tissue would lead to loss of connections between neurons in close proximity and thus massive death of neurons, resulting in further shrinkage of brain tissue. The Ttau also becomes toxic to neurons and leads to their death.

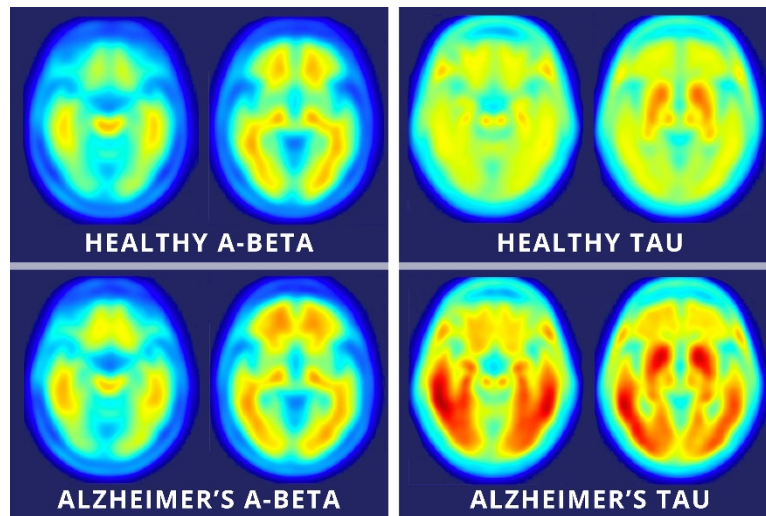


Fig. 1.9. A $\beta$  and Ttau PET images of control and AD patient [11].

**Single Photon Emission Computed Tomography (SPECT):** SPECT is similar to PET in that a radioactive ligand and molecule tracers are both used for generating emission of gamma rays, as shown in Fig. 1.10a. Detection of emitted gamma rays is also used in SPECT for generating computed images of tissues. However, SPECT is significantly different from PET in how the gamma rays are physically generated and in the number of dimensions the generated image may have. For PET, gamma rays are generated when positrons emitted by biological tracers annihilate with electrons. Two gamma photons of exact opposite directions would be, usually millimeters away. The detection of two photons in PET occur at the same time, making the spatial resolution around 1 cm. For SPECT, the gamma rays are directly emitted by the radioactive tracers, without any annihilation process involving electrons. Only one photon is generated in this emission process,

hence the name ‘single photon’. The disadvantage of SPECT compared with PET is its lower resolution. However, three advantages of SPECT are worth mentioning. A SPECT machine usually costs 400,000 to 600,000 in the US, while a PET machine may cost 2,000,000. Another advantage is that SPECT is much less expensive to operate than PET, mainly due to its use of an easily acquired radioactive tracer. The third advantage is its three-dimensional imaging capability, originating from its rotated scanning of targeted organs and 3D rebuilding image with powerful post processing. In Fig. 1.10a, SPECT machine is shown. Compared to PET and MRI machines, the SPECT machine has a rotation stage for acquiring images in different cross sections to build three-dimensional organ and tissue images. Fig. 1.10b shows SPECT images of Alzheimer’s disease patient brain and a patient suffering from depression. The AD brain shows shrunken tissues, which agrees with images obtained by MRI or PET.

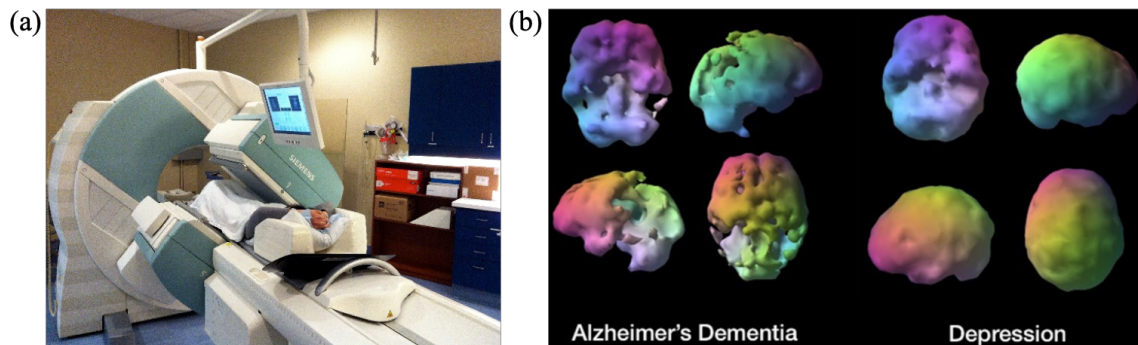


Fig. 1.10. (a) SPECT machine; (b) SPECT images of AD patient and Depression patient [12].

Neuron imaging methods are direct methods to aid in the diagnosis of diseases, but they are sophisticated and expensive. As mentioned, SPECT and PET machines may cost 400,000-600,000 and 2 million dollars, respectively. An MRI machine may cost from \$150,000 to millions of dollars, depending on how complicated the specific MRI machine is. For instance, a state-of-the-art 3 Tesla MRI machine would cost up to 3 million dollars. The extremely high cost of such machines and related equipment can result in high expenses for patients. An MRI usually costs 2600 dollars. For

a brain SPECT, the cost could be 1400 to 2800 dollars. PET costs average 3900 dollars for the brain, to 6700 dollars for the full body. Without insurance coverage, this would be a huge burden for people and their families.

Another disadvantage of neuron imaging is its inability to diagnose Alzheimer's disease early. Neuron imaging is usually the final step in confirming the doctor's diagnosis on the basis of the patients' symptoms, apparent in the late stages of Alzheimer's disease. For the wellbeing of patients, such diagnostic methods cannot provide enough preventive procedures to improve patients' better lives, since in the late stages of AD, all symptoms have appeared and brain damage has already occurred. Patients' normal lives have already largely disappeared and the patient may have to depend on external care, especially because there is no effective treatment to reverse the brain damage and mitigate the dementia symptoms. The early detection of AD therefore is particularly critical to help families to plan patients' future lives and take precautions regarding potential symptom-induced consequences (such as getting lost, injuring self by manipulating fire or electricity-based cooking equipment).

In addition, a neuron imaging method does not provide excellent specificity for diagnosing Alzheimer's disease, especially because other types of dementia (Pick's disease, Huntington's disease) may also cause death of neurons and brain tissue shrinkage. The Ttau and A $\beta$  PET is definitely an improvement over the glucose PET, but is a qualitative evaluation of Ttau or A $\beta$  distribution in brain. For instance, one limitation of A $\beta$ 42 is that it reflects only the density of A $\beta$  neuritic plaques in brain tissues. Further interpretation of A $\beta$  PET may take many other factors into consideration in making a conclusion, such as the individual patient's profile and A $\beta$  deposition caused by other forms of dementia.

To summarize, use of MRI and PET or SPECT for diagnosing Alzheimer's disease is just too

expensive, and performing such neuron imaging methods to further confirm diagnosis comes too late, since damage is already done and little or nothing can be done after diagnosis has been made. A real challenge is to increase the sensitivity and specificity of such methods in the diagnosis of Alzheimer's disease, since there are other diseases that also cause brain tissue damage. Other methods are therefore urgently needed to help in the diagnosis of AD, particularly at the early stage, before symptoms appear.

### **Other Sensing Methods, including MEMS and Nanotechnology Sensors**

Besides neuron imaging methods, other methods have been studied in an attempt to develop efficient and cost-effective yet dependable ways to help in the diagnosis of Alzheimer's disease, or mild cognitive impairment dementia. As research related to Alzheimer's disease goes deeper, other methods have indeed emerged for potential diagnosis of this disease in its early/preclinical stages. First things first: what is the early/preclinical AD stage?

In some papers [13-14], preclinical AD is defined as "The silent stage of AD-when the disease has begun in the brain, but symptoms are not yet clinically evident". The ultimate goal of diagnosing preclinical AD is to be able to apply some intervention at the preclinical stage, which may postpone or even eliminate the upcoming cognitive impairment that would occur if the condition were unattended. The preclinical AD stage could then be divided into three stages, based on different biomarker behavior and neuron imaging. Stage 1 should be characterized as A $\beta$ 42 PET results positive, while no neuron damage can be detected with MRI or FDG imaging. Stage 2 would be characterized as A $\beta$ 42 PET results positive and MRI neuron damage confirmed, although no cognitive damage is observed. In Stage 3, all results would be positive and mild cognitive impairment has occurred.

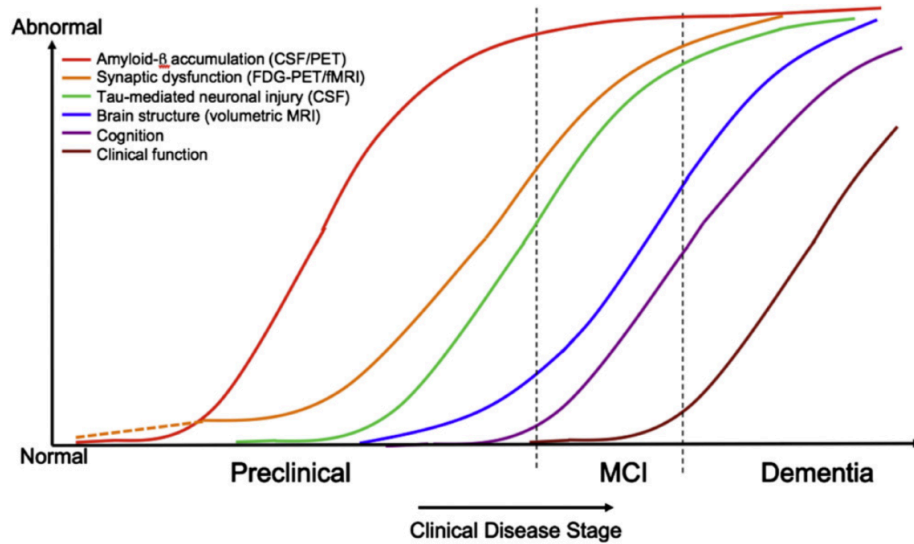


Fig. 1.11. Characteristics for AD stages [13-14].

Detailed information and standards for categorizing examination results in different stages are shown in Fig. 1.12. A $\beta$  PET result, markers of neuronal injury and evidence of subtle cognitive changes are qualitative indicators of disease progression. In combination, they could indicate the preclinical stages of AD.

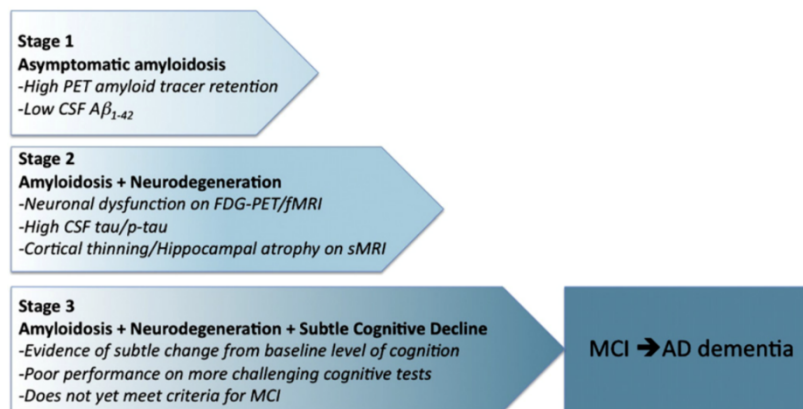


Fig. 1.12. Detailed illustration of each stage of preclinical AD [13-14].

In one study [15], functional near-infrared spectroscopy (fNIRS) was used to monitor changes in concentration of oxygenated hemoglobin (HbO), as shown in Fig. 1.13a. This optical method

accomplishes neuron imaging by utilizing energy of two wavelengths, 600nm/1000nm. Oxygenated hemoglobin and deoxygenated hemoglobin were the targeted chemicals because of their strong association with neuron metabolic activity in the cerebral cortex. Compared with MRI and PET, it has significant advantages with regard to high temporal resolution, low cost, non-invasive monitoring, good portability and low movement constraints. The measurements showed consistently significant reductions of HbO concentration in the targeted group, as shown in Fig. 1.13b. The decreased HbO concentration also agrees with the progress of disease severity from MCI to Alzheimer's Disease, indicating that fNIRS is a potential valuable tool for early detection of Alzheimer's disease and for monitoring the development of the disease.

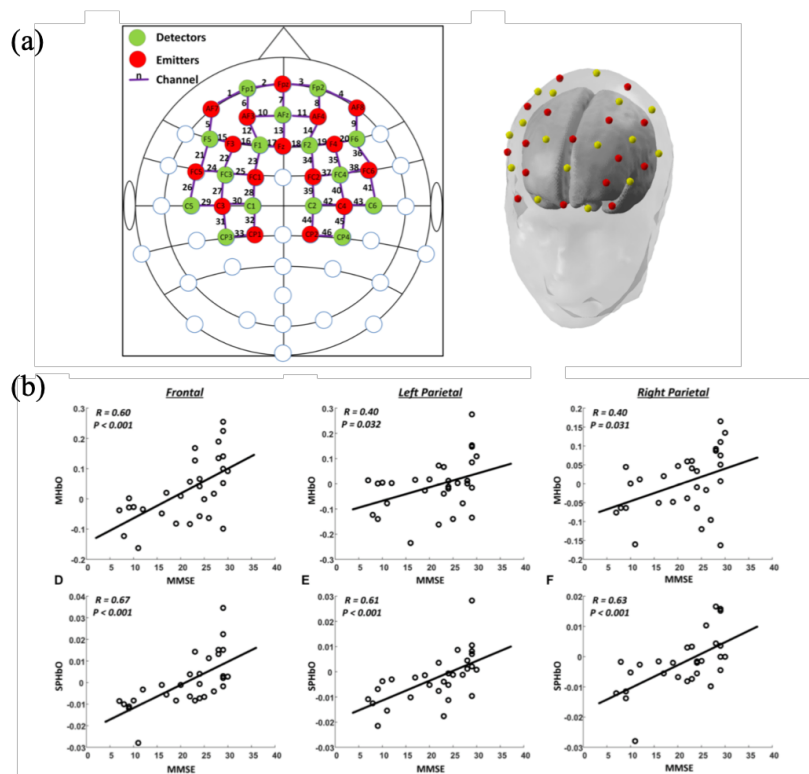


Fig. 1.13. (a) Graphical illustration of detectors and emitters distribution using fNIRS technology; (b) experimental results with fNIRS technology [15].

A strong correlation of the Ttau and A $\beta$ 42 biomarkers with AD has been revealed as more and more studies have provided evidence of the relationship [5], as shown in Fig. 1.14. The first

biomarker found to be related to Alzheimer's disease was A $\beta$ 42. In AD patients, in the brain plaque region where tissue was damaged, the fibril form of A $\beta$ 42 was heavily deposited in tissues. Further studies then showed that the fibril form A $\beta$ 42 was toxic to neurons by disrupting connections between adjacent cells. Lack of connections means further death of neurons. Further research indicates that the monomer form of the A $\beta$ 42 biomarker is normally dissolved in cerebrospinal fluid, circulating inside the brain and spinal fluid and changing to oligomer A $\beta$ 42 and fibrillar A $\beta$ 42 as the severity of AD increases. The fibrillar A $\beta$ 42, no longer soluble in cerebrospinal fluid, is aggregated and deposited onto surfaces of the brain. This causes death of neurons in the surface and shrinkage of brain tissues as the disease becomes more severe. The pathologies related to A $\beta$ 42 and dementia symptoms have been confirmed with MRI or A $\beta$ 42 PET, which have detected A $\beta$ 42 plaque areas in shrunken brain tissues.

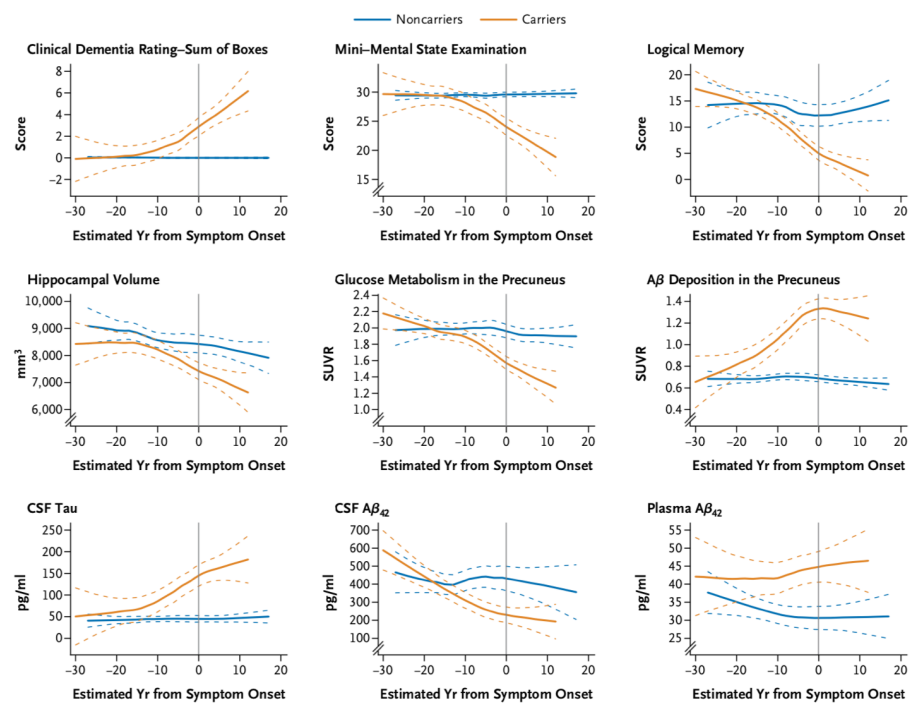


Fig. 1.14. Longitudinal study results of cross-sectional analyses of clinical, cognitive, structural, metabolic, and biochemical changes in mutation carriers versus noncarriers [5].

In another study, optical coherence tomography angiography was utilized for preclinical diagnosis of Alzheimer's disease [16], as shown in Fig. 1.15a. The goal was to investigate whether there is a correlation between retinal or microvascular anatomy abnormality and potential Alzheimer's disease. If such a correlation exists, examination of retinal or microvascular anatomy offers an alternative method of early diagnosis of Alzheimer's disease. The study included 32 participants; 58 eyes from 30 participants (62-92 years old) were selected for further analysis. All participants were cognitively normal and had no prior ophthalmic disease, media opacity, diabetes, or high intraocular pressure. The participants were considered potential AD cases if the A $\beta$ 42 biomarker examination was positive, meaning that PET revealed excessive A $\beta$ 42 deposition or lowered A $\beta$ 42 concentration in the CSF. Among the participants 14 were, on the basis of A $\beta$ 42 biomarkers, positive for AD and considered as having been diagnosed with preclinical AD; 16 were not biomarkers positive and were therefore considered a control group. The combined results with PET with OCT showed that the total foveal avascular zone area was significantly increased in the biomarker positive group compared with control group. In addition, the inner foveal thickness was decreased in the biomarker-positive group compared with control group, as shown in Fig. 1.15b. Findings indicated that individuals diagnosed as having preclinical AD (although cognitively normal) may have abnormal alternations of the retinal microvascular structure. This observation could provide ways of early AD diagnosis by performing ocular OCT, instead of more expensive neuron imaging methods like PET or MRI.

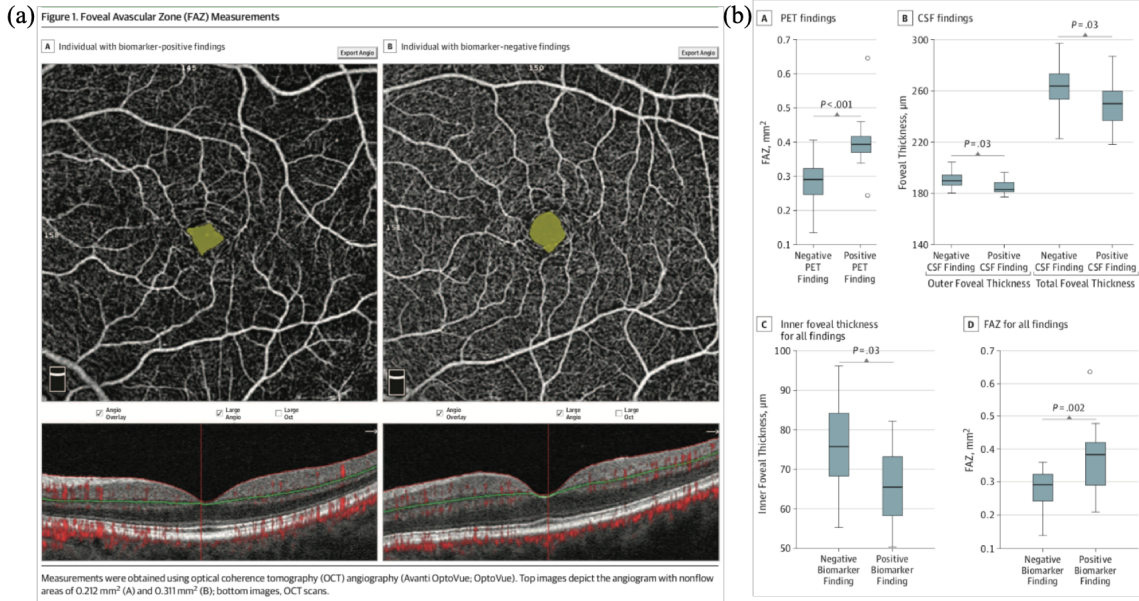


Fig. 1.15. (a) OCT results of FAZ for biomarker-positive and biomarker-negative people; (b) FAZ relationship with CSF biomarker results [16].

In the examples just described, the cerebrospinal fluid biomarker A $\beta$ 42 was usually identified as the monomer. The advantage of directly measuring the A $\beta$ 42 oligomer is that the oligomer form is more relevant as a cause of fibrillar A $\beta$ 42 deposition on human brain tissues. A potential obstacle to detect oligomer A $\beta$ 42 is its extremely low concentration in cerebrospinal fluid, which necessitates use of a highly sensitive method to detect it. A protein misfolding cyclic amplification technology was devised in this study, to amplify the oligomer concentration in cerebrospinal fluid [17], as shown in Fig. 1.16a. Oligomer A $\beta$ 42 concentrations as low as 0.3-8.4 fM were used as seed to induce massive monomer A $\beta$ 42 aggregation in the incubator and thus allow the detection of the minute amount of oligomer A $\beta$ 42 present. The polymerization process is critically influenced by temperature, pH, and peptide concentration, which means that precise control of these parameters is essential, as shown in Fig. 1.16b. The aggregation of A $\beta$ 42 is quantified by the fluorescence emission intensity of the amyloid-binding dye Thioflavin T (ThT); thus the relationship between oligomer A $\beta$ 42 concentration and fluorescence intensity is established, as

shown in Fig. 1.16c. One contradictory finding in this study was that the concentration of A $\beta$ 42 oligomer was higher in CSF from AD patients than in CSF from those in the healthy group, shown in Fig. 1.16d. The explanation of the authors was that since the A $\beta$ 42 oligomer is a very small proportion (1%) of the total A $\beta$ 42 biomarker in cerebrospinal fluid, it is possible that total A $\beta$ 42 concentration is decreased even as oligomer A $\beta$ 42 is increased. Therefore, simultaneous measurement of different forms of A $\beta$ 42 may be a more promising way to increase the specificity of diagnosis of Alzheimer's disease.

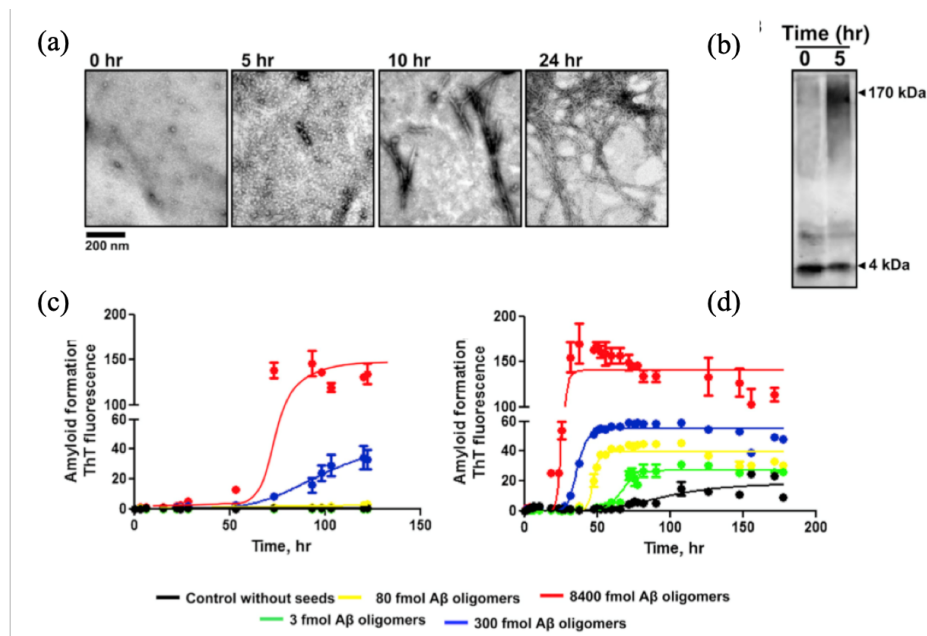


Fig. 1.16. (a) (b) Amyloid formation with time changing; (c) ThT fluorescence intensity change with reaction time; (d) ThT fluorescence intensity change with initial seeds concentration [17].

In addition to the A $\beta$ 42 and Ttau biomarkers, other biomarkers are under study to detect any correlation they have with Alzheimer's disease [18]. One such biomarker is neurofilament light chain (Nfl), a promising fluid biomarker that could indicate cerebral disease progressions. Concentrations of Nfl in both cerebrospinal fluid and serum were measured in the control group (non-carriers) and in potential AD patients (mutation carriers). A strong correlation is found of Nfl concentration in cerebrospinal fluid and in serum of the same participant, indicating that serum

Nfl concentration could reflect cerebrospinal fluid Nfl concentration. Also, transformation of the presymptomatic stage to the symptomatic stage (as early as 5 years before symptoms appear) leads to a peak rate change of the Nfl level in both serum and cerebrospinal fluid, which is confirmed by MRI at the same time, as shown in Fig. 1.17a-d. Such findings suggest that monitoring Nfl level makes it possible to predict AD symptoms and accomplish early diagnosis of AD. Another major contribution of this study is that it is a longitudinal study of participants over decades, providing progressive data and analysis for each stage of AD in the same patient. This is of real significance to providing early diagnosis and prediction of AD. The concentration in serum and cerebrospinal fluid is measured by single molecular array immunoassay technology (SIMOA, similar to the commercialized ELISA kit), which is based on bonding of antibody to antigen. The bonding is detected by light reading or fluorescence imaging equipment; Nfl concentrations in solutions are deduced on the basis of absorbed or emitted light intensities at certain wavelengths.

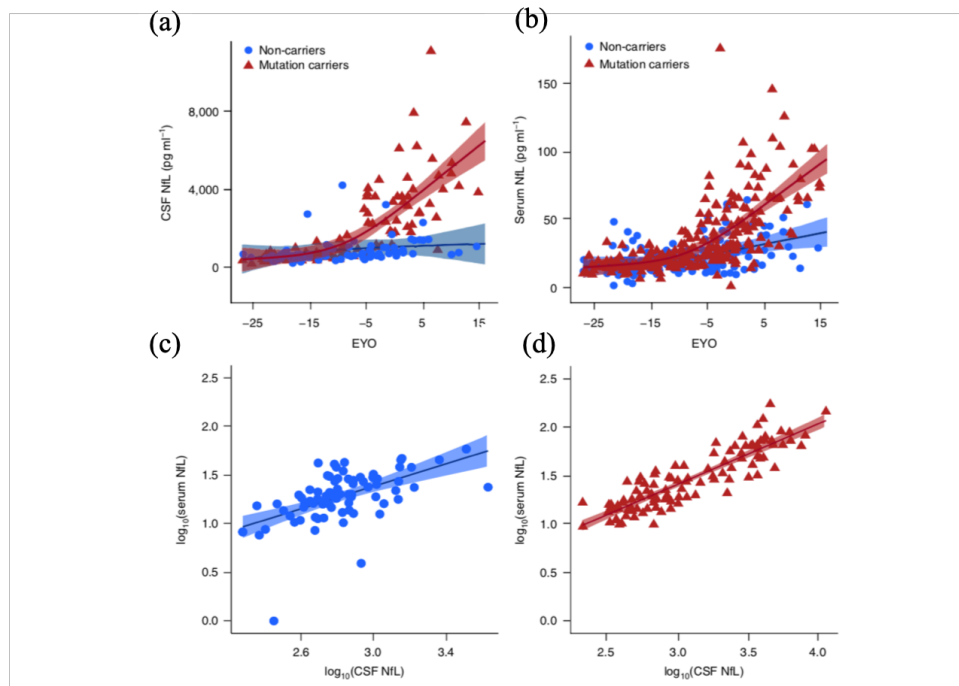


Fig. 1.17. (a) (b) CSF and serum values of NfL concentration in Non-carriers and Mutation carriers; (c) (d) strong relationship is shown for serum and CSF NfL concentration [18].

Another direction for achieving preclinical diagnosis of AD is development of cost effective and point-of-care MEMS devices of high specificity relative to other types of dementia, from the engineering perspective. Such MEMS devices should be capable of detecting biomarker concentrations in a reasonable range with sufficient sensitivity, achieving high specificity of the targeted biomarker relative to others, requiring no highly skilled personnel and expensive measuring equipment, being fabricated at much lower cost, and achieving continuous monitoring.

One example is silicon nanopillar based biosensors, which immobilize various antibodies onto nanopillar surfaces and quantify biomarker/antibody bonding by measuring fluorescence intensity, as shown in Fig. 1.18. With this sensor, the antibody with better specificity is filtered out [19].

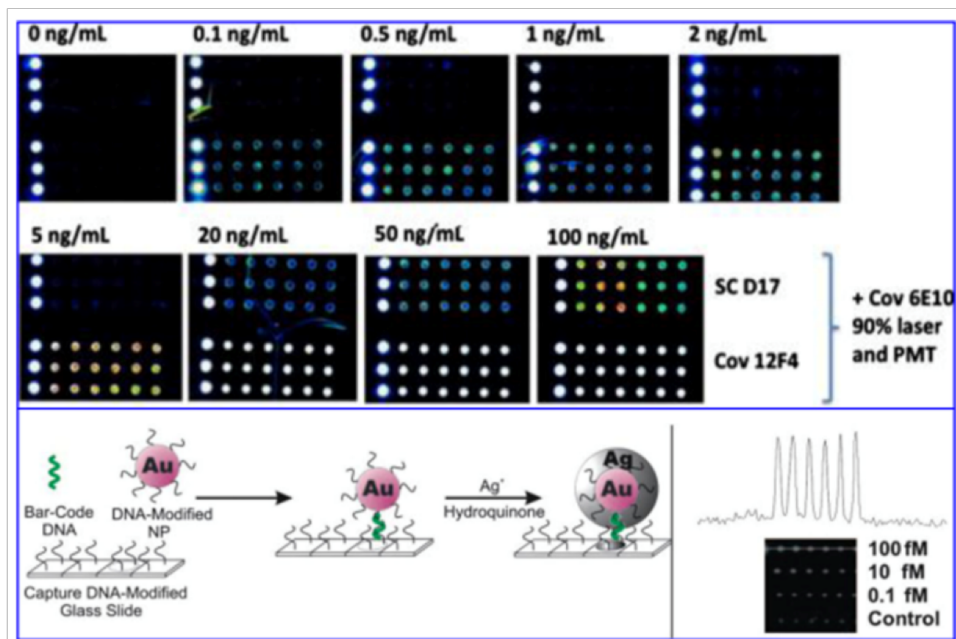


Fig. 1.18. Illustration of fluorescence intensity with different biomarker concentrations with silicon nanopillar sensing platform [19].

In another example, the biosensor is focused primarily on oligomer A $\beta$  (amyloid- $\beta$ -derived diffusible ligands, ADDLs) detection, because this allows for a more definitive diagnosis than detection of monomer A $\beta$  [20]. The minute concentration of A $\beta$  oligomer makes it difficult for ELISA to detect the pM level. A signal amplification process is therefore utilized in this work,

with use of a sandwich process with oligonucleotide-modified Au nanoparticles and magnetic microparticles, as shown in Fig. 1.19a-c. The keys to the increased sensitivity of this sensor are: (1) immobilization of both Au NPs and MMPs with the same antibody to the ADDL antigen; (2) release of hundreds of bar-code DNA strands as the target being detected. Using this approach, concentrations as low as 200 aM ADDL could be detected. The study shows that AD patients have higher a concentration of ADDL than the control group: above 0.5 fM in AD patients and below 0.5 fM in healthy control subjects.

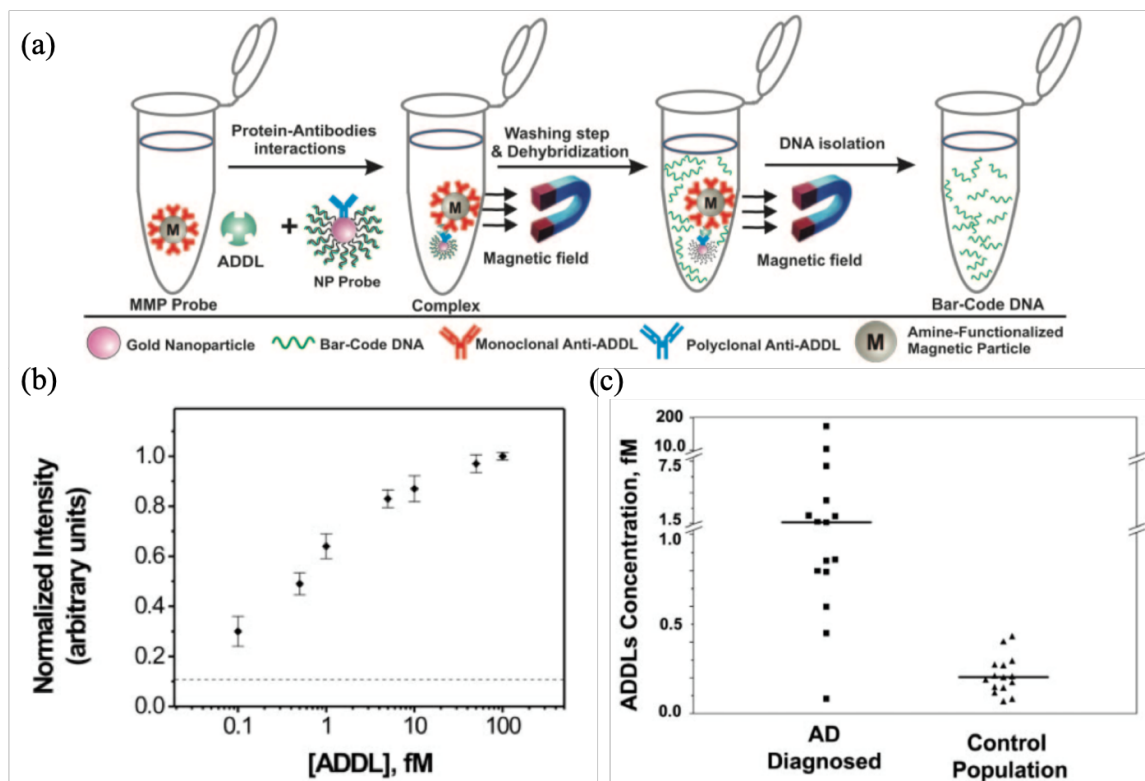


Fig. 1.19. (a) Amplification method of ADDLs; (b) Normalized intensity with respect to ADDL concentrations; (c) ADDLs concentration comparison of AD patient and healthy control [16].

In another study, SERS method was adopted to measure A $\beta$ 42 and Ttau dissolved in CSF. Results showed that much lower concentrations could be detected than with the ELISA kit (0.312 ng/ml for A $\beta$ 42, 0.15ng/ml for Ttau) [21]. The technology studied and utilized in this paper is called Core-Shell Nanoparticle Attached 2D Hybrid Graphene Oxide Based Multifunctional

Nanoplatfrom. The core-shell nanoparticle is very effective in enhancing Raman signal by generating electromagnetic field hot spot; graphene oxide can chemically enhance Raman signal by influencing aromatic molecule interaction and having a large surface area onto which it can attach. The nanoplatfrom is reported to show high sensitivity and to have a detection limit as low as 100 fg/ml for both A $\beta$ 42 and Ttau, shown in Fig. 1.20.

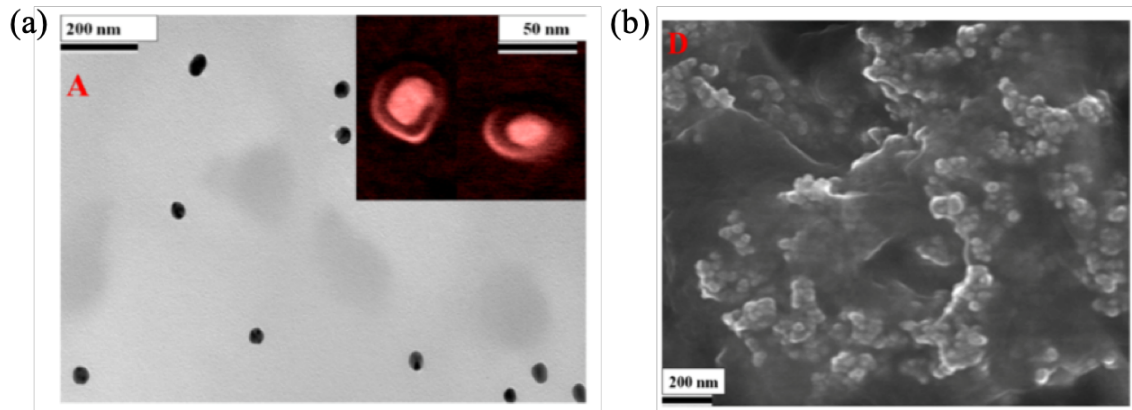


Fig. 1.20. Core-Shell structure characterization with SEM, Raman and Absorbance [21].

An optical LSPR biosensor was introduced later to measure the ADDL concentration in human brain extract and cerebrospinal fluids from both healthy controls and AD patients [22], as shown in Fig. 1.21a-b. LSPR, short for localized surface plasma resonance, usually leads to extraordinary light absorption or reflection at specific wavelengths. Such extraordinary light absorption or reflection results in a light intensity peak or dip in the broadband spectrum, which is highly dependent on the refractive index, shape, size and environmental conditions of the substrate material.

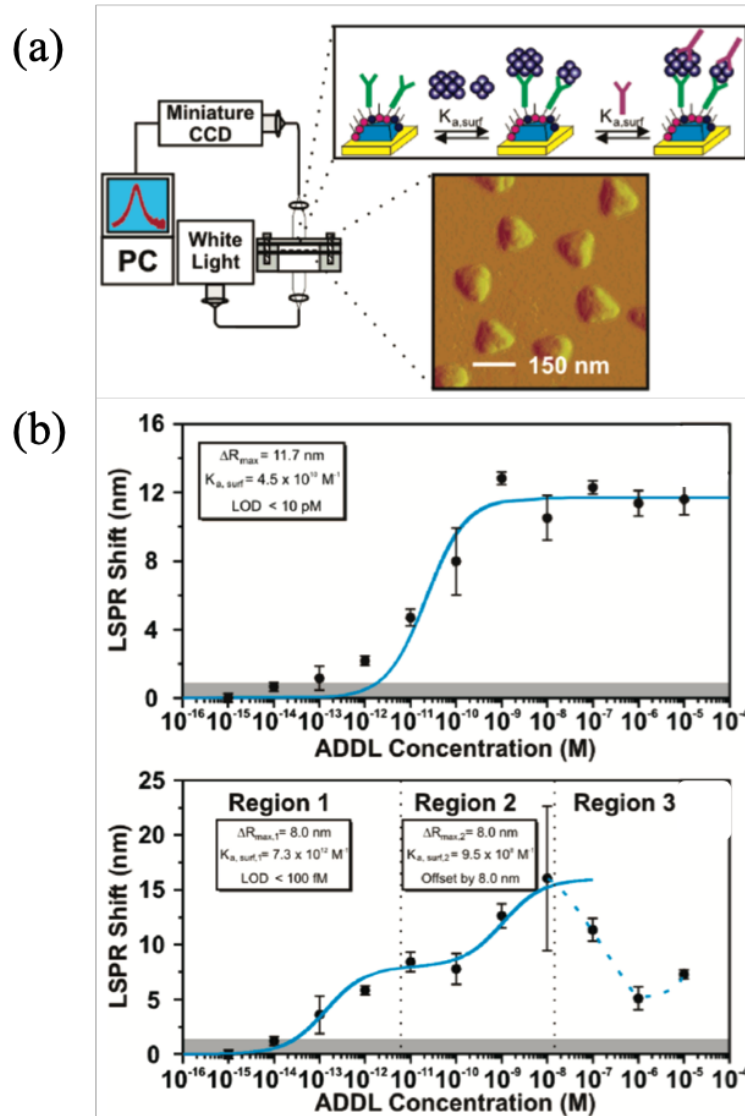


Fig. 1.21. (a) Sketch and experimental setup for LSPR; (b) Experimental results of ADDLs detection [18].

An interesting work on A $\beta$ 42 aggregation shows that ApoE4 could induce A $\beta$ 42 aggregation more rapidly and specifically than A $\beta$ 40 could, under conditions that mimicked biological conditions [23]. This study first reported on a biomimetic platform for real-time A $\beta$ 42 aggregation observation, which could be directly helpful in investigating AD, as shown in Fig. 1.22a-b.

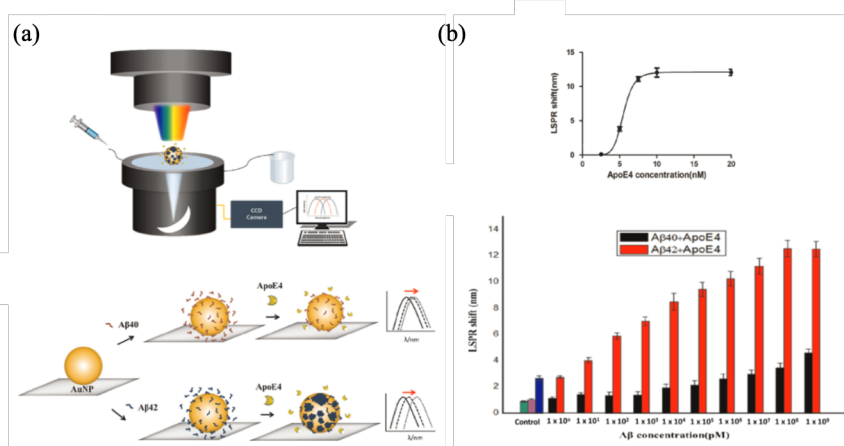


Fig. 1.22. (a) Sketch of AuNP detection principle; (b) Aβ40/42 detection results with ApoE4 [19].

An Interdigitated electrode of Gold (IDE-Au) was fabricated, and Aβ42 antibody was immobilized onto its surface [24], as shown in Fig. 1.23a. Electrochemical impedance spectroscopy (EIS) was performed to measure the impedance change during the bonding process of Aβ42 antibody and Aβ42. The sensor had high selectivity and sensitivity, able to detect concentration as low as 10 pM, with detection range from 10 pM to 100nM. A portable device was then developed by minimizing entire systems and integrated with control circuits to form a point-of-care device that is promising in real-time monitoring applications, as shown in Fig. 1.23b-c.

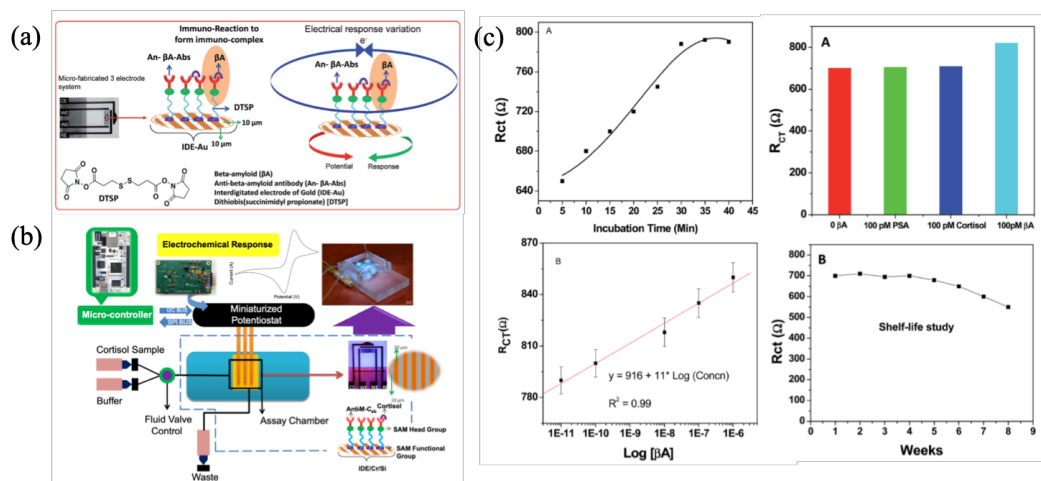


Fig. 1.23. (a) Principle of IDE-Au immunosensor; (b) developed whole system with IDE-Au based immunosensor; (c) tested results of Aβ with proposed systems [24].

A very interesting study based on square wave voltammetry was proposed for detection of soluble oligomer in CSF [25], as shown in Fig. 1.24. The surface electron transfer from Ferrocene is significantly influenced by surface bonding of the targeted A $\beta$ 42 soluble oligomer. In scanning of the square wave frequency, increased absorption at 5 Hz occurs because of electron transfer, when the soluble A $\beta$ 42 oligomer binds onto the chemically functionalized surface. By measuring the signal intensity, the concentration of soluble A $\beta$ 42 oligomer can be deduced.

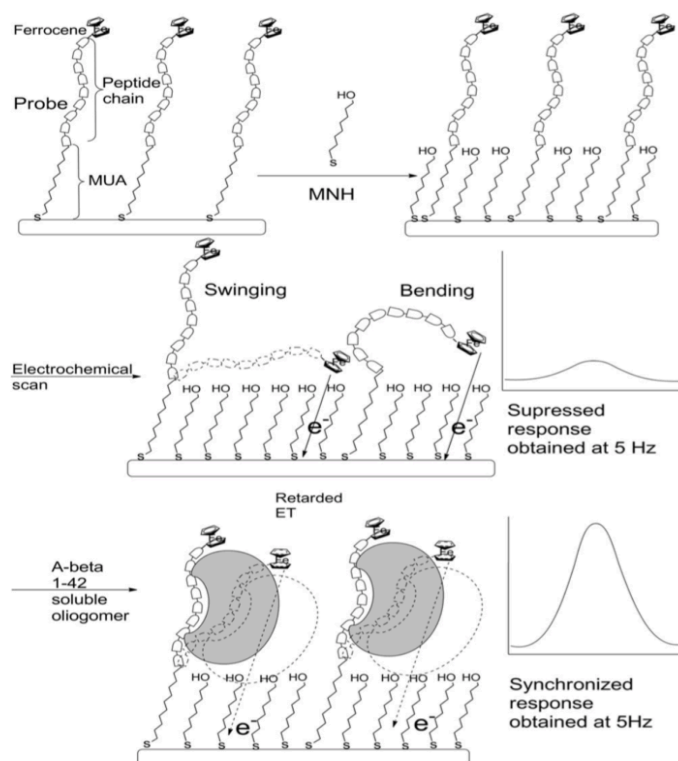


Fig. 1.24. Principle of how square wave voltammetry works for detection of A $\beta$  soluble oligomer [25].

A metal–semiconductor field-effect transistor (MESFET) based biosensor was fabricated [3], as shown in Fig. 1.25a-c. The chemical linker/antibody is immobilized onto the MESFET gate and a channel is fabricated with carbon nanotube. When the chemical linker/antibody binds with A $\beta$ 42, the threshold voltage of the field effect transistor is changed, causing the conductance of channel and source to drain current. Measuring source-to-drain current would therefore give information

about concentration. The antibody sensor has proved to be superior to the chemical linker sensor with regard to sensitivity. And as low as 1 pg/ml A $\beta$ 42 could be readily detected with antibody-based biosensor.

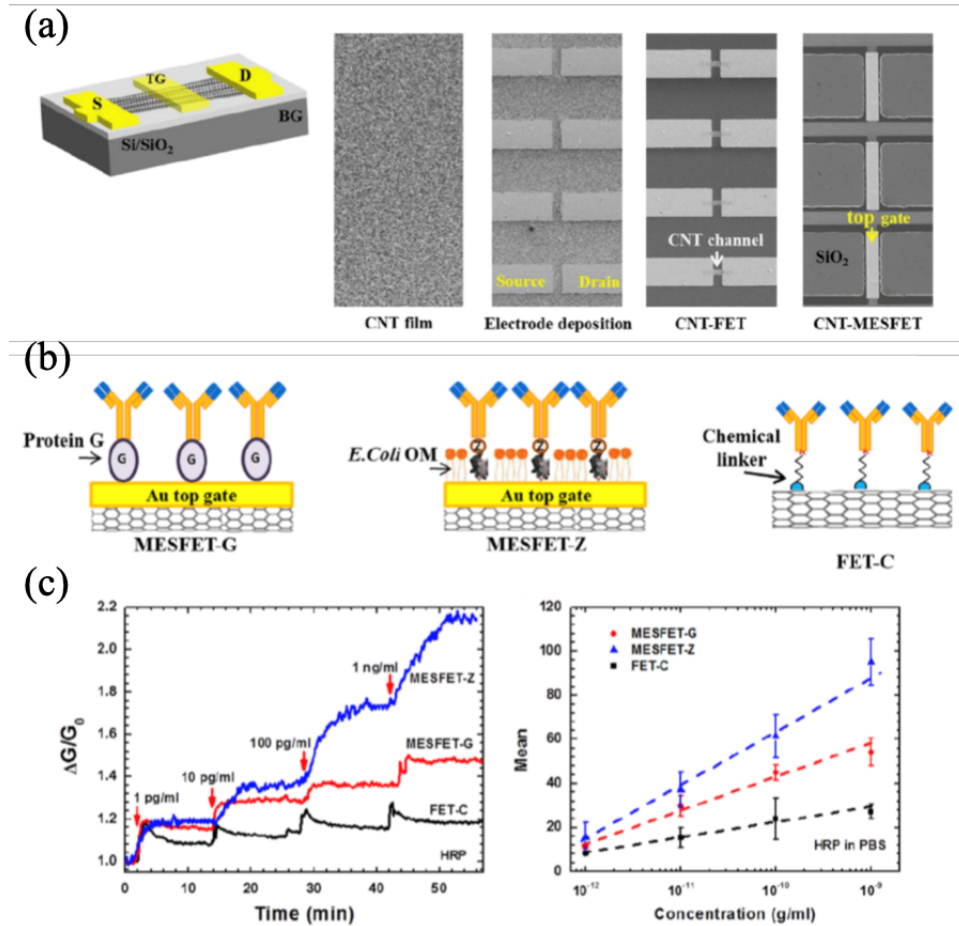


Fig. 1.25. (a) Sketch of MEFET based sensor and fabrication process; (b) surface functionalization process; (c) results of A $\beta$  biomarker detection with MEFET sensor [3].

Despite all these efforts, a device that is cost-effective, has a low detection limit, has high specificity and is capable of simultaneous detection of multiple biomarkers (A $\beta$ 42 and Ttau) and specifically designed for early diagnosis of Alzheimer's disease is still needed.

## Glaucoma

### Current Literatures on Glaucoma: Age, Symptoms, Species and Medication

Glaucoma is a group of eye diseases that result in damage to the optic nerve and vision loss due to high pressure in the eye, as shown in Fig. 1.26a-b. Recent research has shown that glaucoma is also a kind of neuron degenerative disease. The most common type is open-angle glaucoma; less common are closed-angle glaucoma (also as angle-closure glaucoma) and normal-tension glaucoma. Open-angle glaucoma develops slowly over time and there is no pain. An estimated 6 to 67 million people have glaucoma globally. The disease, which affects about 2 million people in the U.S., occurs more commonly among older people. Glaucoma has been called the "silent thief of sight" because the loss of vision usually occurs slowly, over a long period of time.

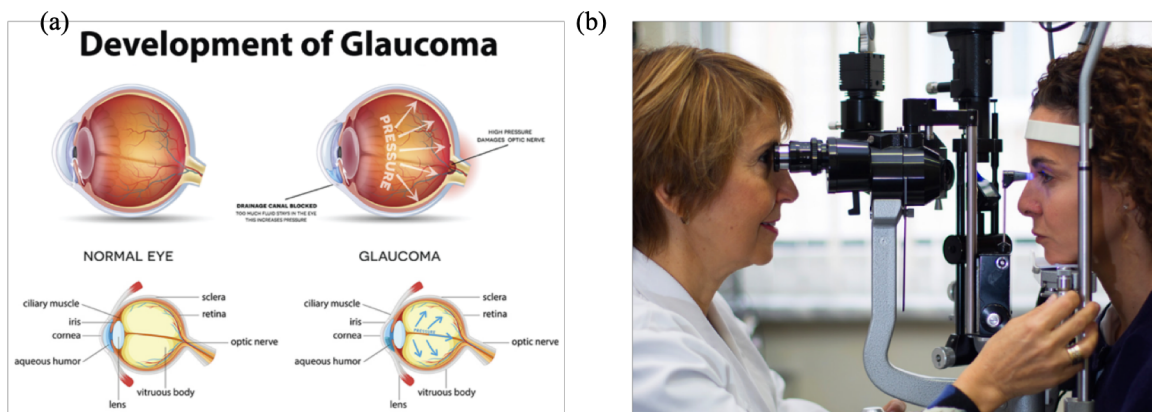


Fig. 1.26 (a) Development of glaucoma; (b) diagnosis of glaucoma using complicated equipment [26].

According to recent research, glaucoma can be categorized as a neuron degenerative disease. Glaucoma is characterized by degenerative death of retinal ganglion cells and consequent deformation or shrinkage of the optic nerve head [27-30]. The death of retinal ganglion cells is believed to be caused by increased intraocular pressure, which is caused by intraocular fluid blockage. Glaucoma can be divided of two kinds, open-angle glaucoma and closed-angle glaucoma, depending on the mechanisms by which the flow of intraocular fluid is blocked. About

90 percent of glaucoma patients have open angle glaucoma and the other 10 percent is closed-angle glaucoma. As shown in Fig. 1.27a. open angle glaucoma is due to increased resistance to aqueous humor drainage through the trabecular meshwork, which makes exit of ocular fluid from the anterior chamber more difficult. Closed-angle glaucoma is due to obstruction of the drainage pathway due to deformation of the iris and its attachment to cornea. Because intraocular fluid circulation is blocked, significantly elevated pressure develops in the anterior chamber. Such increased pressure causes stress on eye structures, especially the posterior chamber and lamina cribrosa (LC). The thickness of the LC layer is reduced and retinal ganglion (RG) cells die, which finally leads to vision loss, as shown in Fig. 1.27b.

About 25-50 percent of glaucoma patients do not have elevated intraocular pressure [31-32]. Instead, such patients may have abnormally low cerebrospinal fluid pressure, leading to a large pressure difference across the lamina cribrosa and optic nerve layer. This would also cause the same optic nerve damage as elevated intraocular pressure would cause. Also, although a strong correlation is found between high intraocular pressure and glaucoma, that does not mean elevated intraocular pressure would necessarily lead to glaucoma.

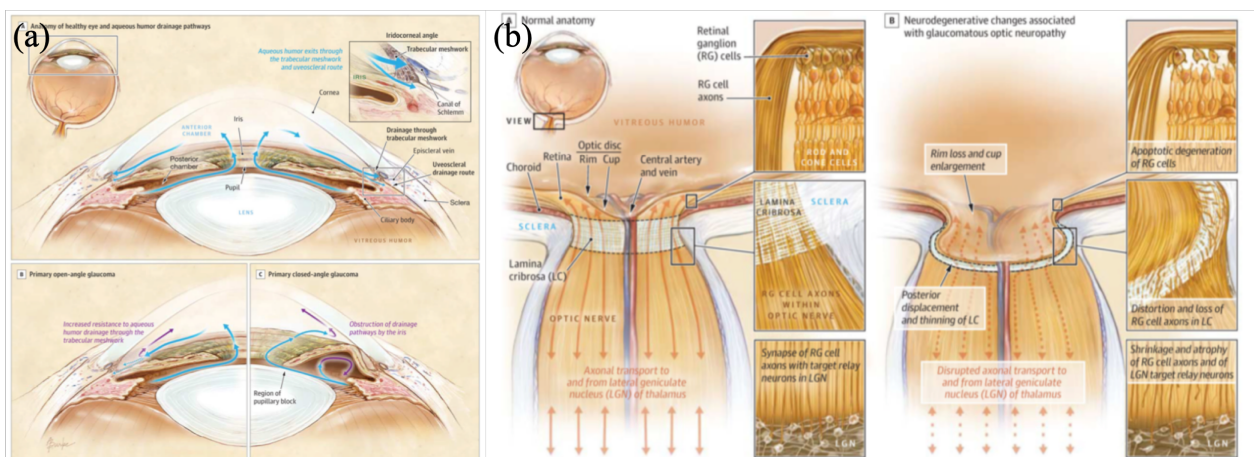


Fig. 1.27. (a) Anatomy of eye structures for intraocular fluid path ways (b) retina and nerve fiber [27-30].

The consequence of glaucoma is gradual loss of visual field [31], due to retinal ganglion cell death, as shown in Fig. 1.28. Death of retinal ganglion cells decreases the information transmitted to the brain, leading to partial or complete vision loss as glaucoma advances. The following figures show a comparison of normal vision and damaged vision due to glaucoma. For glaucoma damaged vision, there is partial field loss in the surrounding region of vision field center, and unbalanced color perception in the center region of vision.

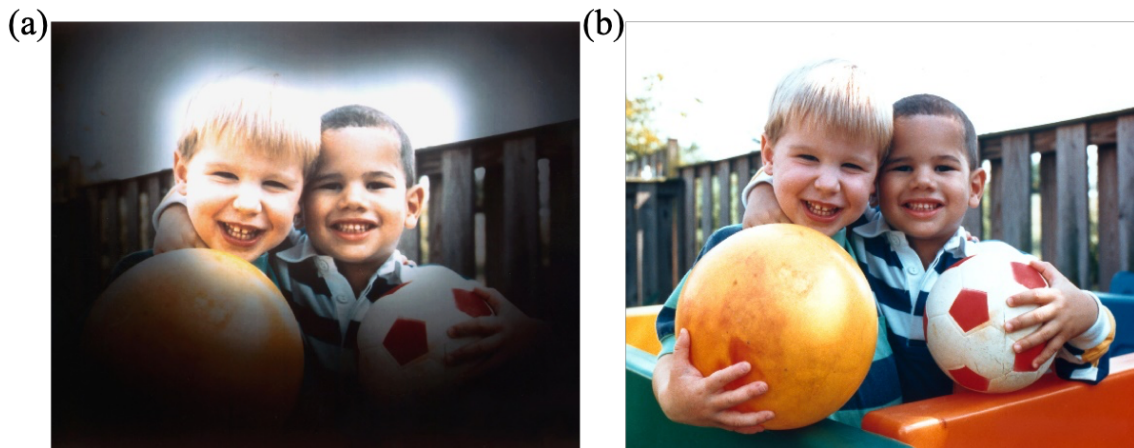


Fig. 1.28. Vision comparison of (a) glaucoma induced vision field loss and (b) health control [31].

### Diagnostic Method of Scanning Laser Tomography

Screening for glaucoma is usually performed as part of a standard eye examination by an optometrist. Testing for glaucoma should include measurements of the intraocular pressure via tonometry, anterior chamber angle examination, and examination of the optic nerve for any visible damage. A formal visual field test should be performed. The retinal nerve fiber layer can be assessed with imaging techniques such as optical coherence tomography, scanning laser polarimetry, and scanning laser ophthalmoscopy.

Tonometry is currently the fastest and easiest way to measure intraocular pressure [34-35], as shown in Fig. 1.29. It is usually done with handheld equipment operated with two hands. The head

of the tonometer is directly opposed onto the cornea. Force applied from the tonometer, causes the cornea curvature to be deformed and become flattened. After the flattened portion reaches a certain size ( $3.06 \text{ mm}^2$ ), the applied force/area reaches a balance with intraocular pressure. The reading from the equipment is the measured intraocular pressure.

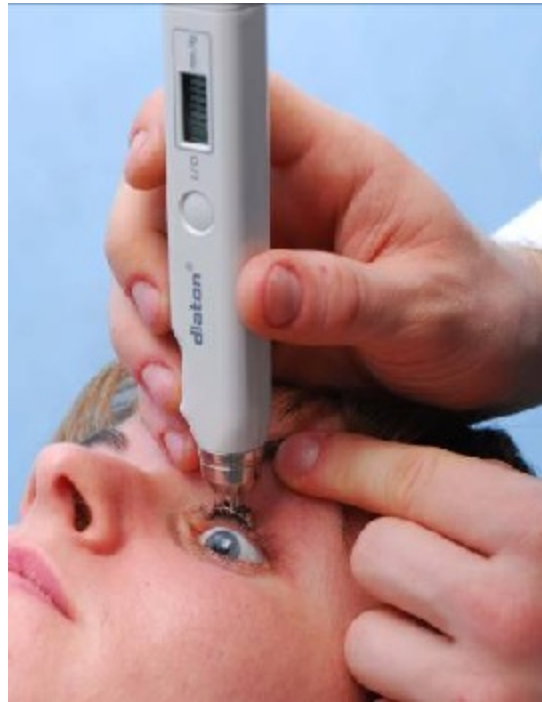


Fig. 1.29. Application of tonometer for measuring intraocular pressure [34-35].

Optical coherence tomography (OCT) is another imaging method useful in diagnosis of glaucoma [36-39]. It is a widely used biological imaging method of analyzing muscles, eyes and other soft tissues. The principle of OCT is based on low coherence interferometry, meaning that interferences can happen only when lights travel the same distances, as shown in Fig. 1.30a. The entire system works like this: as light beam from an optical source is delivered to the pellicle mirror, which splits the light ray into two different separate beams, the reference ray and sample ray. Rays from the reference mirror would interfere with rays from samples' reflection, when their optical paths are the same. The enhanced light intensity would be recorded with a camera and translated

into a surface profile of the detected tissues. Combined with the scanning of the reference reflector, this system would have the capability to image soft tissues, with the high penetration depth of infrared light wavelength. The following figures below show the difference between results with a normal retina and a glaucoma patient's retina. Because of death of retinal ganglion cells, the glaucoma retina has a significantly larger damaged optic nerve head compared to the healthy control, as shown in Fig. 1.30b.

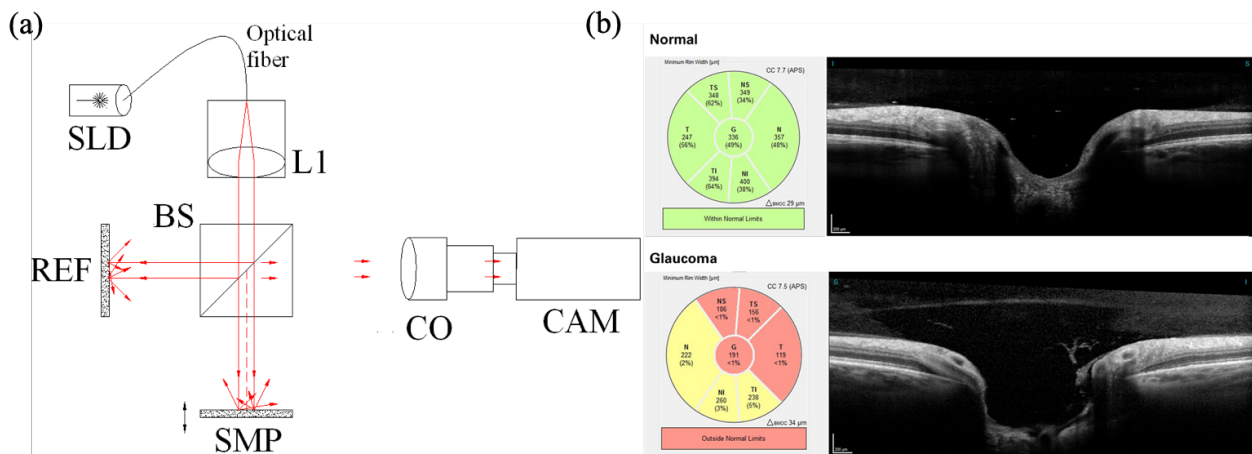


Fig. 1.30. (a) Principle of OCT; (b) OCT images of health control and glaucoma patients [36-39].

Scanning laser polarimetry is best known for effective measurement of the retina nerve fiber layer (RNFL) thickness [40-42]. This technology could be suitable for glaucoma diagnosis because of special structures of retinal ganglion cells axonal shape and their distribution. The microtubules of ganglion cells would have a birefringence effect because of different refractive indices for polarization in the x direction and the y direction, as shown in Fig. 1.31a-b. Different phase shifts after light passes through retinal ganglion cells leads to thickness information revealing of RNFL details, providing objective evidence for diagnosis of optic nerve fiber damage and thus glaucoma, as shown in Fig. 1.31c.



## **Methods Involving Contact Lenses, Implantable Devices for Eye Pressure Measurement**

Only when substantial death of retinal ganglion cell death has occurred would vision be affected, and the patient begin to realize the existence of glaucoma. However, damage has already occurred and there is no method is available to reverse this process; once the optic nerve fiber is damaged, it is damaged forever. Therefore, early detection of glaucoma is definitely meaningful for slowing down the progress of glaucoma, minimizing potential consequences, and giving better lives.

Current diagnostic methods such as tonometry or optical coherence tomography and scanning laser polarimetry are not suitable for early diagnosis of glaucoma, because of their expense (~3000 dollars for tonometer) and the level of skill required to operate such equipment (OCT, SLP). Also, methods such as OCT and SLP can be effective only after damage to the optic nerve fiber has already occurred, making them more suitable to confirm glaucoma rather than to predict glaucoma.

Research on early diagnosis of glaucoma is currently focused on measuring the intraocular pressure, because of the strong correlation between elevated intraocular pressure and glaucoma. Glaucoma patients typically have intraocular pressure above 21mmHg-22mmHg [43-44], while healthy controls do not. Implantable devices [45-47] and noninvasive devices [48-50] have both been proposed as treatments.

Figure 1.32a shows an implantable IOP system designed for measuring intraocular pressure [51]. The key part of this system consists of a microfluidics channel and gas reservoir. When the system is implanted, intraocular pressure pushes intraocular fluid into the microfluidics channel. The gas in the gas reservoir and channel would therefore be compressed so that its pressure is higher than in the normal situation. Increased gas pressure inside the channel/reservoir would counter the pressure of the entered intraocular fluid, so that a static balance is obtained with the gas/interface located at a specific position inside the channel. The interface position would be directly

determined by the level of intraocular fluid pressure, thus achieving a quantitative measurement of IOP. The experimentally determined position of the gas/liquid interface is linearly related to intraocular pressure, as shown in Fig. 1.32b.

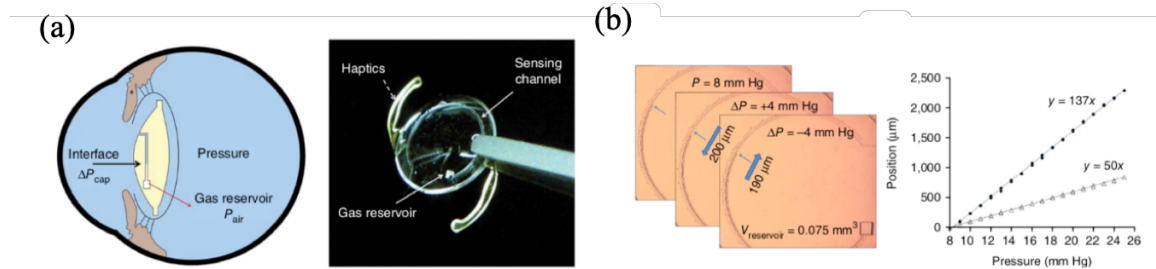


Fig. 1.32. (a) An implantable IOP measurement system; (b) results showing position versus pressure [51].

Another example is a contact lens fabricated with an antenna imbedded between layers of the lenses [52], as shown in Fig. 1.33a-f. The contact lens contacts the cornea of the eye, and any pressure change inside the eye would deform the contact lens and antenna. Deformation of the antenna results in a change of resonance frequency change, which is thus utilized as a transducing signal to indicate an intraocular pressure change. The contact lens is flexible and has good reliability. Stretching experiments have shown that the fabricated contact lens can tolerate up to 10,000 bending cycles. In addition to use in intraocular pressure measurement, the contact lens could be used for measuring tear glucose concentration in tears.

However, since some glaucoma patients do not have elevated intraocular pressure, simply measuring intraocular pressure does not provide sufficient evidence to predict glaucoma and accomplish early diagnosis of the disease. Use of implantable devices requires surgery for implanting device and involves increased cost and patient discomfort. Recent research has found one particular biomarker for glaucoma, IL12p70. Glaucoma patients have considerably lower IL12p70 concentrations in their tears, compared to healthy controls [53]. Therefore, including detection of this biomarker as well as IOP measurement could strengthen the evidence needed to

confirm or rule out early glaucoma. With regard to treatment, reducing intraocular pressure is current the only proven way to treat glaucoma so as to slow down its progress. Of course, surgery to open up the channel for flow of intraocular liquid is an option, but it is still not a cure. The common method, delivery of certain drugs (such as Timolol) that is effective but inconvenient, decreases intraocular pressure by use of eyedrops each day.

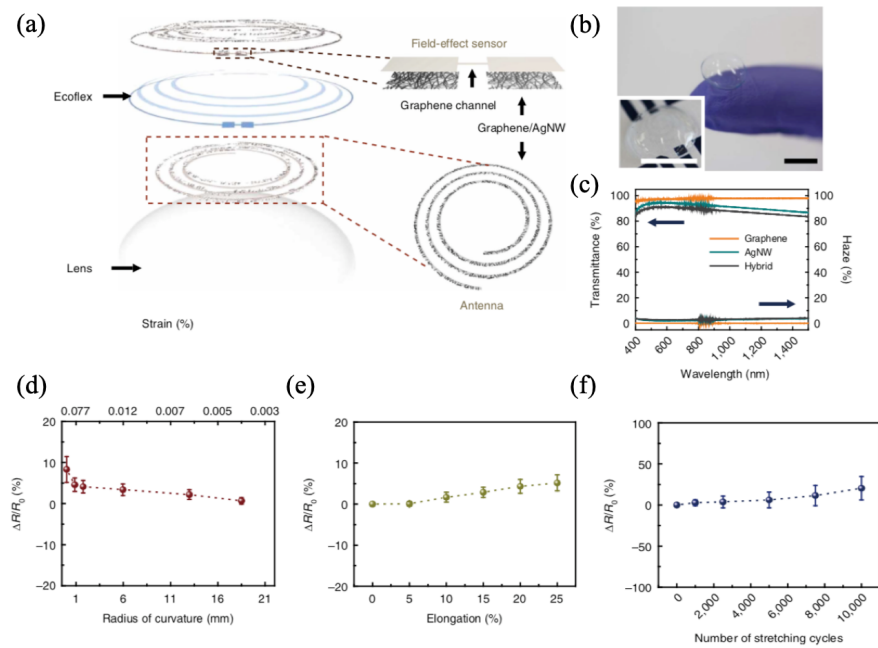


Fig. 1.33. (a) Contact lens sensor structure illustration; (b) fabricated contact lens sensor; (c) transmittance of contact lens; (d) resistance change with lens curvature; (e) resistance change with elongation; (f) resistance change with stretching cycles [52].

Simpler ways of diagnosing glaucoma, involving less complicated procedures and at lower cost are desirable. To this end, we will report on another technology to monitor eye pressure and treat glaucoma.

## Dissertation Organization

The dissertation is mainly to summarize my research work during my four-year PhD studies at Iowa State University. This dissertation consists of seven chapters: (1) Introduction about

Alzheimer's Disease and Glaucoma background and detection challenge; (2) Rapid multiplexed detection of beta-amyloid and total-tau as biomarkers for Alzheimer's disease in cerebrospinal fluid [54]; (3) Nanopore thin film enabled optical platform for drug loading and release [55]; (4) A flexible nanopore thin film enabled device for pressure sensing and drug release [56]; (5) High-resolution, flexible, and transparent nanopore thin film sensor enabled by cascaded Fabry–Perot effect [57]; and (6) A multifunctional contact lens [58]; (7) future work.

The first chapter is introduction to background of neurodegenerative disease, which includes literature review regarding pathological description of Alzheimer's Disease (AD), conventional and current diagnostic methods of Alzheimer's Disease and related challenge, our new label-free optical devices targeting point-of-care and early diagnosis of AD. Introduction also includes background description of glaucoma, which is also a neurodegenerative disease happened to eyes as aging. The developing process of glaucoma is introduced, and symptoms are illustrated. Challenges about early detection of glaucoma are mentioned and a new type of multifunctional contact lens device is proposed to monitor/treat glaucoma.

The second chapter of this dissertation is about our proposed microfluidic device for demonstrating the simultaneous detection of two biomarkers for AD using Anodic Aluminum Oxide (AAO) nanopore optical interference sensing mechanism. Several microfluidic passive valves are designed in the microfluidics device to control the chemicals flow. The antibodies specific to different biomarkers are immobilized onto AAO nanopore sensing surfaces by NHS/EDC assisted chemical bonding method. Concentrations of biomarkers can be estimated and quantified by the shifts of the optical signals in the broadband visible light spectrum reflected from the AAO nanopore sensors.

The third and fourth chapter of this dissertation are about developing flexible device for drug loading and releasing, also for pressure sensing. The AAO thin film is transferred onto PDMS flexible thin film, resulting in a flexible AAO thin film device. The drug is loaded onto the flexible device using a layer by layer nanoassembly process and the drug release process from the device into DI water is monitored. Due to its flexibility and optical interference properties, this type of flexible device can also be used as angle sensor and pressure sensor.

The fifth chapter of this dissertation is about developing *thin* flexible AAO/PDMS substrate with new fabrication process, compared to *thick* flexible AAO/PDMS substrate. The thinner AAO/PDMS substrate has significantly improved flexibility and sensitivity. New fabrication process involves spinning coating uncured PDMS onto AAO film, peeling off AAO/PDMS with great cares and techniques. Thinner AAO/PDMS is capable of stretching, bending, random reshaping due to the improved flexibility from much thinner PDMS substrate. Improved sensitivity is mainly due to denser optical interference fringes introduced by PDMS thin film. With smaller FWHM of denser fringes, resolution is enhanced, and sensitivity is improved.

The sixth chapter of this dissertation is about developing multifunctional contact lens. Originally from the Chapter 4, thin AAO/PDMS substrate are fabricated and integrated with a contact lens. The integrated contact lens has three functions: angular sensor for monitoring cornea curvature change due to intraocular pressure (IOP), detection of one glaucoma biomarker IL12p70, and sustained drug delivery to treat glaucoma. The angular sensor is sensitive enough for a minute curvature change due to its increased sensitivity. Antibody will be immobilized onto contact lens surface with similar surface functionalization procedures in Section one for detecting glaucoma biomarker. Sustained drug release becomes possible because of the large surface areas and nanopore structures of AAO.

The seventh chapter is about future work to improve current developed devices and target point-of-care applications.

### References

- [1] [www.silverbook.org/fact/projected-percent-of-u-s-population-aged-65-and-older-2010-to-2050/](http://www.silverbook.org/fact/projected-percent-of-u-s-population-aged-65-and-older-2010-to-2050/)
- [2] [https://en.wikipedia.org/wiki/Alzheimer%27s\\_disease](https://en.wikipedia.org/wiki/Alzheimer%27s_disease)
- [3] A. Kaushik, R. D. Jayant, S. Tiwari, A. Vashist, and M. Nair, "Nano-biosensors to detect beta-amyloid for Alzheimer's disease management," *Biosensors and Bioelectronics*, vol. 80, pp. 273-287, 2016.
- [4] E. R. Mayeda, M. M. Glymour, C. P. Quesenberry, and R. A. Whitmer, "Inequalities in dementia incidence between six racial and ethnic groups over 14 years," *Alzheimer's Dement*, vol.12, pp. 216-224, 2016.
- [5] R. J. Bateman, C. Xiong, "Clinical and biomarker changes in dominantly inherited Alzheimer's disease," *New England Journal of Medicine*, vol. 367, no. 9, pp. 795-804, 2012.
- [6] O. Preische, S. A. Schultz, "Serum neurofilament dynamics predicts neurodegeneration and clinical progression in presymptomatic Alzheimer's disease," *Nature Medicine*, vol. 25, pp. 277-283, 2019.
- [7] N. Salvadores, M. Shahnawaz, E. Scarpini, F. Tagliavini, and C. Soto, "Detection of Misfolded A $\beta$  Oligomers for Sensitive Biochemical Diagnosis of Alzheimer's Disease," *Cell Reports*, vol. 7, no. 1, 261-268, 2014.
- [8] G. McKhann, D. Drachman, M. Folstein, R. Katzman, D. Price, and E. M. Stadlan, "Clinical diagnosis of Alzheimer's disease: report of the NINCDS-ADRDA Work Group under the auspices of Department of Health and Human Services Task Force on Alzheimer's Disease," *Neurology*, vol. 34, no. 7, pp. 939-944, 1984.
- [9] <https://institute.progress.im/en/content/brain-imaging-psychiatrists-part-2-structural-static-measures>
- [10] L. Vermunt, AJL Van Paasen, C.E. Teunissen, P. Scheltens, P.J. Visser, and B. M. Tijms, "Alzheimer's Disease Neuroimaging Initiative. Alzheimer disease biomarkers may aid in the prognosis of MCI cases initially reverted to normal," *Neurology*, vol. 92, no. 23, pp. e2699-e2705, 2019.
- [11] M. R. Brier, B. Gordon, K. Friedrichsen, J. McCarthy, A. Stern, J. Christensen, C. Owen, P. Aldea, Y. Su, J. Hassenstab, N. J. Cairns, D. M. Holtzman, A. M. Fagan, J. C. Morris, T. L. S. Benzinger, and B. M. Ances, "Tau and Ab imaging, CSF measures, and cognition in Alzheimer's disease," *Science Translational Medicine*, 2016.
- [12] D. G. Amen, P. Krishnamani, S. Meysami, A. Newberg, and C. A. Raji, "Classification of Depression, Cognitive Disorders, and Co-Morbid Depression and Cognitive Disorders with Perfusion SPECT Neuroimaging," *Journal of Alzheimer's Disease*, vol. 57, no. 1, pp. 253-266, 2017.
- [13] R. A. Sperling, J. Karlawish, and K. A. Johnson, "Preclinical Alzheimer disease - The challenges ahead," *Nature Review Neurology*, 2013.
- [14] R. A. Sperling, P. S. Aisen, L. A. Beckett, "Toward defining the preclinical stages of Alzheimer's disease: Recommendations from the National Institute on Aging-Alzheimer's Association workgroups on diagnostic guidelines for Alzheimer's disease," *Alzheimer's Dement*, vol. 7, no. 3, pp. 280-292, 2011.
- [15] R. Li, G. Rui, W. Chen, S. Li, P. E. Schulz, and Y. Zhang, "Early Detection of Alzheimer's Disease Using Non-invasive Near-Infrared Spectroscopy," *Frontiers in Aging Neuroscience*, vol. 10, 2018.

- [16] B. E. O'Bryhim, R. S. Apte, N. Kung, D. Coble, and G. P. Van Stavern, "Association of Preclinical Alzheimer Disease with Optical Coherence Tomographic Angiography Findings," *JAMA Ophthalmology*, vol. 136, no. 11, pp. 1242-1248, 2018.
- [17] N. Salvadores, M. Shahnawaz, E. Scarpini, F. Tagliavini, and C. Soto, "Detection of Misfolded A $\beta$  Oligomers for Sensitive Biochemical Diagnosis of Alzheimer's Disease," *Cell Reports*, vol. 7, pp. 261–268 (2014).
- [18] O. Preische, S. A. Schultz, A. Apel, "Serum neurofilament dynamics predicts neurodegeneration and clinical progression in presymptomatic Alzheimer's disease," *Nature Medicine*, vol. 25, pp. 277-283, 2019.
- [19] P. Gagni, L. Sola, M. Cretich, and M. Chiari, "Development of a high-sensitivity immunoassay for amyloid-beta 1-42 using a silicon microarray platform," *Biosensors and Bioelectronics*, vol. 47, pp. 490-495, 2013.
- [20] D. G. Georganopoulou, L. Chang, J.-M. Nam, C. S. Thaxton, E. J. Mufson, W. L. Klein, and C. A. Mirkin, "From The Cover: Nanoparticle-based detection in cerebral spinal fluid of a soluble pathogenic biomarker for Alzheimer's disease," *Proceedings of National Academy of Science*, vol. 102, pp. 2273–2276, 2005.
- [21] T. Demeritte, B. P. Viraka Nellore, R. Kanchanapally, S. S. Sinha, A. Pramanik, S. R. Chavva, and P. C. Ray, "Hybrid Graphene Oxide Based Plasmonic-Magnetic Multifunctional Nanoplatfrom for Selective Separation and Label-Free Identification of Alzheimer's Disease Biomarkers," *ACS Applied Materials & Interfaces*, vol. 7, pp. 13693-13700, 2015.
- [22] A. J. Haes, L. Chang, W. L. Klein, and R. P. Van Duyne, "Detection of a biomarker for Alzheimer's disease from synthetic and clinical samples using a nanoscale optical biosensor," *Journal of American Chemical Society*, vol. 127, no. 7, pp. 2264-2271, 2005.
- [23] M. K. Kang, J. Lee, A. H. Nguyen, and S. J. Sim, "Label-free detection of ApoE4-mediated  $\beta$ -amyloid aggregation on single nanoparticle uncovering Alzheimer's disease," *Biosensors and Bioelectronics*, vol. 72, pp. 197-204, 2015.
- [24] A. Kaushik, P. Shah, P. K. Vabbina, R. D. Jayant, S. Tiwari, A. Vashist, A. Yndart, and M. Nair, "A label-free electrochemical immunosensor for beta-amyloid detection," *Analytical Methods*, vol. 8, pp. 6115-6120, 2016.
- [25] A. Kaushik, P. Shah, P. K. Vabbina, R. D. Jayant, S. Tiwari, A. Vashist, A. Yndart, and M. Nair, "A label-free electrochemical immunosensor for beta-amyloid detection," *Analytical Methods*, vol. 8, pp. 6115-6120, 2016.
- [26] <https://www.allenrichmondmd.com/our-services/glaucoma/>
- [27] R. N. Weinreb, T. Aung, and F. A. Medeiros, "The pathophysiology and treatment of glaucoma: A review," *JAMA-Journal of American Medical Association*, vol. 311, pp. 1901–1911, 2014.
- [28] H. A. Quigley, E. M. Addicks, W. R. Green, and A. E. Maumenee, "Optic nerve damage in human glaucoma: Ii. The Site of Injury and Susceptibility to Damage," *Archives of Ophthalmology*, vol. 99, no. 4, pp. 635-649, 1981.
- [29] C. F. Burgoyne, J. Crawford Downs, A. J. Bellezza, J. K. Francis Suh, and R. T. Hart, "The optic nerve head as a biomechanical structure: A new paradigm for understanding the role of IOP-related stress and strain in the pathophysiology of glaucomatous optic nerve head damage," *Progress in Retinal and Eye Research*, vol. 24, no. 1, pp. 39-73, 2005.
- [30] H. A. Quigley, S. J. McKinnon, D. J. Zack, M. E. Pease, L. A. Kerrigan-Baumrind, D. F. Kerrigan, and R. S. Mitchell, "Retrograde axonal transport of BDNF in retinal ganglion cells is blocked by acute IOP elevation in rats," *Investigative Ophthalmology and Visual Science*, vol. 41, no.11, pp. 3460-3466, 2000.
- [31] Weinreb RN, Khaw PT, "Primary open-angle glaucoma," *Lancet*, vol. 363, no. 9422, pp. 1711-1720, 2004.
- [32] Fechtner RD, Weinreb RN, "Mechanisms of optic nerve damage in primary open angle glaucoma," *Survey of Ophthalmology*, vol. 39, no.1, pp. 23–42, 1994.
- [33] National Eye Institute, "Facts About Glaucoma," *National Institutes of Health*, 2009.

- [34] J. W. Smith, "Tonometry," *American Journal of Ophthalmology*, vol. 9, no. 10, pp. 773-777, 1926.
- [35] M. R. Nelson, J. Stepanek, M. Cevette, "Noninvasive measurement of central vascular pressures with arterial tonometry: Clinical revival of the pulse pressure waveform," *Mayo Clinic Proceedings*, 2010.
- [36] H. G. Bezerra, M. A. Costa, G. Guagliumi, A. M. Rollins, and D. I. Simon, "Intracoronary Optical Coherence Tomography: A Comprehensive Review," *JACC: Cardiovascular Interventions*, vol. 2, no. 11, pp. 1035-1046, 2009.
- [37] D. Huang, E. A. Swanson, C. P. Lin, "Optical Coherence Tomography HHS Public Access," *Science*, vol. 80, 1991.
- [38] I. I. Bussel, G. Wollstein, and J. S. Schuman, "OCT for glaucoma diagnosis, screening and detection of glaucoma progression," *British Journal of Ophthalmology*, vol. 98, 2014.
- [39] V. Kansal, J. J. Armstrong, R. Pintwala, and C. Hutnik, "Optical coherence tomography for glaucoma diagnosis: An evidence based meta-analysis," *PLoS One*, vol. 13, no. 1, 2018.
- [40] S. Da Pozzo, R. Marchesan, and G. Ravalico, "Scanning laser polarimetry - A review," *Clinical and Experimental Ophthalmology*, vol. 37, no. 1, pp. 68-80, 2009.
- [41] R. N. Weinreb, C. Bowd, D. S. Greenfield, "Measurement of the magnitude and axis of corneal polarization with scanning laser polarimetry," *Archives of Ophthalmology*, vol. 120, no. 7, pp. 901-906, 2002.
- [42] F. A. Medeiros, L. M. Alencar, L. M. Zangwill, C. Bowd, G. Vizzeri, P. A. Sample, and R. N. Weinreb, "Detection of progressive retinal nerve fiber layer loss in glaucoma using scanning laser polarimetry with variable corneal compensation," *Investigative Ophthalmology and Visual Science*, vol. 50, no. 4, pp. 1675-1681, 2009.
- [43] A. V. Mantravadi, N. Vadhar, "Glaucoma," *Primary Care*, vol. 42, no. 3, pp. 437-49, 2015.
- [44] Rhee, J. Douglas. "Glaucoma," *Philadelphia: Wolters Kluwer Health/Lippincott Williams & Wilkins*, pp. 180, 2012.
- [45] P. J. Chen, D. C. Rodger, S. Saati, M. S. Humayun, and Y. C. Tai, "Microfabricated implantable parylene-based wireless passive intraocular pressure sensors," *Journal of Microelectromechanical Systems*, vol. 17, no. 6, pp. 1342-1351, 2008.
- [46] E. Y. Chow, A. L. Chlebowski, and P. P. Irazoqui, "A miniature-implantable RF-wireless active glaucoma intraocular pressure monitor," *IEEE Transactions on Biomedical Circuits and Systems*, vol. 4, no. 6, pp. 340-349, 2010.
- [47] G. Chitnis, T. Maleki, B. Samuels, L. B. Cantor, and B. Ziaie, "A minimally invasive implantable wireless pressure sensor for continuous IOP monitoring," *IEEE Transactions on Biomedical Engineering*, vol. 60, no. 1, pp. 250-256, 2013.
- [48] P. J. Chen, D. C. Rodger, R. Agrawal, S. Saati, E. Meng, R. Varma, M. S. Humayun, and Y. C. Tai, "Implantable micromechanical parylene-based pressure sensors for unpowered intraocular pressure sensing," *Journal of Micromechanics and Microengineering*, vol. 17, no. 10, pp. 1931-1938, 2007.
- [49] G. Z. Chen, I. S. Chan, L. K. K. Leung, and D. C. C. Lam, "Soft wearable contact lens sensor for continuous intraocular pressure monitoring," *Medical Engineering and Physics*, vol. 36, no. 9, pp. 1134-1139, 2014.
- [50] M. Leonardi, E. M. Pitchon, A. Bertsch, P. Renaud, and A. Mermoud, "Wireless contact lens sensor for intraocular pressure monitoring: Assessment on enucleated pig eyes," *Acta Ophthalmologica*, vol. 87, no. 4, pp. 433-437, 2009.
- [51] I. E. Araci, B. Su, S. R. Quake, and Y. Mandel, "An implantable microfluidic device for self-monitoring of intraocular pressure," *Nature Medicine*, vol. 20, no. 9, pp. 1074-1078, 2014.
- [52] J. Kim, M. Kim, M. S. Lee, K. Kim, S. Ji, Y. T. Kim, J. Park, K. Na, K. H. Bae, H. K. Kim, F. Bien, C. Y. Lee, and J. U. Park, "Wearable smart sensor systems integrated on soft contact lenses for wireless ocular diagnostics," *Nature Communications*, vol. 8, pp. 14997, 2017.
- [53] D. Gupta, J. C. Wen, J. L. Huebner, S. Stinnett, V. B. Kraus, H. C. Tseng, and M. Walsh, "Cytokine biomarkers in tear film for primary open-angle glaucoma," *Clinical Ophthalmology*, vol. 11, pp. 411-416, 2017.

- [54] Chao Song\*, Pan Deng\*, and Long Que. "Rapid multiplexed detection of Beta-amyloid and Total-tau as biomarkers for Alzheimer's disease in cerebrospinal fluid." *Nanomedicine: Nanotechnology, Biology and Medicine*, vol. 14, no. 6, pp. 1845-1852, 2018.
- [55] Chao Song, Xiangchen Che, and Long Que. "Nanopore thin film enabled optical platform for drug loading and release." *Optics Express*, vol. 25, no. 16, pp. 19391-19397, 2017.
- [56] Chao Song, Pan Deng, Xiaoke Ding, and Long Que. "A Flexible Nanopore Thin Film Enabled Device for Pressure Sensing and Drug Release." *IEEE Transactions on Nanotechnology*, vol. 17, no. 5, pp. 962-967, 2018.
- [57] Chao Song, Xiaoke Ding, and Long Que. "High-resolution, flexible and transparent nanopore thin film sensor enabled by cascaded Fabry-Perot effect." *Optics Letters*, vol. 43, no. 13, pp. 3057-3060, 2018.
- [58] Chao Song, Gil Ben-Shlomo, and Long Que. "A multifunctional smart soft contact lens device enabled by nanopore thin film for glaucoma diagnostics and in situ drug delivery," *Journal of Microelectromechanical Systems* (published), 2019.

## CHAPTER 2. RAPID MULTIPLEXED DETECTION OF BETA-AMYLOID AND TOTAL-TAU AS BIOMARKERS FOR ALZHEIMER'S DISEASE IN CEREBROSPINAL FLUID

Chao Song\*, Pan Deng\*, and Long Que. *Nanomedicine: Nanotechnology, Biology and Medicine*, vol. 14, no. 6, pp. 1845-1852, 2018.

### Abstract

This paper reports the multiplexed monitoring of two promising biomarkers, beta-amyloid (A $\beta$ 42) and total tau (T-tau), in both buffer and cerebrospinal fluid (CSF) for Alzheimer's disease (AD) using label-free optical nanosensors. It has been found that 7.8 pg/ml of A $\beta$ 42 in buffer and 15.6 pg/ml of T-tau in buffer can be readily detected with very good specificity. Based on our measurements, the purchased CSF itself contains A $\beta$ 42, whose concentration is estimated to be about 400 pg/ml. A $\beta$ 42 and T-tau in the mixtures of A $\beta$ 42 and T-tau spiked in CSF have been detected successfully, indicating the feasibility of the optical nanosensors to detect these biomarkers in clinical samples. For the measurements, only a small amount ( $\sim 1 \mu\text{l}$ ) of the samples is required. This type of sensor is suitable for point-of-care application to diagnose the AD due to its low cost and ease-of-operation.

### Introduction

Alzheimer's disease (AD), as a chronic progressive neurodegenerative disease, is the most prevalent type of dementia. According to the Alzheimer's Association, the number of AD patients will almost double every 20 years, reaching 75 million in 2030 and 131.5 million in 2050. Even though the diagnostic means such as neuroimaging methods (magnetic resonant imaging, positron emission tomography, single-photon emission computed tomography, etc.) are under continual

improvement for the past decades, it is still a challenge to increase the sensitivity and specificity of a diagnosis of Alzheimer's disease. Until now, beta-amyloid (A $\beta$ 42), total tau (T-tau) and phospho-tau (P-tau) inside serum or cerebrospinal fluid (CSF) (Fig. 2.1a) are still the best biological markers to diagnose Alzheimer's disease and differentiate it from other forms of dementia with a high reliability and validity [1, 2]. Clinically relevant concentration ranges of A $\beta$ 42 and T-tau are  $382.2 \pm 102.0$  pg/ml and at least  $> 300$  pg/ml, respectively [3, 4]. Available methods such as neuroimaging and enzyme-linked immunosorbent assay (ELISA) have been used to detect A $\beta$ 42, T-Tau and P-tau [5, 6]. However, because of the requirements of the sophisticated equipment, the highly experienced personnel for the complicated operation, and the challenge of low detection limit, these methods are typically expensive and time-consuming, and not yet extended to and unsuitable for point-of-care (POC) diagnostics. To this end, some microsensors and nanotechnologies have been developed in recent years to address these issues. Examples include fluorescence imaging and electrochemical impedance spectroscopy based sensors for the detection of A $\beta$ 42 [7-9]. However, the technologies, which can provide ease-of-use platforms with high sensitivity and specificity, and suitable for POC diagnostics, are still critically needed. Herein, label-free monitoring of beta-amyloid and T-tau in CSF using optical nanosensors is reported.

The label-free nanosensor (Fig. 2.1b-c) is adapted from the nanostructured Fabry-Perot interference (nanoFPI) sensor developed in our lab [10, 11]. In this type of sensor, a layer of nanopores, which is the anodic aluminum oxide (AAO) embedded in the Fabry-Perot cavity, serves as the sensing element. The reflected white light from the nanoFPI sensor forms interference fringes, which are used as transducing signals.

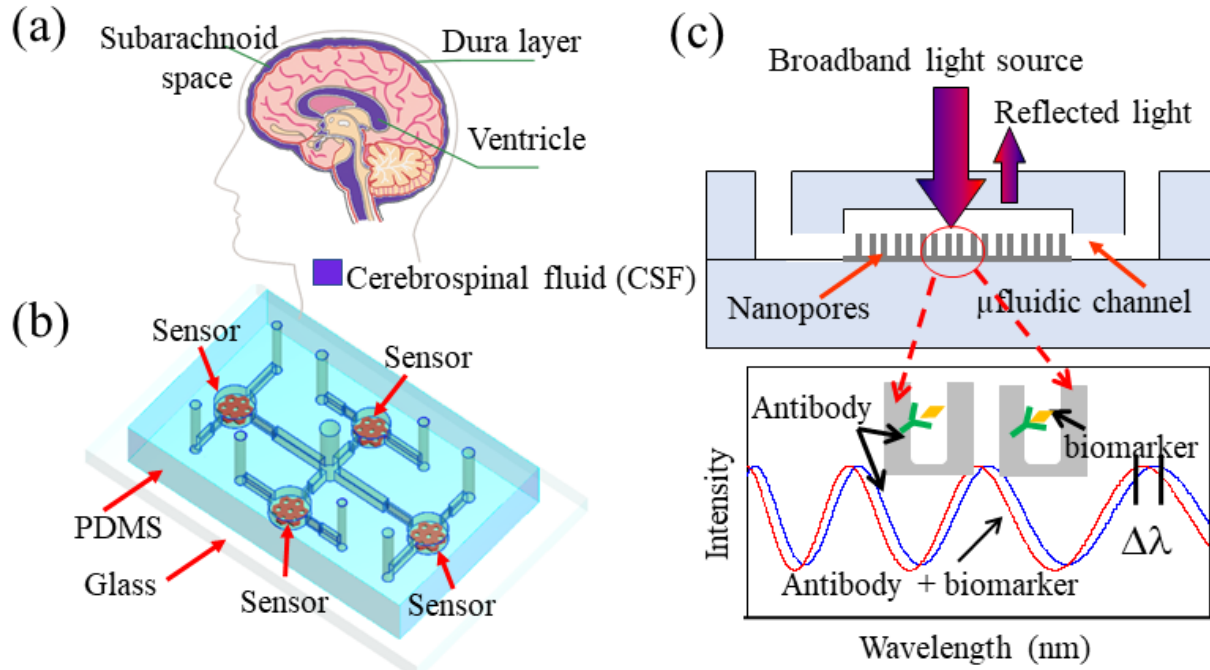


Fig. 2.1. (a) Sketch showing cerebrospinal fluid (CSF) inside the brain. Monitoring the biomarkers such as A $\beta$ 42, T-tau inside CSF to diagnoses Alzheimer's disease; (b) Schematic of a chip, consisting of four nanopore sensors; with integrated microfluidic network; (c) Close-up of nanopore thin film sensor and its operational principle.

## Methods

### Chemicals and Materials

A $\beta$ 42 antibody and biomarker: Mouse anti-Amyloid Beta Peptide 42(A $\beta$ 42) monoclonal antibody (detector mAb) (cat. # MO-M40093B, Clone # CA9 10C11), ELISA kits for human A $\beta$ 42 (Cat. # EL10057) were obtained from Anogen-YES Biotech Laboratories Ltd. (Mississauga, Canada). A $\beta$ 42 standard is reconstituted by standard diluent provided in the ELISA kit. 1mM AEBSF in protease inhibitor cocktail (cat. # P8340-1ML, Thermo Fisher Scientific Inc., IL, USA) is added to appropriate standard diluent before use. Nano-pore purified water is used to reconstitute anti-A $\beta$ 42 mAb to a concentration of 10  $\mu$ g/ml.

T-tau antibody and biomarker: Anti-Human Tau monoclonal antibody (200 $\mu$ g/ml, cat.# MN1000, Clone # HT7) and Tau (Total, T-tau) Human ELISA Kit (Cat.# KHB0041) was obtained

from Thermo Fisher Scientific Inc.(IL, USA). Human T-tau is reconstituted by standard diluent buffer provided in the ELISA kit. Nano-pore purified water is used to dilute anti-T-tau mAb to the concentration of 10 $\mu$ g/ml.

Cerebrospinal fluid: Cerebrospinal Fluid (Pooled Human Donors) (cat. # 991-19-P) was purchased from Lee Biosolutions, Inc. (Missouri, USA).

Materials/chemicals for surface functionalization of sensor surface: 11-Mercaptoundecanoic acid (HSC<sub>10</sub>COOH, 99%), 8-Mercapto-1-Octanol (HSC<sub>8</sub>OH, 98%), N-(3-Dimethylaminopropyl)-N'-ethylcarbodiimide hydrochloride (EDC), N-Hydroxysuccinimide (NHS), and ethanolamine (EA), Phosphoric acid (PPA) and PBS buffer were purchased from Sigma-Aldrich (Milwaukee, WI) and used without further purification. Deionized (DI) water was obtained from a DI water purification system (Millipore, FRANCE).

### **Sensor Chip and Its Transducing Signals**

A sensor chip consisting of four sensors fabricated from anodic aluminum oxide (AAO) nanopore thin film on a glass substrate is shown in Fig. 2.1b. The fabrication process is adapted from our previous work [12]. Its operational principle is illustrated in Fig. 2.1c. The A $\beta$ 42 antibody or T-tau antibody are immobilized on the chemically functionalized sensing surface. When the biomarker is bound to the antibody, the reflected optical signal (interference fringes) from the sensor will shift, which is used as the transducing signals and monitored by a spectrometer. Among the four sensors, one is used as a reference for control experiments, and the others are used to detect A $\beta$ 42, T-tau and the mixture of A $\beta$ 42 and T-tau, respectively. All these experiments have been carried out three times, and the reported results are the average of the three measurements.

## Fabrication of the Sensor Chip

The fabrication process involves the following steps. (1) Fabrication of AAO thin film patterns as the sensing elements on glass substrate [12]: Aluminium thin film is deposited onto glass slides with E-beam evaporation. The aluminium is then transformed into AAO by electrochemical reaction in 0.3M Oxalic Acid, at 5.8 Celsius degree, for 2 hours. Photoresist AZ5214 is then spin-coated onto surface and patterned as protection layer. Device is then immersed into AAO etchant to etch the unprotected AAO away. AZ5214 is then washed away, leaving the patterns of AAO thin film exposed, followed by coating a layer of 10 nm Au. (2) Fabrication of microfluidic layer [13]: SU8-2075 is spin-coated onto glass slides with a thickness of 80  $\mu\text{m}$  and patterned using photolithography, resulting in a SU8 mold. Liquid PDMS with precursor to cure agent ratio of 9:1 is then deposited onto SU8 mold and cured at 65 Celsius for 2 hours. The PDMS microfluidic layer is peeled off from the mold. (3) The sensor chip is finally completed by bonding the PDMS microfluidic layer with the fabricated AAO thin film patterns on glass substrate after oxygen plasma treatment. The fabricated chip is shown in Fig. 2.2a. The close-up showing the four sensors, their inputs, their outputs and the microfluidic channels, and the nanopore thin film sensing elements is given Fig. 2.2b-c. The optical setup for the experiments is illustrated in Fig. 2.2d.

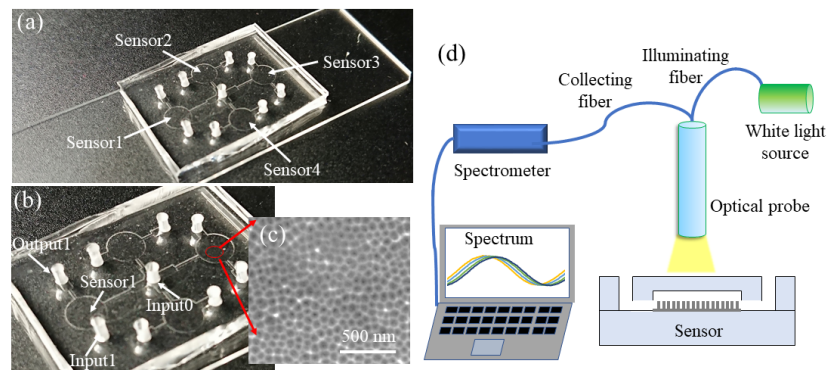


Fig. 2.2. (a) Photo of a fabricated chip with four sensors and microfluidic interface; (b) close-up showing the main inlet *Input0*, and sub-inlet *Input1* and sub-outlet *Output1* for Sensor1; (c) SEM image of the nanopores in each sensor; (d) the optical setup for the experiments.

### Sensor's Surface Functionalization Procedure

The sensor surface coated with 10 nm Au is functionalized with either A $\beta$ 42 or T-tau antibody through 1-ethyl-3-(3-dimethylaminopropyl) carbodiimide (EDC)/N-hydroxysulfosuccinimide (NHS) chemistry. As shown in Fig. 2.3, the Au-coated sensor surface is immersed in the 10 mM HSC10COOH/HSC8OH for overnight and then washed with ethanol and DI water. After the surface is dried, the surface is immersed in a solution of NHS and EDC (NHS 0.2M, EDC 0.05M) for 2 hours. The sensor surface is washed with DI water and then immersed in the 10  $\mu$ M antibody solution overnight. This is followed by loading of 100  $\mu$ L 1 M ethanolamine (EA) to block the non-occupied HSC10COOH/HSC8OH sites activated by the EDC/NHS. Finally, the sensor surface is rinsed with the PBS buffer to flush off non-specifically adsorbed proteins. At this stage, the sensor is ready for the measurement.

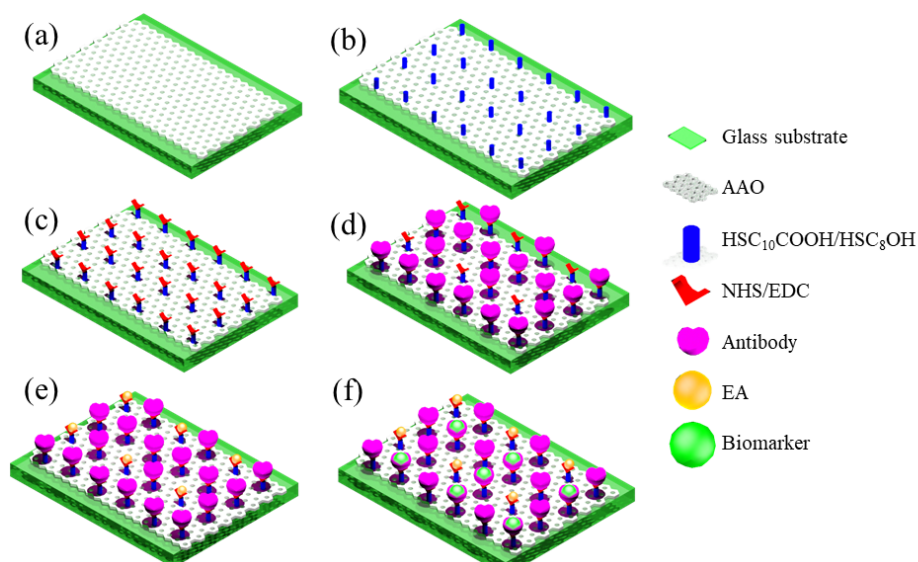


Fig. 2.3. Surface functionalization steps for the sensor surface from (a) to (e). In step (f), the biomarker is applied to the sensor.

Thereafter, A $\beta$ 42 or/and T-tau (in the buffer or CSF) will be applied to the sensors. After final sequential washes, the measurements will be taken. Experiments for negative controls are carried out to employ the full assay procedure but without the A $\beta$ 42 and T-tau.

## Chip Operational Procedure for Surface Functionalization and the Biomarker Detection

As shown in Fig. 2.1b and Fig. 2.2a, the chip consists of four sensors with one main inlet *Input0*. Each sensor has one sub-inlet and one sub-outlet. Use *Sensor1* in Fig. 2.2b as an example, it has one sub-inlet *Input1* and one sub-outlet *Output1*. From step *a* to step *c* in Fig. 2.3, the chemicals are flowed into chip through the *Input0* located in the center of chip to functionalize the surfaces of the four sensors simultaneously. For step *d* of coating antibody to the sensors in Fig. 2.3, the antibody is flowed to each sensor through its sub-inlet. For instance, for *Sensor1* on chip, the A $\beta$ 4 or T-tau antibody is flowed through its sub-inlet *Input1* to immobilize one specific antibody. Similarly, one specific antibody will be functionalized on the surfaces of *Sensor2*, *Sensor3* and *Sensor4*, respectively. This step allows different antibodies to be coated on each sensor, resulting in four A $\beta$ 42-sensors and/or T-tau-sensors, thereby enabling the multiplexed detection of different biomarker on the same chip simultaneously. The widths of the channels in the microfluidic network are properly designed so that the chemicals can be readily flowed to all four sensors through the main inlet *Input0*, but the chemicals through the sub-inlets can only be flowed to one specific sensor. For instance, in Fig. 2.2b, the chemical through *input1* can only be flowed to *Sensor1*.

As a demonstration of the microfluidic network, for the first few steps of surface functionalization, green food dye solution (used to mimic those chemicals) is flowed through main inlet *Input0* to four sensors on chip (Fig. 2.4a). For the antibody coating, orange food dye (used to mimic the antibody) is followed into *Sensor1* through its sub-inlet *Input1*, as shown in Fig. 2.4b. Similar procedure is used to coat the antibody to other sensors. Finally, the sample-to-be-detected is flowed into the chip through the main inlet *Input0*, and thus the sample can be detected by the four sensors simultaneously.

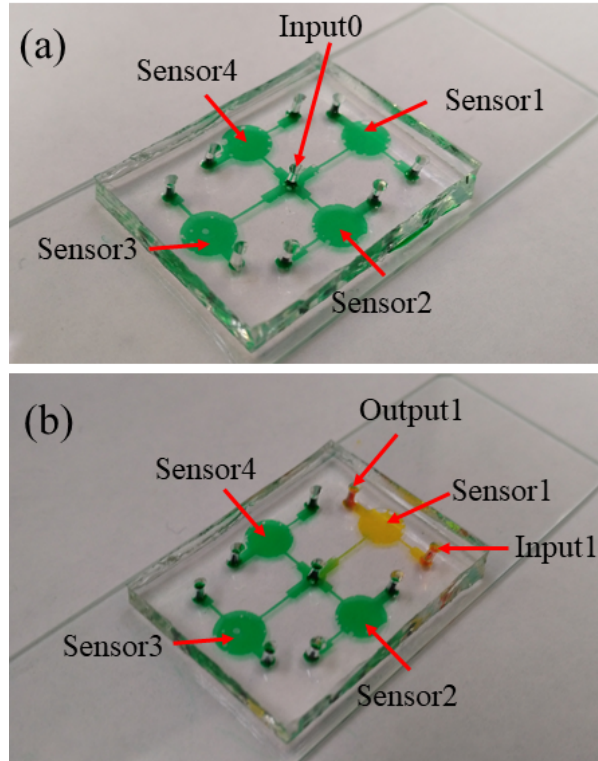


Fig. 2.4. Optical images showing how the microfluidic network works: (a) green food dye (mimic the chemicals) to be flowed through the main inlet *Input0* to all four sensors; (b) orange food dye (mimic the antibody) to be flowed to *Sensor1* through its sub-inlet.

### Instrumentation

The detection setup of the sensors in Fig. 2.2d is the same as those previously reported [14, 15]. A broadband light source from a tungsten halogen lamp is coupled to a specifically-designed optical fiber probe (Ocean Optics, Inc., Dunedin, FL, USA), which illuminates the sensor surface perpendicularly. The reflected signals (transducing signals) are collected by the same optical fiber probe, leading to an optical spectrometer (Ocean Optics, Inc.), which can detect the optical spectrum from 350 nm to 1050 nm. The spectrometer is connected to a laptop computer for data acquisition and processing. The biochemical samples are transported to the chip through the assembled plastic tubes (Upchurch Scientific, Inc.) by a syringe controlled by a pump (Harvard Apparatus, MA, USA).

## **Experimental Data Acquisition**

The average shift of the fringes for the measured transducing signals is obtained by (i) firstly obtaining the shift of each fringe peak relative to that of the blank Au-coated AAO surface or the shift after the antibody has been immobilized on the AAO surface, and (ii) averaging the shift of all the peaks to obtain the error bars for the measurements. The reference for each average shift is specified in the context in the following sections. The transducing signal of the same sample is measured at least on three sensors to obtain the average value.

## **Results**

### **Detection of A $\beta$ 42 in Buffer (A $\beta$ 42-buffer) and T-tau in Buffer (T-tau-buffer)**

A $\beta$ 42 of different concentrations in buffer have been detected. The A $\beta$ 42 is diluted in buffer provided by the ELISA Kit, resulting in a series of concentrations of 500 pg/ml, 250 pg/ml, 125 pg/ml, 62.5 pg/ml, 31.2 pg/ml, 15.6 pg/ml, 7.8 pg/ml, 3.9 pg/ml, respectively. The measured optical signals (fringe shift) are plotted in Fig. 2.5a. As shown, the fringe shift increases with the increasing concentrations of A $\beta$ 42. The shift is 6.5 nm when the concentration of A $\beta$ 42 reaches 500 pg/ml. As low as 7.8 pg/ml of A $\beta$ 42 can be readily detected, which is better than those of previously reported biosensors [7-9]. Similarly, the T-tau is diluted in buffer with a series of concentrations of 2000 pg/ml, 1000 pg/ml, 500 pg/ml, 250 pg/ml, 125 pg/ml, 62.5 pg/ml, 31.25 pg/ml, 15.6 pg/ml, respectively. The measured results are shown in Fig. 2.5b. It shows when the concentration of T-tau is 2000 pg/ml, the shift is 3.76 nm. The lowest concentration of T-tau can be detected is 15.6 pg/ml.

It should be noted that since the clinically relevant concentration range of A $\beta$ 42 for AD patients is  $382.2 \pm 102.0$  pg/ml [2-4] as aforementioned, the measurement range of the sensors from 7.8

pg/ml to 500 pg/ml is sufficient enough to cover this range. The clinically relevant concentration of T-Tau for AD patients is Age-dependent [2]. The following concentrations for normal T-tau levels have already been established [2]: <300 pg/ml for ages between 21 and 50 years old; <450 pg/ml for ages between 51 to 70 years old; and <500 pg/ml for ages between 70 and 93 years old. The measurement range of the sensor from 15.6 pg/ml to 2000 pg/ml can easily monitor the T-tau levels for AD patients. Hence, it is not critically important to further improve the detection limit of the sensor for both A $\beta$ 42 and T-tau.

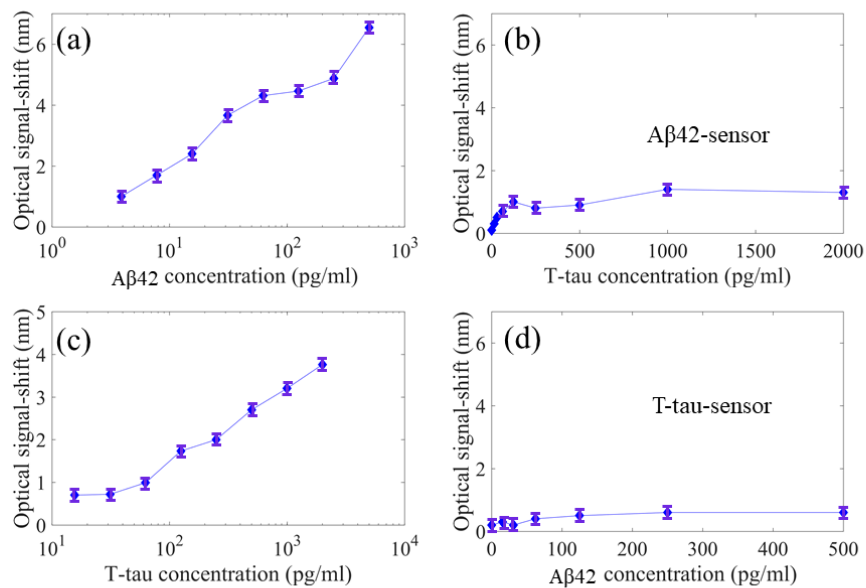


Fig. 2.5. (a) Measured transducing signals for an A $\beta$ 42-sensor to detect A $\beta$ 2 in buffer at different concentrations; (b) Measured transducing signals for an A $\beta$ 42-sensor to detect T-tau in buffer at different concentrations; (c) Measured transducing signals for a T-tau-sensor to detect T-tau in buffer at different concentrations; (d) Measured transducing signals for a T-tau-sensor to detect A $\beta$ 2 in buffer at different concentrations.

### Specificity Evaluation: A $\beta$ 42-buffer and T-tau-buffer

The specificity of the A $\beta$ 42 antibody functionalized sensors (*A $\beta$ 42-sensor*) has been evaluated by detecting T-tau-buffer. The measured optical signal for T-tau-buffer samples with different concentrations are given in Fig. 2.5c. The shift increases from 0.1 nm to 1.3 nm with the increased concentrations of T-tau from 0 pg/ml to 2000 pg/ml. Compared to the measured optical signals for

detecting A $\beta$ 42 in Fig. 2.5a, when the concentrations of A $\beta$ 42 increase from 0 pg/ml to 500 pg/ml, the shift increases from 1 nm to 6.5 nm, indicating very good specificity of the A $\beta$ 42-sensors. Similarly, the specificity of the T-tau antibody functionalized sensors (*T-tau-sensor*) has been examined by detecting A $\beta$ 42-buffer. The measured optical signal for A $\beta$ 42-buffer samples with different concentrations are given in Fig. 2.5d. The shift increases from 0.2 nm to 0.6 nm with the increased concentrations of A $\beta$ 42 from 0 pg/ml to 500 pg/ml. Compared to the measured optical signals for detecting T-tau in Fig. 2.5b, when the concentrations of T-Tau increase from 0 pg/ml to 500 pg/ml, the shift increases from 0.7 nm to 3.76 nm, indicating very good specificity of the T-tau-sensor. These measurements suggest that the assay is suitable for detecting A $\beta$ 42 and T-tau in a complex biofluid such as in CSF.

#### **Detection of A $\beta$ 42 in CSF (A $\beta$ 42-CSF) and T-tau in CSF (T-tau-CSF)**

Detection of the A $\beta$ 42 of different concentrations spiked in CSF has been carried out. A $\beta$ 42-CSF samples are prepared as the following procedure. The CSF is obtained from Pooled Human Donors, the CSF itself contains A $\beta$ 42, but its concentration is unknown. The diluted A $\beta$ 42 samples have the following known concentrations: 500 pg/ml, 250 pg/ml, 125 pg/ml, and 62.5 pg/ml. Then the same volume of the diluted A $\beta$ 42 is spiked to the same volume of CSF. As a result, four A $\beta$ 42-CSF samples (Sample1, Sample2, Sample3, and Sample4) are prepared but their exact concentrations of A $\beta$ 42 in these four samples have been changed and become unknown. Four A $\beta$ 42-buffer samples of the same known concentrations (500 pg/ml, 250 pg/ml, 125 pg/ml, and 62.5 pg/ml) are also prepared for the experiments.

The measured optical signals of A $\beta$ 42-CSF samples and A $\beta$ 42-buffer samples are given in Fig. 2.6a. As shown, at the same A $\beta$ 42 concentration but below 500 pg/ml, the shift of the optical signals for A $\beta$ 42-CSF samples is larger than that for A $\beta$ 42-buffer samples, indicating the A $\beta$ 42

exists in CSF before additional A $\beta$ 42 is spiked to CSF. When the concentration of the added A $\beta$ 42 in CSF and in buffer increases to 500 pg/ml, the shift of the optical signal from A $\beta$ 42-CSF samples becomes smaller than that from A $\beta$ 42-buffer samples. The A $\beta$ 42 concentration at the intersection point between the measured optical signals from the A $\beta$ 42-CSF samples and the A $\beta$ 42-buffer samples is the original A $\beta$ 42 concentration in CSF, which is  $\sim 400$  pg/ml (Fig. 2.6a).

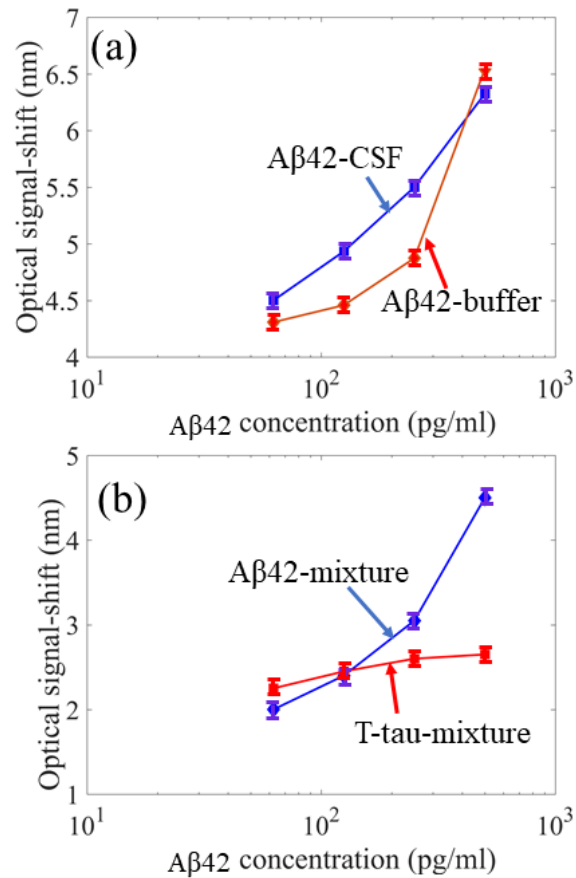


Fig. 2.6. (a) Measured transducing signals of A $\beta$ 42 spiked in buffer and CSF, respectively; (b) Measured transducing signals of A $\beta$ 42 in A $\beta$ 42-T-tau mixture using an A $\beta$ 42-sensor, measured transducing signals of T-tau in A $\beta$ 42T-tau-mixture using a T-tau-sensor, respectively.

A series of mixed samples is prepared by spiking both the diluted A $\beta$ 42-buffer and the diluted T-tau-buffer into CSF. Again, the diluted A $\beta$ 42-buffer samples have the following known concentrations: 500 pg/ml, 250 pg/ml, 125 pg/ml, and 62.5 pg/ml. The diluted T-tau-buffer samples have the same concentration of 1000 pg/ml. Then the same volume of the diluted A $\beta$ 42-

buffer sample and the same volume of the diluted T-tau-buffer sample are spiked to the same volume of CSF. Namely, the mixed volume ratio for them is: A $\beta$ 42-buffer: T-tau-buffer: CSF=1:1:1. As a result, four A $\beta$ 42-T-tau-CSF samples are prepared but their concentrations of A $\beta$ 42 and T-tau in the samples become unknown. Note that the CSF contains both A $\beta$ 42 and T-tau, hence the real concentrations of A $\beta$ 42 and T-tau in the four samples should be different from the concentrations of A $\beta$ 42-buffer samples and T-tau-buffer samples before they are spiked into the CSF samples. Specifically, since the volumes of the diluted A $\beta$ 42-buffer samples, the diluted T-tau-buffer samples and CSF are the same for preparing the mixed samples, the real concentrations of both A $\beta$ 42 and T-tau in the mixed samples have been further diluted.

These four samples have been detected by the A $\beta$ 42-sensor and the T-tau-sensor on chip, respectively. The measured optical signals from both sensors are plotted together in Fig. 2.6b. As shown, the measured optical signals for T-tau in the mixture (*A $\beta$ 42-T-tau-mixture*) have small variations, consistent with the same concentrations of T-tau in these mixed samples, again indicating the very good specificity of the T-tau-sensors. Otherwise, if the A $\beta$ 42 in the mixed samples can be efficiently bound to T-tau antibody, the change of the optical signals should be significant. In contrast, the optical signals for the A $\beta$ 42 in the mixture (*A $\beta$ 42-T-tau-mixture*) increases with its increased concentrations in the mixed samples as expected. In addition, the optical signal shifts for A $\beta$ 42 are smaller than those in Fig. 2.5a and Fig. 2.6a, confirming the real concentrations of A $\beta$ 42 in the mixture have been diluted in the mixed samples.

### **Multiplexed Detection of Samples Mixed with A $\beta$ 42 and T-tau in CSF**

To further demonstrate the multiplexed detection of A $\beta$ 42 and T-tau in the mimicking clinical samples, a series of samples has been prepared by spiking A $\beta$ 42 and T-tau at the clinically relevant concentration ranges into CSF. Before mixing, the diluted A $\beta$ 42-buffer samples are prepared with

concentrations of A $\beta$ 42 of 500 pg/ml, 250 pg/ml, 125 pg/ml, 62.5pg/ml, 31.25 pg/ml, and the T-tau-buffer samples with concentrations of T-tau of 2000 pg/ml, 1000 pg/ml, 500 pg/ml, 250 pg/ml, 125 pg/ml, respectively. Then the A $\beta$ 42-buffer sample, the T-tau-buffer sample, and CSF are mixed together with a volume ratio of 1:1:1. As a result, 25 mixed samples in CSF are prepared. These 25 samples have been detected by A $\beta$ 42-sensors and T-tau-sensors on chip, respectively.

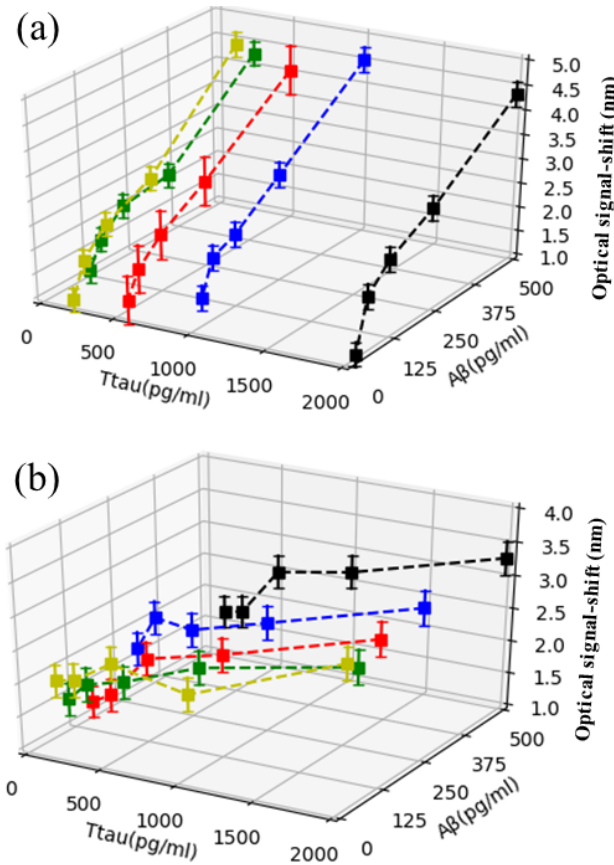


Fig. 2.7. (a) Measured transducing signals of A $\beta$ 42 in A $\beta$ 42-T-tau mixture using an A $\beta$ 42-sensor; (b) measured transducing signals of T-tau in A $\beta$ 42-T-tau-mixture using a T-tau-sensor.

The measured optical signals by A $\beta$ 42-sensors are plotted in Fig. 2.7a. As shown, for the samples spiked with the same concentration of A $\beta$ 42, the measured optical signals have small variations, indicating the very good specificity of the A $\beta$ 42-sensors. Otherwise, if the T-tau in the mixed samples can be efficiently bound to A $\beta$ 42 antibody, the change of the optical signals should be significant. On the other hand, for the samples spiked with the same concentration of T-tau, the

measured optical signals clearly increase with the increased concentrations of A $\beta$ 42 in the mixed samples. In addition, the optical signal shifts are consistent with those in Fig. 2.6b but smaller than those in Fig. 2.5a and Fig. 2.6a, confirming the real concentrations of A $\beta$ 42 in the mixed samples have been diluted.

The measured optical signals by T-tau-sensors are plotted in Fig. 2.7b. Similarly, for the samples spiked with the same concentration of T-tau, the measured optical signals have small variations, again indicating the very good specificity of the T-tau sensors. Otherwise, if the A $\beta$ 42 in the mixed samples can be efficiently bound to T-tau antibody, the change of the optical signals should be significant. For the samples spiked with the same concentration of A $\beta$ 42, the optical signals clearly increase with the increased concentrations of T-tau in the mixed samples.

All these measurements of the mixed samples demonstrate that these sensors can detect A $\beta$ 42 and T-tau in CSF successfully with very good specificity and repeatability, indicating the sensor can potentially detect them in the clinical samples.

## Discussion

In this effort, as a technical demonstration, four nanosensors on a chip have been fabricated. It should be noted that tens of nanosensors can be readily batch-fabricated on a chip inexpensively to increase the capacity for multiplexed detection if needed. The detection of two promising biomarkers A $\beta$ 42 and T-tau in buffer and in CSF for AD using these label-free optical nanosensors has been carried out. The typical detection time is less than 20 minutes after a biomarker is applied on the nanosensor, much faster than neuroimaging methods such as magnetic resonant imaging (MRI). It has been found that as low as 7.8 pg/ml of A $\beta$ 42 in buffer and 15.6 pg/ml of T-tau in buffer can be readily detected with high specificity and very good repeatability, and with much

lower detection limit than those of previously reported sensors. The detection of A $\beta$ 42 spiked in CSF has been performed. The measured optical signals show consistent larger shift for A $\beta$ 42-CSF samples than that of A $\beta$ 42-buffer samples at lower concentrations of the spiked A $\beta$ 42, while the shift becomes smaller for A $\beta$ 42-CSF samples than that for A $\beta$ 42-buffer samples at higher concentrations of the spiked A $\beta$ 42, which indicates the CSF itself contains A $\beta$ 42 and its concentration is estimated at  $\sim$ 400 pg/ml. Finally, the detection of the CSF samples spiked with both A $\beta$ 42 and T-tau has been demonstrated, suggesting the feasibility to monitor these biomarkers in clinical samples using the nanosensors. Furthermore, given its low cost and ease-of-operation with high sensitivity and specificity, this type of nanosensor can serve as a powerful point-of-care (POC) diagnostic tool if combined with the neuroimaging tool such as MRI. For instance, the nanosensor can serve as a POC equipment for early detection of the protein biomarkers in an efficient and cost-effective manner. If the sensor detects the changes of concentrations of the proteins that serve as Alzheimer's biomarkers, it is a good indication that further tests are required, making the MRI the next step in the patient's diagnosis and treatment. By this way, significant costs and time can be saved for patients, achieving more precision diagnostics of AD in a rapid and inexpensive way.

## References

- [1] M.S. Albert, S.T. DeKosky, D. Dickson, B. Dubois, H.H. Feldman, N.C. Fox, et al., "The diagnosis of mild cognitive impairment due to Alzheimer's disease: Recommendations from the National Institute on Aging-Alzheimer's Association workgroups on diagnostic guidelines for Alzheimer's disease," *Alzheimer's & dementia: the journal of the Alzheimer's Association*, vol. 7, no. 3, pp. 270-279, 2011.
- [2] C. Mulder, N.A. Verwey, W.M. van der Flier, F.H. Bouwman, A. Kok, E.J. van Elk, et al., "Amyloid- $\beta$  (1-42), total tau, and phosphorylated tau as cerebrospinal fluid biomarkers for the diagnosis of Alzheimer disease," *Clinical chemistry*, vol. 56, no. 2, pp. 248-253, 2010.
- [3] H. Hampel, and K. Blennow, "CSF tau and  $\beta$ -amyloid as biomarkers for mild cognitive impairment," *Dialogues in clinical neuroscience*, vol. 6, no. 4, pp. 379, 2004.

- [4] J.A. Mo, J.H. Lim, A.R. Sul, M. Lee, Y.C. Youn, H.J. Kim, et al., "Cerebrospinal Fluid  $\beta$ -Amyloid<sub>1-42</sub> Levels in the Differential Diagnosis of Alzheimer's Disease-Systematic Review and Meta-Analysis," *PloS one*, vol. 10, no. 2, pp. e0116802, 2015.
- [5] L. Song, D.R. Lachno, D. Hanlon, A. Shepro, A. Jeromin, D. Gemani, et al., "A digital enzyme-linked immunosorbent assay for ultrasensitive measurement of amyloid- $\beta$  1-42 peptide in human plasma with utility for studies of Alzheimer's disease therapeutics," *Alzheimer's research & therapy*, vol. 8, no. 1, pp. 58, 2016.
- [6] J.H. Kang, H. Vanderstichele, J.Q. Trojanowski, L.M. Shaw, "Simultaneous analysis of cerebrospinal fluid biomarkers using microsphere-based xMAP multiplex technology for early detection of Alzheimer's disease," *Methods*, vol. 56, no. 4, pp. 484-493, 2012.
- [7] A. Kaushik, R.D. Jayant, S. Tiwari, A. Vashist, M. Nair, "Nano-biosensors to detect beta-amyloid for Alzheimer's disease management," *Biosensors and Bioelectronics*, vol. 80, pp. 273-287, 2016.
- [8] P. Gagni, L. Sola, M. Cretich, M. Chiari, "Development of a high-sensitivity immunoassay for amyloid-beta 1-42 using a silicon microarray platform," *Biosensors and Bioelectronics*, vol. 47, pp. 490-495, 2013.
- [9] M.R. Sierks, G. Chatterjee, C. McGraw, S. Kasturirangan, P. Schulz, S. Prasad, "CSF levels of oligomeric alpha-synuclein and beta-amyloid as biomarkers for neurodegenerative disease," *Integrative Biology*, vol. 3, no. 12, pp. 1188-1196, 2011.
- [10] T. Zhang, Z. Gong, R. Giorno, L. Que, "A nanostructured Fabry-Perot interferometer," *Optics express*, vol. 18, no. 19, pp. 20282-20288, 2010.
- [11] T. Zhang, Y. He, J. Wei, L. Que, "Nanostructured optical microchips for cancer biomarker detection," *Biosensors and Bioelectronics*, vol. 38, no. 1, pp. 382-388, 2012.
- [12] H. Yin, X. Li, and L. Que, "Fabrication and characterization of aluminum oxide thin film micropatterns on the glass substrate," *Microelectronic Engineering*, vol. 128, pp. 66-70, 2014.
- [13] Y. Xia and G.M. Whitesides, "Soft lithography," *Annual review of materials science*, 1998. vol. 28, no.1, pp. 153-184.
- [14] Y. He, X. Li, and L. Que, "A transparent nanostructured optical biosensor," *Journal of biomedical nanotechnology*, 2014. vol. 10, no. 5, pp. 767-774, 2014.
- [15] T. Zhang, P. Pathak, S. Karandikar, R. Giorno, L. Que, "A polymer nanostructured Fabry-Perot interferometer based biosensor," *Biosensors and Bioelectronics*, vol. 30, no. 1, pp. 128-132, 2011.

## CHAPTER 3. NANOPORE THIN FILM ENABLED OPTICAL PLATFORM FOR DRUG LOADING AND RELEASE

Chao Song, Xiangchen Che, and Long Que. *Optics Express*, vol. 25, no. 16, pp. 19391-19397, 2017.

### Abstract

In this paper, a drug loading and release device fabricated using nanopore thin film and layer-by-layer (LbL) nanoassembly is reported. The nanopore thin film is a layer of anodic aluminum oxide (AAO), consisting of honeycomb-shape nanopores. Using the LbL nanoassembly process, the drug, using gentamicin sulfate (GS) as the model, can be loaded into the nanopores and the stacked layers on the nanopore thin film surface. The drug release from the device is achieved by immersing it into flowing DI water. Both the loading and release processes can be monitored optically. The effect of the nanopore size/volume on drug loading and release has also been evaluated. Further, the neuron cells have been cultured and can grow normally on the nanopore thin film, verifying its bio-compatibility. The successful fabrication of nanopore thin film device on silicon membrane render it as a potential implantable controlled drug release device.

### Introduction

Ideally for many diseases, including various ocular diseases, some chronic diseases and coronary heart disease, the controlled dose of drugs can be delivered locally for a sustained treatment [1-2]. Toward this goal, a variety of nanostructured materials, devices and systems have been developed to fulfil this requirement [3-7]. Among them, the nanoporous structure such as the porous Si has been used as a controlled drug delivery device [2]. Another widely used technology for controlled drug release is to synthesize capsules for the nanoscale-sized drugs, which is

achieved by coating the drugs with multiple layers of chemicals by a layer-by-layer (LbL) nanoassembly process [8-9]. LbL nanoassembly process is based on the electrostatic attraction between oppositely charged polyelectrolytes. It is a simple yet powerful way for fabricating micrometer diameter shells/capsules to encapsulate drugs. Usually the wall permeability of synthesized capsules can be readily modified either by the chemical structures of the wall compositions or by external stimuli [8-10], which include pH and light. Specifically, by changing the pH of the solution around the chemically encapsulated drugs or using the light illumination to the capsules of drug, the nanopores inside the capsules can be dynamically changed or the wall of the capsules can be broken partially, facilitating the controlled drug release. Anodic aluminium oxide (AAO) nanopore, another nanoporous structure, is also an ideal drug delivery system with the following properties [11]. First, its nanopore size and volume can be easily modified; second, various drug loading to the nanopore structure is easy to carry out with simple chemical modifications; and finally, AAO is biocompatible. In addition, a unique property of AAO nanopore thin film is its ability to optically report on the loading or the release of a molecule or a drug within or from the porous nanostructure due to the change of the effective refractive index of the nanostructures [12]. In this paper, drug loading and release enabled by the AAO nanopore thin film and layer-by-layer (LbL) nanoassembly is reported. In addition, the effect of the nanopore size/volume on the release time has also been studied. Finally, the biocompatibility of the device and the successful fabrication of AAO nanopore thin film on silicone membrane have been demonstrated, indicating this type of device can be used as an implantable drug delivery device for localized drug treatment for an extended period of time.

## Materials and Methods

Sketch showing how to load the drug to and release drug from the AAO nanopore thin film-based device is illustrated in Fig. 3.1. Drug model gentamicin sulfate (GS) is stored in the nanopores and in the stacked between poly (acrylic acid) (PAA) and chitosan (CHI) layers. The chemicals PAA, GS, CHI, and phosphate-buffered saline (PBS) are all purchased from Sigma. Concentrations of PAA, GS, and CHI are prepared to be 2mg/ml, 5mg/ml, and 0.12mg/ml, diluted in PBS 6.5.

The drug loading process is illustrated in Fig. 1(a). During this process, an LbL nanoassembly process [13] is carried out. PAA, GS, PAA and CHI are applied onto the Au-coated nanopore thin film device in sequence and repeatedly. Due to their opposite charges and attractive electrostatic force among them, layers of [PAA/GS/PAA/CHI] is formed. Briefly, after PAA is applied for 5 minutes on the Au-coated nanopore thin film surface, a two- consecutive rinse step with PBS 6.5 is followed. The rinse ensures the less firmly bonded chemical PAA to be removed from the surface, allowing the next chemical layer GS deposition.

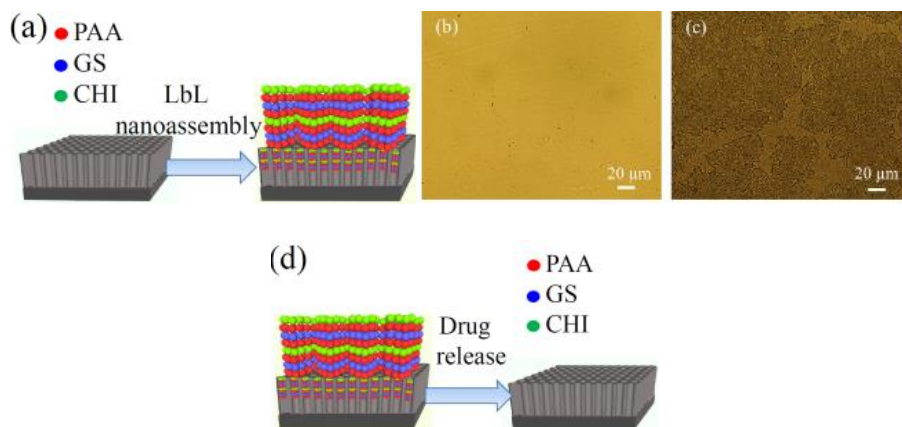


Fig. 3.1. (a) preparation of AAO nanopore-thin film drug release device using LbL nanoassembly process (not to scale); optical micrographs showing the surfaces of the nanopore thin film (b) before and (c) after LbL nanoassembly process; (d) the drug release process (not to scale).

Similarly, two consecutive rinse is carried out after the GS layer is formed before next layer of chemical is deposited. Following the same procedure, ten layers of [PAA/GS/PAA/CHI] combination are deposited in the whole loading process, resulting in totally forty layers of chemicals deposited onto the nanopore thin film surface. Fig. 3.1b-c gives the optical micrographs of the surface of the nanopore thin film before and after the ten layers of [PAA/GS/PAA/CHI] combination have been deposited. Due to the nature of AAO nanopores [18], the deposition of each chemical layer on the nanopore surface can be monitored by measuring the reflectance signals from the sample. The drug release process is illustrated in Fig. 3.1d. The sample is immersed into flowing DI water, which is utilized as the release solution. The release procedure can also be optically monitored by measuring the reflectance signals from the sample.

The optical setup for monitoring the drug loading and release is shown in Fig. 3.2. It consists of a white light source, an optical fiber spectrometer, an optical fiber illuminating and collecting probe and a laptop computer.

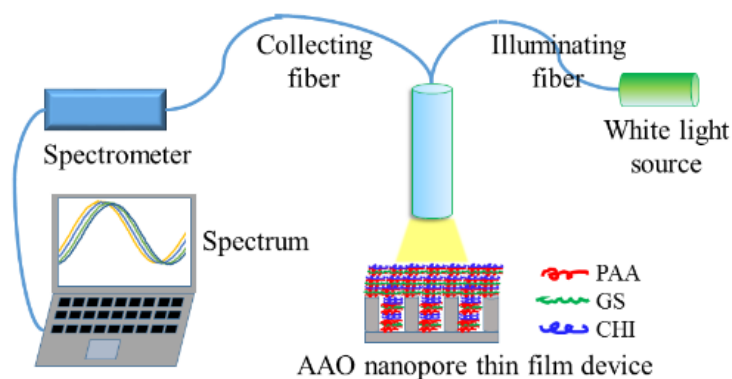


Fig. 3.2. Illustration of the setup for optical monitoring of drug loading and release process for an AAO nanopore thin film device.

When the drug along with PAA and CHI is loaded to the nanopores and/or deposited on the nanopore thin film surface layer-by-layer, the effective refractive index of the device is changed. As a result, the reflectance optical interference fringes from the device shift [14], which can be

optically monitored. Similarly, when the drug (GS) is released from the device, namely the layers of GS/PAA/CHI is dissolved, again resulting in the optical signals' change of the device.

## Results and Discussion

AAO nanopore thin film device for drug loading and release: During the drug loading process, [PAA/GS/PAA/CHI] layer is repeatedly deposited ten times on the nanopore thin film. The measured reflectance optical signals for each [PAA/GS/PAA/CHI] layer is shown in Fig. 3.3a. In Fig. 3.3a, one of the peaks of optical signal from bare AAO nanopore thin film at wavelength of 609 nm is selected as the reference peak. In the first two layers of [PAA/GS/PAA/CHI] deposition, the peak shifts to 607.8 nm. Starting from the third layer of deposition, the peak has a redshift eventually to 612.3 nm after deposition of the tenth layer, respectively. Overall, the peak has a blueshift of 1.2 nm and then has a redshift of 4.5 nm, leading to a net 3.3 nm redshift.

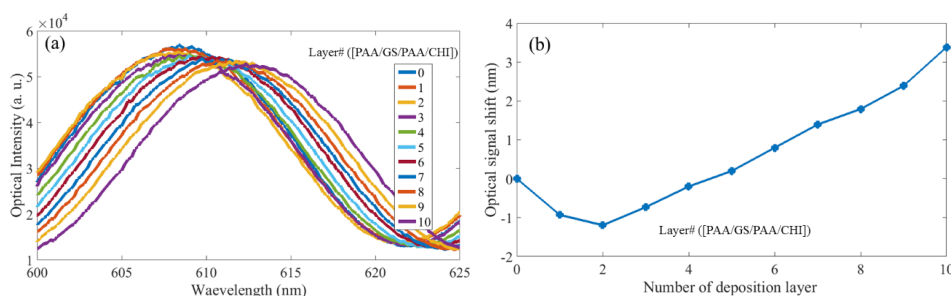


Fig. 3.3. (a) Measured optical signals after each [PAA/GS/PAA/CHI] deposition cycle: clear optical signal peak shift is observed; (b) the shift of wavelength peak, relative to 609 nm, for each cycle of deposition.

Fig. 3.3b shows almost linear increase of wavelength (i.e., peak red-shift) from the third layer to tenth layer deposition. The relationship of refractive index, thickness and resonant wavelength of this device is [15]:  $2(n_3t+n_2d-n_1t-n_0d) = m\lambda$  (1), where  $n_3$  is the effective refractive index of AAO,  $n_2$  is the effective refractive index of chemicals on AAO surface,  $n_1$  is the effective

refractive index of chemicals filled in nanopores,  $n_0$  is the effective refractive index of chemicals deposited above nanopores,  $t$  is the thickness of AAO structure and  $d$  is the chemicals thickness on surface of AAO. As seen from Fig. 3.3b, the resonant wavelength peak shifts from 607.8 nm to 612.3 nm, suggesting that  $n_2d$  increases linearly while other items remain unchanged in equation (1). This indicates that [PAA/GS/PAA/CHI] layer is deposited on the surface of AAO thin film uniformly and the thickness of chemical layers increases linearly, consistent with previous work of other researchers [2]. However, for the first two layers chemical deposition as shown in Fig. 3.3b, it shows a linear decrease of wavelength (i.e., peak blueshift). In the process of first two layers, chemicals are not only deposited on the surface of AAO, they are also trapped into the nanopores of AAO. The nanopore would accommodate a certain amount of chemicals, chemicals deposited onto the surface is less than chemicals trapped into nanopore. This leads to a blueshift of the resonant wavelength. After first two layers deposition, nanopore is filled with chemicals and no more chemical can be trapped into nanopore. Therefore, chemicals can only be deposited on the surface of AAO due to the attraction force between positive and negative charges, which leads to a redshift.

Drug release process is facilitated by flowing DI water through the devices. As shown in Fig. 3.4a, for the first 2 minutes, the peak has a blueshift of 1nm. Because of change with solution from PBS 6.5 to DI water, chemical ionization changes. The bonding force due to charge attraction becomes weak and deposited chemicals on AAO nanopore surface are dissolved, leading to drug release, resulting in a wavelength blueshift. In the next 8 minutes, the peak has a very small blueshift, approximately 0.5 nm. Peak shift has been observed for next 120 minutes, 600 minutes, 1440 minutes, and 2800 minutes. During this period of time, the peak has a redshift rather than a blueshift, which suggests the chemicals/drug stored inside the nanopores started to be released into

the DI water. The much longer release time for them indicates that it is difficult for the chemicals/drug inside the nanopores to be released into the DI water, in comparison with the chemicals/drug stored in the layers deposited on the AAO nanopore surface. The wavelength peak shift during the whole release process is summarized in Fig. 3.4b.

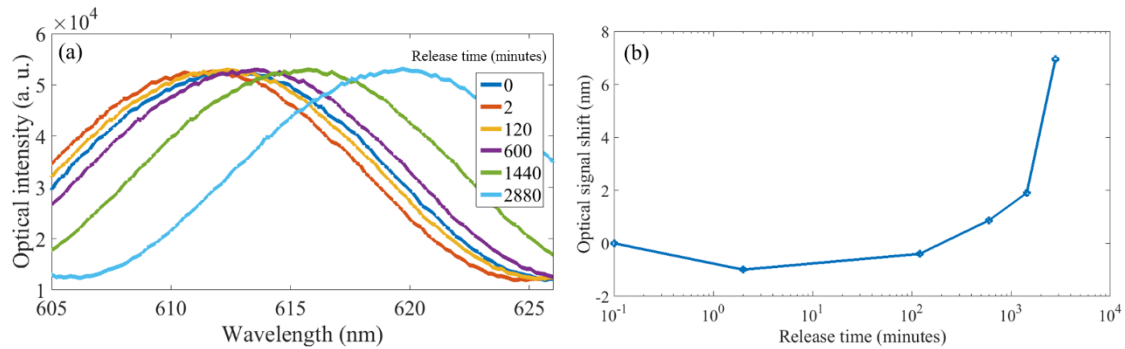


Fig. 3.4. (a) Measured optical signals from the device after chemical/drug releasing through DI water at 0, 2, 120, 600, 1440, 2880 minutes, resulting in clear peak shift; (b) and the corresponding shifts at different release time.

Nanopore size/volume effect on drug loading and release: In order to evaluate the nanopore size/volume effect on the drug loading and release, AAO nanopore thin film devices with two different sizes ( $\sim 10$ nm and  $\sim 50$ nm) have been fabricated. SEM images of the nanopore thin film devices are shown in Fig. 3.5a. The device with enlarged pore size is supposed to provide larger volume to accommodate more drugs, and thus achieve longer release time.

As shown in Fig. 3.5c-d, the measured optical signals of these two devices show the similar trend in both drug loading process and release process. During the loading process, the optical peak has blueshift in the first two layers and then redshift in the next eight layers. On the other hand, during the release process, the optical peak has blueshift in the first two minutes and then redshift until the releasing procedure is completed. But, for the Device2 with larger nanopore size ( $\sim 50$  nm), its optical peak shifts during the loading process and release process of the Device2 are significantly larger than those of the Device1 of smaller nanopore size ( $\sim 10$  nm). The larger shift

indicates that more chemicals can be stored in the device, and thus larger dose of drug can be delivered for the same period of time (Fig. 3.5d). Hence, both the amount and the duration of the drug delivery can be modified by using AAO nanopore thin film with different nanopore size/volume to accommodate different amount of drugs. In these experiments, the time used for monitoring the drug release from these devices is only from 0 to 2800 minutes. As can be seen in Fig. 3.5d, even after 2800-minute release, the shift of the optical signals for both Device1 and Device2 still do not tend to become saturated, indicating that some drugs in both devices still remain to be released for an extended period of time.

Evaluation of biocompatibility of AAO nanopore thin film: In order to prove the biocompatibility of the devices based on AAO nanopore thin film as potential implantable devices, the neuron cells have been cultured on the AAO nanopore thin film. Briefly, immortalized rat mesencephalic cells (1RB3AN27, N27 for short) are grown in RPMI medium supplemented with 10% fetal bovine serum, 1% L -glutamine, penicillin (100 U/ml), and streptomycin (100 U/ml), maintained at 37°C in a humidified atmosphere of 5% CO<sub>2</sub>. Before we seed cells from the flask to AAO nanopore thin film, trypsin is used to detach the cells from the bottom of flask. After 2 or 3 minutes, we pipette normal medium with 10% fetal bovine serum to the flask. Then the cells are seeded to AAO nanopore thin film. An optical image of neuron cells (N27) cultured on AAO nanopore thin film is shown in Fig. 3.6. Clearly the cells can spread and grow normally, verifying the good biocompatibility of the AAO nanopore thin film.

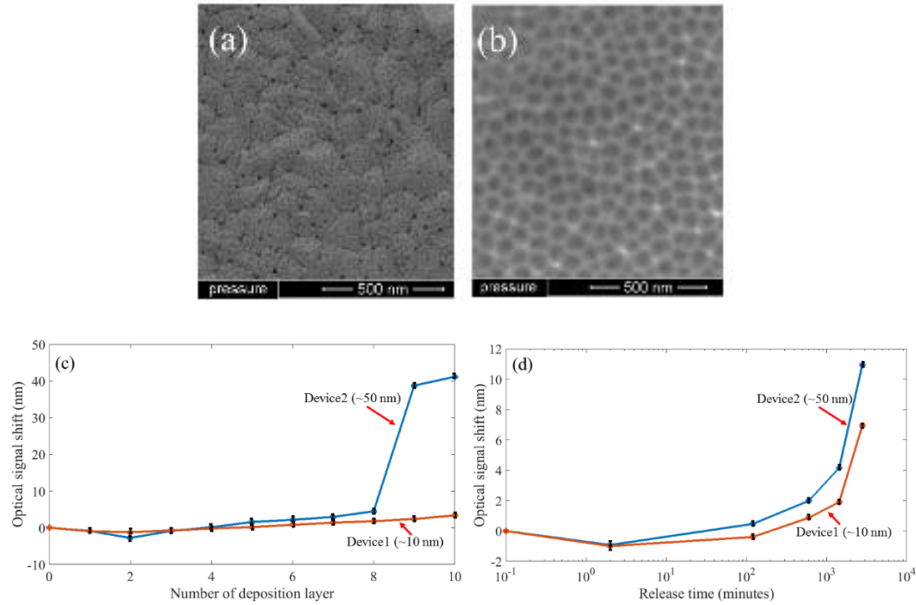


Fig. 3.5. (a) SEM images for AAO devices with nanopore size of ~10 nm and ~50 nm, respectively; (b) measured shift of optical signals for the devices during the LbL loading process; (c) the measured peak shifts after chemical/drug releasing through DI water at different release time.

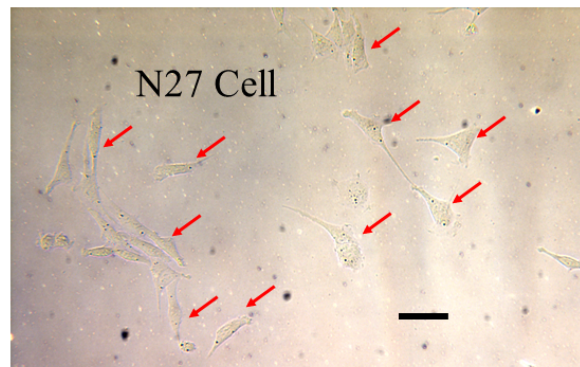


Fig. 3.6. Optical image showing the neuron cells' (N27 cells pointed by red arrows) growth on AAO thin film device.

Transferring of AAO nanopore thin film to silicone membrane: Even though the fabricated AAO nanopore thin film on the glass substrate can be peeled off, but it is quite crispy and easy to become curly and thus damaged (Fig. 3.7a), in order to make implantable or wearable AAO nanopore thin film device, the nanopore thin film need to be transferred to biocompatible substrate from the glass substrate. To this end, a process has been developed to transfer the AAO nanopore thin film to the silicone substrate (Fig. 3.7b). The transferring process can be briefly summarized

as the following: After the AAO nanopore thin film fabricated on glass substrate, the liquid adhesive PDMS-silicone membrane is applied uniformly on the nanopore thin film. After curing PDMS-silicone, the nanopore thin film along with the PDMS-silicone membrane can be gently peeled off the glass substrate. To verify the nanopore thin film is not damaged, the reflected optical signal from the thin film on silicone has been measured. As shown in Fig. 3.7c, the optical interference fringes can be observed, similar to that of AAO nanopore thin film on glass substrate [22]. While for the PDMS-silicone membrane without AAO nanopore thin film, no inference fringes can be observed. Further, it has been found no damages are observed after the nanopore thin film on PDMS-silicone membrane has been cyclically bent.

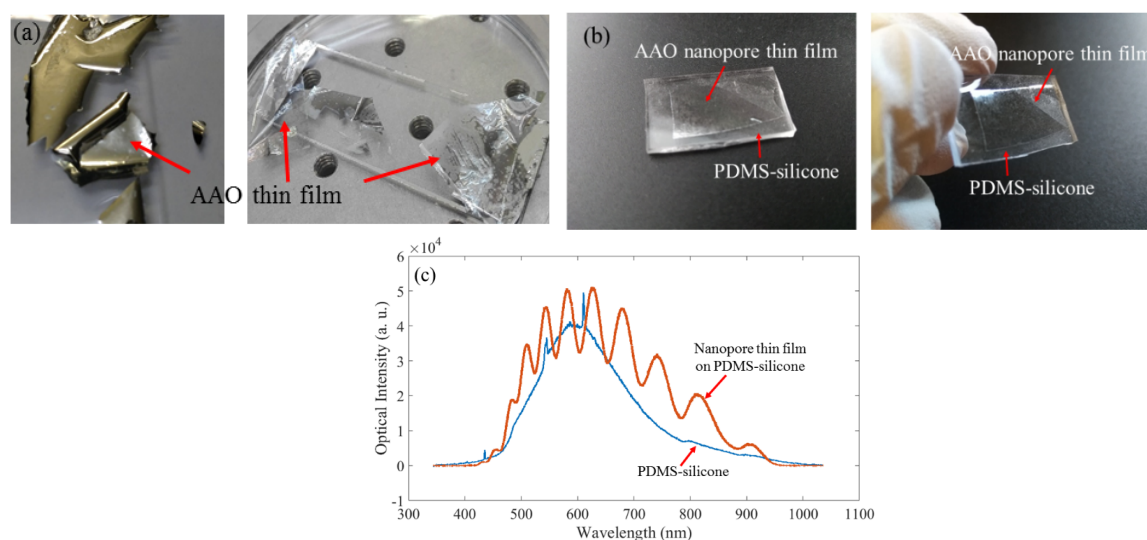


Fig. 3.7. (a) photos showing the nanopore thin films peeled off glass substrate are damaged and/or become curly; (b) photos showing nanopore thin film transferred on PDMS-silicone; (c) measured optical signals indicate the nanopore thin film perfectly transferred to PDMS-silicone membrane.

## Conclusions

In this paper, a drug loading and release device based on AAO nanopore thin film and LbL nanoassembly is reported. Both drug loading and release processes can be monitored optically for this type of device. The nanopore size effect on the drug loading and release has been evaluated. The drug release time can be readily up to three days by using only 10 layers LbL nanoassembly

to load the drugs to the AAO nanopore thin film devices with nanopore size from ~10 nm to ~50 nm. The bio-compatibility of AAO nanopore thin film has been demonstrated by culturing neuron cells on its surface. Further, AAO nanopore thin film has been successfully transferred to PDMS-silicone membrane, indicating the AAO nanopore thin film-based device can be used as an implantable device for drug delivery.

## References

- [1] L. Levy, Y. Sahoo, K. Kim, E.J. Bergey, and P.N. Prasad, "Nanochemistry: synthesis and characterization of multifunctional nanoclincs for biological applications." *Chemistry of Materials*, vol. 14, no. 9, pp. 3715-3721, 2002.
- [2] E. Wu, J.S. Andrew, L. Cheng, W.R. Freeman, L. Pearson, and M.J. Sailor, "Real-time monitoring of sustained drug release using the optical properties of porous silicon photonic crystal particles." *Biomaterials*, vol. 32, no. 7, pp. 1957-1966, 2011.
- [3] O. Farokhzad, and R. Langer, "Impact of Nanotechnology on Drug Delivery," *ACS Nano*, vol. 3, no. 1, pp. 16-20, 2009.
- [4] D. LaVan, T. McGuire, and R. Langer, "Small-scale systems for in vivo drug delivery," *Nature biotechnology*, vol. 21, no. 10, pp. 1184-1191, 2003.
- [5] F. Tian, J. Min, J. Kanka, X. Li, P.T. Hammond, and H. Du, "Lab-on-fiber optofluidic platform for in situ monitoring of drug release from therapeutic eluting polyelectrolyte multilayers," *Optics express*, vol. 23, no. 15, pp. 20132-20142, 2015.
- [6] R.K. Verma, S. Arora, S. Garg, "Osmotic pumps in drug delivery," *Crit. Rev. Ther. Drug Carrier Syst*, vol. 21, pp. 477- 520, 2004.
- [7] A.N. Zelikin, "Drug releasing polymer thin films: new era of surface-mediated drug delivery," *ACS Nano*, vol. 4, no. 5, 2494-2509, 2010.
- [8] H. Ai, S. Jones, M. de Villiers, Y. Lvov, "Nano-encapsulation of furosemide microcrystals for controlled drug release," *Journal of Controlled Release*, vol. 86, pp. 59-66, 2003.
- [9] B. Radt, T. Smith, and F. Caruso, "Optically addressable nanostructured capsules," *Advanced Materials*, vol. 16, pp. 23- 24, 2004.
- [10] Y. Lvov, A. Antipov, A. Mamedov, H. Mohwald, and G. Sukhorukov, "Urease encapsulation in nanoorganized microshells," *Nano Letters*, vol. 1, pp. 125-128, 2001.
- [11] A. Jani, D. Losic, and N. H. Voelcker, "Nanoporous anodic aluminium oxide: advances in surface engineering and emerging applications," *Progress in Materials Science*, vol. 58, no. 5, pp. 636-704, 2013.
- [12] T. Zhang, Z. Gong, R. Giorno, and L. Que, "A nanostructured Fabry-Perot interferometer," *Optics express*, vol. 18, no. 19, pp. 20282-20288, 2010.
- [13] W. Cheng, Yuan He, An-Yi Chang, and Long Que. "A microfluidic chip for controlled release of drugs from microcapsules." *Biomicrofluidics*, vol. 7, no. 6, pp. 0641021-06410210, 2013.
- [14] Y. He, X. Li and L. Que, "A transparent nanostructured optical biosensor," *Journal of Biomedical Nanotechnology*, vol. 10, no. 5, pp. 767-774, 2014.
- [15] M. Born, and E. Wolf, Principal of Optics, *John Wiley & Sons, Inc.*, 2000.
- [16] H. Yin, X. Li and L. Que, "Fabrication and characterization of aluminum oxide thin film micropatterns on the glass substrate," *Microelectronic Engineering*, vol. 128, pp. 66-70, 2014.

## CHAPTER 4. A FLEXIBLE NANOPORE THIN FILM ENABLED DEVICE FOR PRESSURE SENSING AND DRUG RELEASE

Chao Song, Pan Deng, Xiaoke Ding, and Long Que. *IEEE Transactions on Nanotechnology*, vol. 17, no. 5, pp. 962-967, 2018.

### Abstract

A new multifunctional flexible nanopore thin film device for both drug release and pressure sensing is reported. Different from previously reported drug release device based on the nanopore thin film fabricated on rigid substrates, this new flexible device offers two functions: it not only can serve as a drug delivery device, but also can be used as a pressure sensor as well. Specifically, the periodically distributed honeycomb- shape nanopores in the device are used to store the drugs, facilitating the extended drug release. In addition, the applied pressure on the device deforms the nanopore thin film, causing the change of the incident angle of the illuminating optical light on the device surface. As a result, the reflected optical interference fringes from the device shift, which is used as a pressure transducing signal. It has been found that the pressure sensitivity is  $\sim 0.01$  nm/mmHg, and the drug release can be easily extended to three weeks for this type of flexible nanopore thin film devices.

### Introduction

Usually on-chip devices and electronic circuits are fabricated exclusively on rigid substrates with little mechanical flexibility. However, for some specific applications such as wearable devices, devices fabricated on elastic substrates will be much suitable and favored. To this end, for recent decades, fabrication of devices on deformable polymer substrates has given birth to the flexible device technology [1]. For instance, a variety of photonic devices has been fabricated on

flexible substrates, including waveguides, microdisk resonators, add-drop filters and photonic crystals [2]. This progress on the 3D monolithic photonic integration technique on plastic substrates paves a way for opening up a variety of new application venues such as high-bandwidth-density optical interconnects, conformal wearable sensors and ultrasensitive strain gauges. Flexible fluorescence sensors have been developed and demonstrated recently [3]. This technology may play an important role in developing some wearable diagnostic tools for monitoring the diseases based on fluorescence detection. And piezoresistive strain sensors have also been fabricated on plastic substrates [4]. This type of flexible strain sensor can be potentially integrated with stretchable or curvilinear substrates to enable some demanding strain mapping for biomedical applications and could be potentially used for intraocular pressure (IOP) monitoring [5], which is critical for diagnosis of glaucoma and monitoring of glaucoma treatment [6]. Nowadays, the flexible device technology has been widely used to fabricate different types of devices or sensors and has already demonstrated its significant impact on wearable sensing and drug delivery system among others [7-8]. Herein, a new type of flexible nanopore device for both drug release and pressure sensing is reported.

### **Materials, Methods and Device Description**

The materials used for fabricating flexible nanopore thin film (FLEX-nanopore-TF) include Polydimethylsiloxane (PDMS) (ELLSWORTH, Inc.) and high purity Al (IAM, Inc.). The materials used for drug release include Drug model gentamicin sulfate (GS), poly(acrylic acid) (PAA) and chitosan (CHI). All of them are purchased from Sigma, Inc.

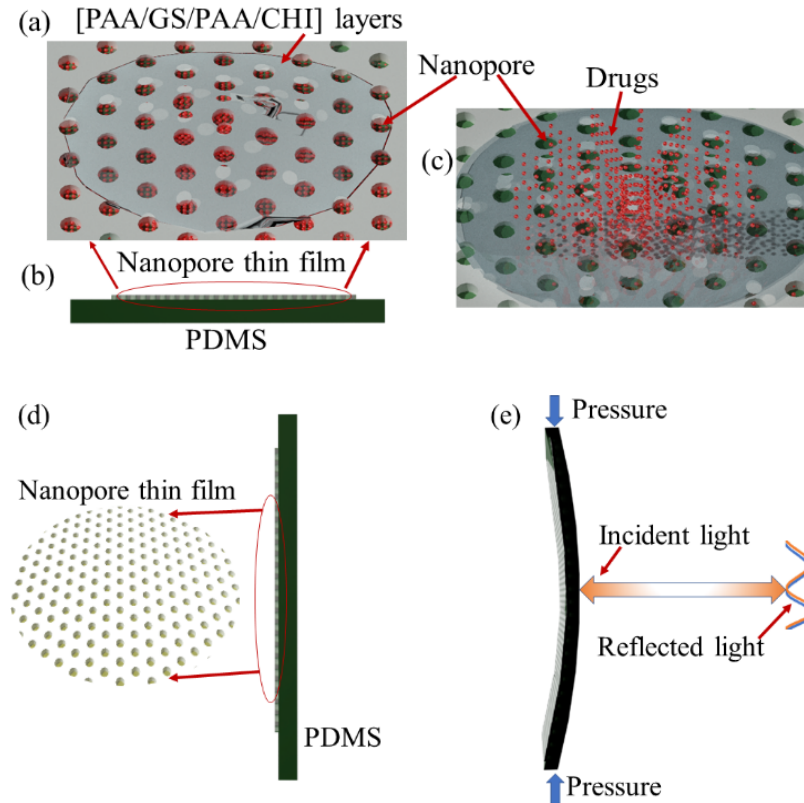


Fig. 4.1. Sketch of proposed FLEX-nanopore-TF (a-c) as a drug delivery device: drugs are stored inside the nanopores and the stacked nanoscale [PAA/GS/PAA/CHI] layers. The drugs are released by flowing water across the device; (d-e) as a pressure sensor: the shift of the interference fringes of the reflected optical signal as the transducing signal for pressure sensing.

The sketch of the FLEX-nanopore-TF device is illustrated in Fig. 4.1. The FLEX-nanopore-TF contains a layer of periodically distributed honeycomb-shape nanopores, which is anodic aluminum oxide (AAO) fabricated from an aluminum thin film using a two-step anodization process [9-11] and is tightly bonded to a layer of PDMS. As a drug delivery device, the nanopores in the FLEX-nanopore-TF are used to store drugs for extended drug release (Fig. 4.1a-c). The drugs are loaded into the nanopores and/or stacked on the surface of the nanopore thin film by layer-by-layer (LbL) nanoassembly [9-10].

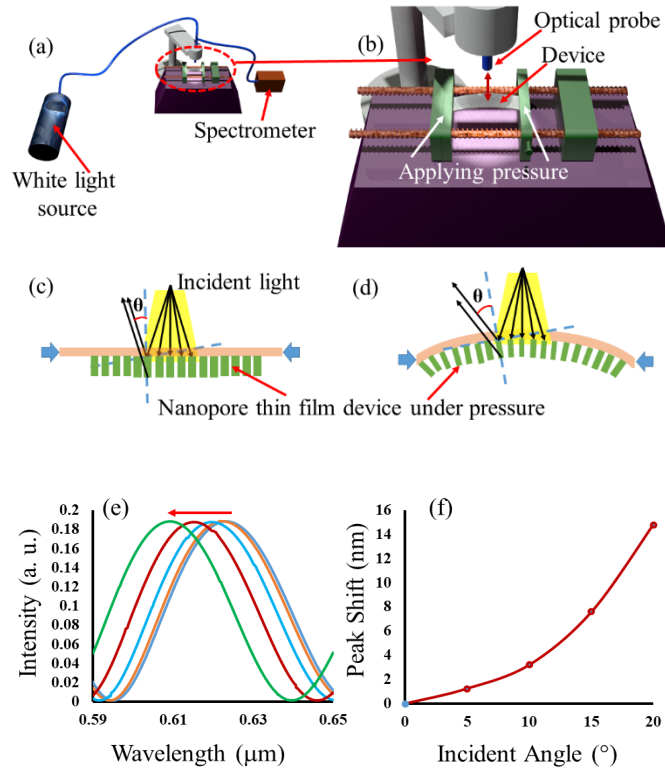


Fig. 4.2. (a-b) Setup and its close-up for optical monitoring of the pressure applied on a FLEX-nanopore-TF device; (c-d) incident angle of the illuminating light changes with the bending of the FLEX-nanopore-TF device under applied pressure; (e-f) modeling results: the optical interference fringes reflected from the FLEX-nanopore-TF device shift when the incident angles change.

Meanwhile, as a pressure sensor, the nanopore thin film is used to optically monitor the pressure applied on the device (Fig. 4.1d-e). The illuminating light is perpendicular to the flat surface of the FLEX-nanopore-TF device, and the transducing signal is the reflected optical signal from the surface (Fig. 4.2a-b). When a pressure is applied on the FLEX-nanopore-TF device, a curvature of the FLEX-nanopore-TF device is formed due to its bending. As a result, the incident angle  $\theta$  of the illuminating light changes (Fig. 4.2c-d). Because of the changes of the incident angle  $\theta$  under different pressures, the peaks of the interference fringes of the reflected optical signal shift due to changes of the optical path [12]. The shift of the interference optical signal is used as the pressure transducing signal. Detailed optical model of FLEX-nanopore-TF device showing pressure sensing is given in Fig. 4.2c-d without applied pressure and with an applied pressure, respectively.

One representative modeling result based on rigorous coupled-wave analysis (RCWA) using RSoftTM is shown in Fig. 2e-f [13]. In this model, the FLEX-nanopore-TF device is measured 18 mm long, 13 mm wide and 1.5 mm thick. The nanopore size is 50 nm in diameter, and the interspacing among nanopore is 100 nm. As shown, when the FLEX-nanopore-TF device is deformed horizontally by applying axial pressure  $P$ , the incident angle of the illuminating light is changed from  $0^\circ$  to  $5^\circ$ ,  $10^\circ$ ,  $15^\circ$  and  $20^\circ$ , as a result, the shift of the optical signal is 1.2 nm, 3.2 nm, 7.6 nm, 14.8 nm, respectively.

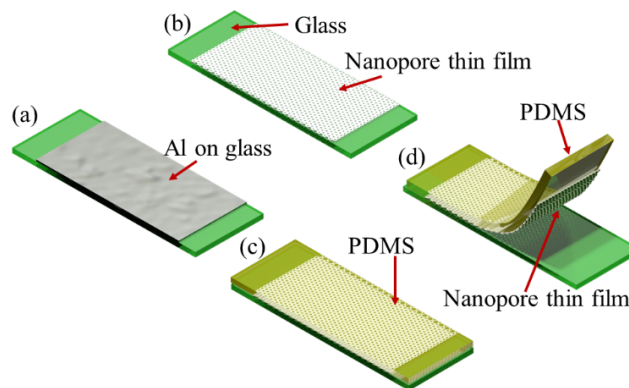


Fig. 4.3. Process flow to fabricate nanopore thin film on flexible substrate: FLEX-nanopore-TF.

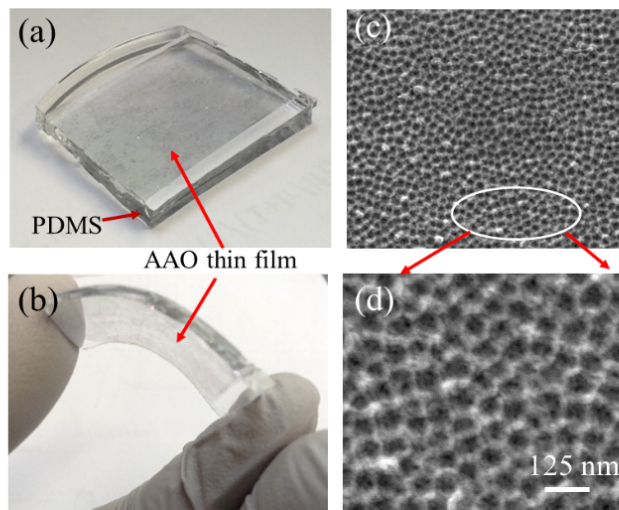


Fig. 4.4. Photo of (a) a FLEX-nanopore-TF; (b) a bended FLEX-nanopore-TF; (c-d) SEM images showing the nanopores of AAO thin film.

## Experimental Results and Discussion

### Fabrication of Flexible Nanopore Thin Film

The process flow for fabricating FLEX-nanopore-TF is illustrated in Fig. 4.3. Briefly, after a layer of Al with high purity is deposited on glass substrate, anodic aluminum oxide (AAO) nanopore thin film is fabricated from Al thin film on glass substrate using a two-step anodization process [11], then the AAO nanopore thin film is immersed in liquid PDMS, followed by 65 °C curing for 2 hrs. Thereafter, AAO nanopore thin film along with a layer of PDMS is peeled gently off the glass substrate, resulting in a FLEX-nanopore-TF. The photos of the fabricated FLEX-nanopore-TF and a SEM image of the nanopores in the thin film are given in Fig. 4.4. Typical thickness of PDMS for this device is ~3 mm and the thickness of the nanopore thin film is ~3 μm.

The mechanical property and reliability of the FLEX-nanopore-TF has been evaluated. It has been found that no cracks are observed in the FLEX-nanopore-TF after cyclic bending (Fig. 4.4b), indicating its good flexibility.

### Pressure Sensing Using FLEX-nanopore-TF Device

Using the setup in Fig. 4.2a, the applied pressure on the FLEX-nanopore-TF device can be calculated by measuring the horizontal displacement of the two ends of the FLEX-nanopore-TF device, given the pressure is applied along its horizontal axis of the device (Fig. 4.5). Based on the bending curvature, the mechanical properties of PDMS (i.e., Young's modulus of 600 kPa [14], etc.) and the displacement of the both ends of the FLEX-nanopore-TF device, the applied pressure on the device can be calculated using the following formulas [15-16]:

$$E \equiv \frac{\sigma(\varepsilon)}{\varepsilon} = \frac{F/A}{\Delta L/L_0} = \frac{FL_0}{A\Delta L}$$

$$\Delta L = L_0 - d$$

$$p = \frac{F}{A} = E \left(1 - \frac{\sin \alpha}{\alpha}\right)$$

Where  $p$ ,  $F$  are the applied pressure and force on the two ends of the device, respectively.  $L_0$  is the original length,  $A$  is the cross-section area of the FLEX-nanopore-TF.  $E$  is the Young's modulus of PDMS.  $\alpha$  is the angle and  $d$  is the length shown in Fig.5a, respectively.

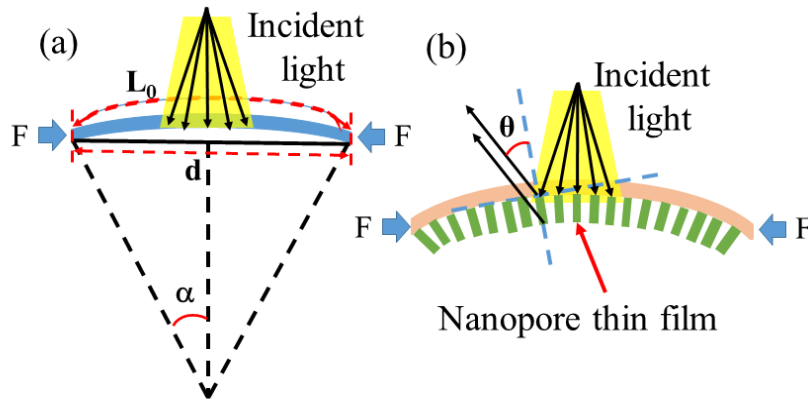


Fig. 4.5. Sketch showing (a) the bending of the FLEX-nanopore-TF before and after being applied with a compressive pressure; (b) close-up showing the bending of the FLEX-nanopore-TF.

As shown in Fig. 4.6a, the shift of the peak of the optical signal is clearly observed under different applied pressure on the device. Note that the optical responses of the FLEX-nanopore-TF device are monitored by an optical fiber-based optical spectrometer as shown in Fig. 4.2a. It has been found the peak has a blue-shift with increased compressive pressure. And its sensitivity of the FLEX-nanopore-TF based pressure sensor is  $\sim 0.01$  nm/mmHg. The simulated results match the experimental results quite well (Fig. 4.6b).

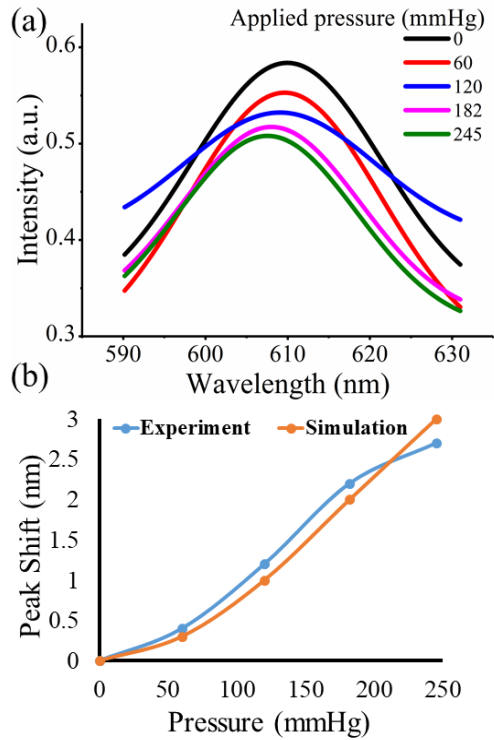


Fig. 4.6. (a) Measured optical signals from the device under different pressure; (b) measured shift of the peak of the reflected optical signal from the device and the simulated peak shift of the optical signal under different pressures.

## Drug Loading Process

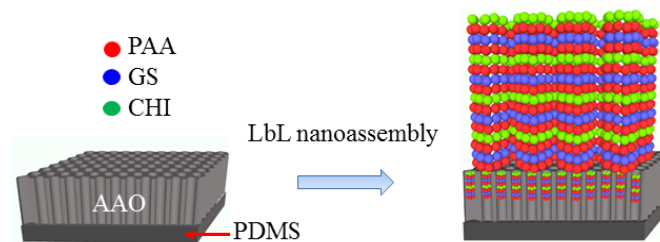


Fig. 4.7. Sketch: the drug loading to the nanopore thin film using layer-by-layer (LbL) nanoassembly process (not-to-scale).

In the experiments, the concentrations of PAA, GS, and CHI are prepared to be 2 mg/ml, 5 mg/ml, and 0.12 mg/ml, respectively, which are all diluted in PBS 6.5. First, the drug loading to the FLEX-nanopore-TF device has been carried out. Similar to our previous work [9-10], during

the drug loading process in Fig. 4.7, [PAA/GS/PAA/CHI] layer is repeatedly deposited ten times on the nanopore thin film using layer-by-layer (LbL) nanoassembly process [17]. And the loading process can be monitored optically by measuring the reflected signal from the device surface, similar to the setup in Fig. 4.2a.

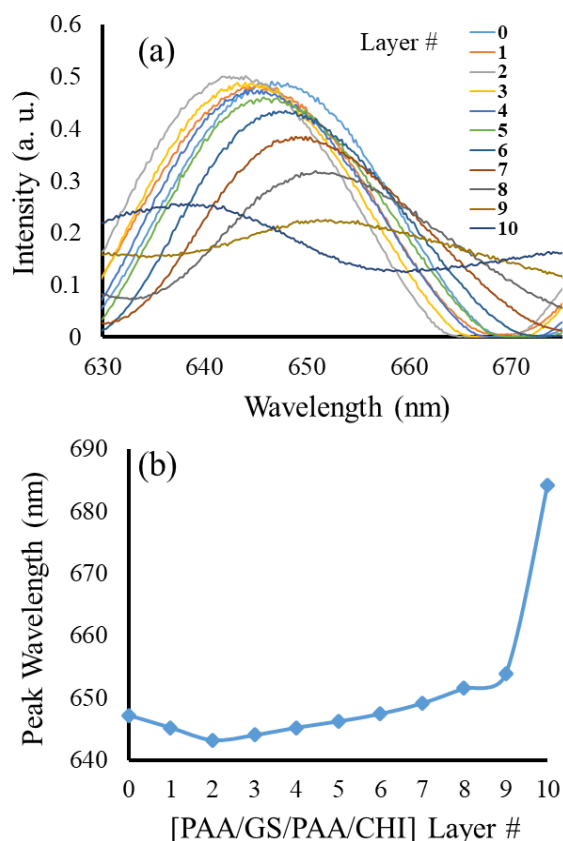


Fig. 4.8. (a) Measured interference optical signals after deposition of each layer [PAA/GS/PAA/CHI]; (b) Measured shift of the optical signal after disposition of each layer during the loading procedure.

The measured reflectance optical signal for each deposited [PAA/GS/PAA/CHI] layer is shown in Fig. 4.8. One of the peaks of optical signal from bare AAO nanopore thin film at wavelength of 647 nm is selected as the reference peak. After the first layer and second layer of [PAA/GS/PAA/CHI] deposition, the peak has blueshift to 643 nm. Starting from the third layer of deposition, the peak has a red shift, and eventually to ~684 nm after deposition of the tenth layer. The peak shifts are caused by the changes of effective optical thickness (EOT) of the AAO

nanopore thin film due to the deposition of the [PAA/GS/PAA/CHI] layers [18]. The shift of the interference fringes of the reflectance optical signal is caused by the changes of effective refractive index of nanopore thin film due to the coated layers, which is different from the reason of the changes of the incident angle of illuminating light for pressure sensing in Fig. 4.2 and Fig. 4.5.

### Drug Release Process

Drug release process is realized by flowing DI water through the devices in Fig. 4.9. The measured reflectance optical signals during the drug release procedure are shown in Fig. 10a. The shift of the peaks of the optical signals are clearly observed. As shown in Fig. 4.10b, for the first 2 minutes, the peak has a blueshift of  $\sim 1\text{nm}$ . This is because the deposited chemicals on AAO nanopore surface are dissolved, leading to drug release. Then the peak has a redshift, suggesting the chemicals/drug stored inside the nanopores start to be released into water. Peak shift has then been observed for next 120 minutes, 600 minutes and 1440 minutes. During this period of time, the peak has a redshift, suggesting the chemicals/drug stored inside the nanopores start to be released into the DI water [18]. The wavelength peak shift during the release process from 0 min to 1440 min is plotted in Fig. 4.10b. As shown in Fig. 4.10b, the optical signal shift at 1440 minutes does not tend to become saturated, indicating that some drugs are still not released.

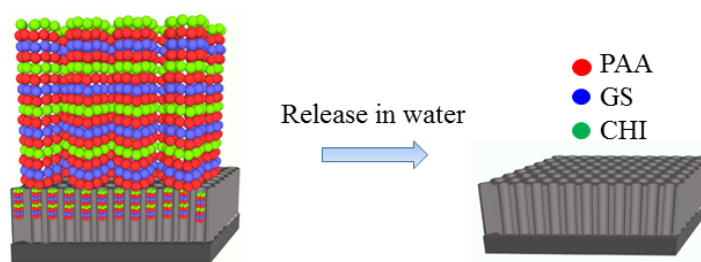


Fig. 4.9. Sketch: the drug release from the nanopore thin film in water (not-to-scale).

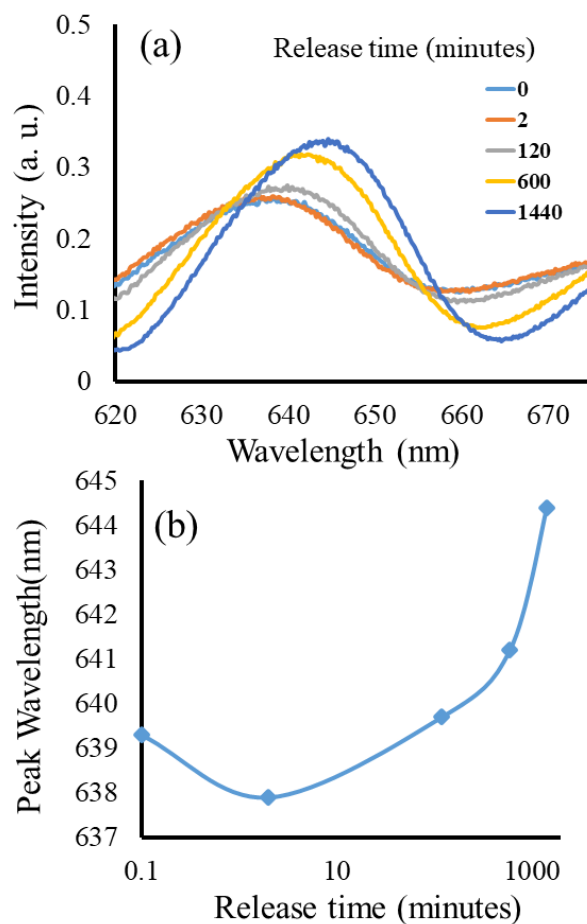


Fig. 4.10. (a) Measured interference optical signals at different release time; (b) Measured shift of the optical signal during the release procedure.

The drug release from the same FLEX-nanopore-TF device has been further monitored from first day up to 21 days. As shown in Fig. 4.11, it has been found the shift of the optical signal continues increase till 8 days, and the shift becomes smaller and eventually stops from 15 days, indicating the drugs have been totally released. It is anticipated the release time can further extended by increasing the size (diameter and depth) of the nanopores and the numbers of the [PAA/GS/PAA/CHI] layers so that more drugs are loaded to the device.

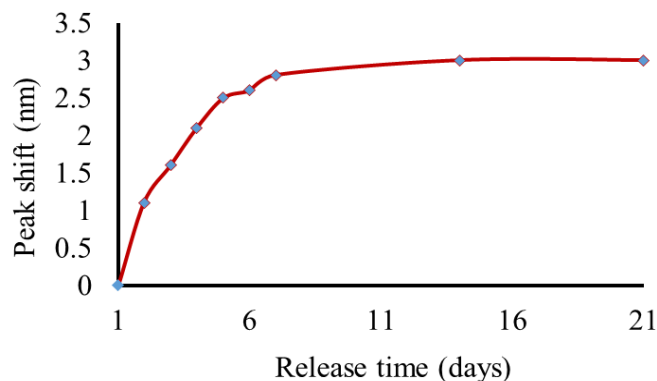


Fig. 4.11. Measured drug release from the device: the shift of the optical signal stops after 15-day release, indicating the drug has been totally released.

### Summary

A flexible nanopore thin film (FLEX-nanopore-TF) device for the controlled drug release and pressure sensing has been developed. The drug delivery device is realized by loading the drugs to the nanopore thin film and to the stacked nanoscale thin film using LbL nanoassembly process. It has been demonstrated up to 15 days drug release with the nanopore size of 50 nm and the LbL coating 10 layers of [PAA/GS/PAA/CHI] on the nanopore thin film. The release time can be further extended by increasing the nanopore size and density and the number of the [PAA/GS/PAA/CHI] layers. The pressure sensing is achieved due to the change of the incident angle of the illuminating light to the surface of the nanopore thin film when a pressure is applied on the FLEX-nanopore-TF device, resulting in the shift of the reflected optical signals from the device. It has been found its pressure sensitivity is  $\sim 0.01$  nm/mmHg. The multiple functions offered by the FLEX-nanopore-TF make it an ideal wearable device for drug delivery and pressure detection applications.

## References

- [1] J.H. Ahn, H.S. Kim, E. Menard, K.J. Lee, Z. Zhu, D.H. Kim, R.G. Nuzzo, et al. "Bendable integrated circuits on plastic substrates by use of printed ribbons of single-crystalline silicon." *Applied Physics Letters*, vol. 90, no. 21, pp. 213501, 2007.
- [2] L. Li, H. Lin, S. Qiao, Y. Zou, S. Danto, K. Richardson, J. David Musgraves, N. Lu, and J. Hu. "Integrated flexible chalcogenide glass photonic devices." *Nature Photonics*, vol. 8, no. 8, pp. 643-649, 2014.
- [3] D. Kang, B. Gai, B. Thompson, S. M. Lee, N. Malmstadt, and J. Yoon. "Flexible Opto-Fluidic Fluorescence Sensors Based on Heterogeneously Integrated Micro-VCSELs and Silicon Photodiodes." *ACS Photonics*, vol. 3, no. 6, pp. 912-918, 2016.
- [4] S.M. Won, H.S. Kim, N. Lu, D.G. Kim, C.D. Solar, T. Duenas, A. Ameen, and J. A. Rogers. "Piezoresistive strain sensors and multiplexed arrays using assemblies of single-crystalline silicon nanoribbons on plastic substrates." *IEEE Transactions on Electron Devices*, vol. 58, no. 11, pp. 4074-4078, 2011.
- [5] Ç. Varel, Y.-C. Shih, B.P. Otis, T.S. Shen, and K.F. Böhringer, "A wireless intraocular pressure monitoring device with a solder-filled microchannel antenna," *Journal of Micromechanics and Microengineering*, vol. 24, pp. 045012, 2014.
- [6] H.A. Quigley and A.T. Broman, "The number of people with glaucoma worldwide in 2010 and 2020," *British journal of ophthalmology*, vol. 90, pp. 262-267, 2006.
- [7] M.B. Brown, G.P. Martin, S.A. Jones, and F.K. Akomeah. "Dermal and transdermal drug delivery systems: current and future prospects." *Drug Delivery*, vol. 13, no. 3, pp. 175-187, 2006.
- [8] D. Son, J. Lee, S. Qiao, R. Ghaffari, J. Kim, J. E. Lee, C. Song et al. "Multifunctional wearable devices for diagnosis and therapy of movement disorders." *Nature Nanotechnology*, vol. 9, no. 5, pp. 397-404, 2014.
- [9] C. Song, X. Che, and L. Que, "Controlled drug loading and release enabled by nanopore thin film and layer-by-layer nanoassembly," in *Proc. IEEE Sensors Conference*, pp. 199-201, 2016.
- [10] C. Song, Chao, X. Che, and L. Que. "Nanopore thin film enabled optical platform for drug loading and release." *Optics express* 25, no. 16, pp. 19391-19397, 2017.
- [11] H. Yin, X. Li, and L. Que. "Fabrication and characterization of aluminum oxide thin film micropatterns on the glass substrate." *Microelectronic Engineering*, vol. 128, pp. 66-70, 2014.
- [12] M. Born, and E. Wolf, *Principal of Optics*, John Wiley & Sons, Inc., 2000.
- [13] RSoft™: <https://www.synopsys.com/optical-solutions/rsoft.html>
- [14] M. Liu, J. Sun, Y. Sun, C. Bock, and Q. Chen. "Thickness-dependent mechanical properties of polydimethylsiloxane membranes." *Journal of micromechanics and microengineering* 19, no. 3, pp. 035028, 2009.
- [15] L. Chu, L. Que, and Y. B. Gianchandani. "Measurements of material properties using differential capacitive strain sensors." *Journal of Microelectromechanical Systems*, vol. 11, no. 5, pp. 489-498, 2002.
- [16] Y. Gianchandani and K. Najafi. "Bent-beam strain sensors." *Journal of Microelectromechanical Systems* 5, no. 1, pp: 52-58, 1996.
- [17] W.C. Cheng, Y. He, A.Y. Chang, and L. Que. "A microfluidic chip for controlled release of drugs from microcapsules." *Biomicrofluidics*, vol. 7, no. 6, pp. 064102, 2013.
- [18] T. Zhang, Z. Gong, R. Giorno, and L. Que. "A nanostructured Fabry-Perot interferometer." *Optics Express*, vol. 18, no. 19, pp. 20282-20288, 2010.

## CHAPTER 5. HIGH-RESOLUTION, FLEXIBLE, AND TRANSPARENT NANOPORE THIN FILM SENSOR ENABLED BY CASCADED FABRY-PEROT EFFECT

Chao Song, Xiaoke Ding, and Long Que. *Optics Letters*, vol. 43, no. 13, pp. 3057-3060, 2018.

### Abstract

This Letter reports a method to significantly improve the optical resolution of the anodic aluminum oxide (AAO) nanopore thin film sensor based on multi-cavity Fabry-Perot interference. The newly designed sensor is fabricated by bonding a layer of transparent polymer thin film (pTF), which is polydimethylsiloxane (PDMS), to a transparent AAO thin film to form a flexible pTF-nanopore sensor. In comparison with the AAO nanopore thin film sensor, the pTF-nanopore sensor shows a much-improved quality (Q) factor and optical resolution. Typical thicknesses of a PDMS layer and an AAO layer of the pTF-nanopore sensor are 80  $\mu\text{m}$  and 2  $\mu\text{m}$ , respectively. The pTF-nanopore sensor used for angle detection shows a sensitivity of 0.4 nm/deg with a resolution of 0.2 deg. The pTF-nanopore sensor can also be used for temperature monitoring with a sensitivity of 0.2 nm/ $^{\circ}\text{C}$  and a resolution of 1 $^{\circ}\text{C}$ .

### Introduction

Anodic aluminum oxide (AAO) is one of the most prevalent nanomaterials used in biosensing, biomedical and energy storage applications [1-9]. AAO, a biocompatible and self-assembled nanostructure material, can be rapidly fabricated by an anodization process in a cost-effective manner. Taking advantages of the unique optical properties of arrayed nanopores, different types of sensors or devices such as refractive index sensor [1], gas sensor [2], colorimetric sensor [3], theophylline and plant hormone sensor [4-5], cancer biomarker sensor [6], solar energy device [7], fluorescence enhancement sensor [8] and drug storage and release device [9,10] have been developed. While the AAO thin film based optical sensor (Fig. 5.1a) can offer limit of detection

(LOD) of biochemical such as disease biomarkers at a concentration in the picomolar or femtomolar range [6], further improvement of its LOD and optical resolution is still a very important topic. Some work has been done to optimize the LOD by tailoring the nanopore diameter, thickness and periodicity [11]. However, this method is complicated since it requires to tune the fabrication process parameters such as acid species and their concentrations, reaction temperature and the applied anodization voltage. Recently, it has been reported that the LOD of optical fiber-based sensor can be improved by utilizing cascaded Fabry-Perot cavities [12–18], which might be adopted to the AAO nanopore thin film based optical sensor to improve its LOD and resolution.

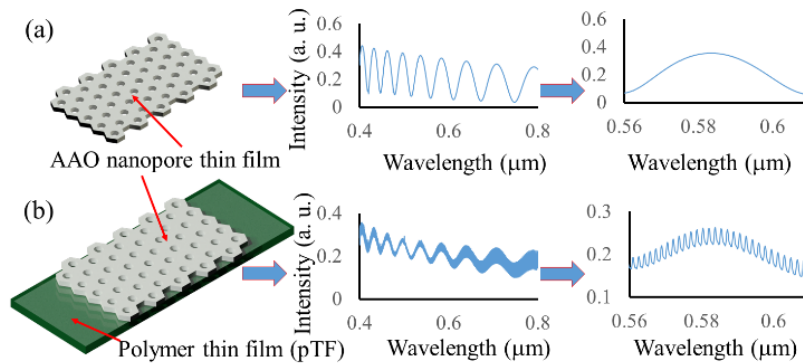


Fig. 5.1. (a) Sketches of an AAO nanopore thin film based optical sensor and its typical reflected interference signal, (b) sketches of the proposed pTF-nanopore sensor and its typical reflected interference signal.

In this letter, a method of improving the LOD of the AAO thin film based optical sensor is proposed by simply attaching a layer of transparent polymer thin film (pTF) to the AAO nanopore thin film. In this case, two Fabry-Perot cavities, the nanopore thin film and the pTF, are cascaded, resulting in a new type of optical sensor (pTF-nanopore sensor) as shown in Fig. 5.1b. The pTF layer is made from the transparent polymer polydimethylsiloxane (PDMS). The reflected optical signal (interference fringes) in Fig. 1a from the AAO nanopore thin film alone has a Full-Width-Half-Maximum (FWHM), typically in the range of 20-30 nm and its quality (Q) factor is  $\sim 20$  at 600nm for 2  $\mu\text{m}$  thick AAO nanopore thin film. In contrast, for the pTF, due to its increased

thickness (from 40  $\mu\text{m}$  to 100  $\mu\text{m}$ ), the reflected optical signal (interference fringes) has small FWHM, typically in the range of 0.4-1.4 nm and its Q factor is 400-1,500. When pTF and AAO nanopore thin film is cascaded as a pTF-nanopore sensor, the reflected optical signal in Fig. 5.1b is the convolution of the optical signals from the AAO nanopore thin film and the optical signal from pTF, resulting in a significantly increased number of sub-interference fringes in the same free spectral range (e.g., sub-interference fringes from 0.56  $\mu\text{m}$  to 0.61  $\mu\text{m}$  in Fig. 5.1b), thereby improving optical resolution compared to AAO nanopore thin film-based sensor [18-21].

### **Fabrication of pTF-nanopore Sensors**

The fabrication process flow is illustrated in Fig. 5.2a. Briefly, a cover glass is cleaned with acetone and isopropyl alcohol (IPA), followed by deposition of a thin layer of highly purified Al using E-beam evaporation. Typical thickness of Al thin film is  $\sim 1.5 \mu\text{m}$ . After electrochemical reaction in 0.3 M oxalic acid at 5.8  $^{\circ}\text{C}$  with a 30 V DC voltage using a two-step anodization process, Al thin film is transformed into AAO nanopore thin film [9]. Liquid PDMS is spin-coated on top surface of the AAO nanopore thin film, followed by being baked at 70 $^{\circ}\text{C}$  for 2 hours. Then the PDMS thin film (pTF) along with the AAO thin film is gently peeled off from the glass substrate, resulting in a flexible transparent pTF-nanopore sensor. Photos of the fabricated sensors are shown in Fig. 5.2b and Fig. 5.2c. The scanning electron microscope (SEM) image of AAO thin film is shown in Fig. 5.2d. The nanopore size is  $\sim 30\text{nm}$ .

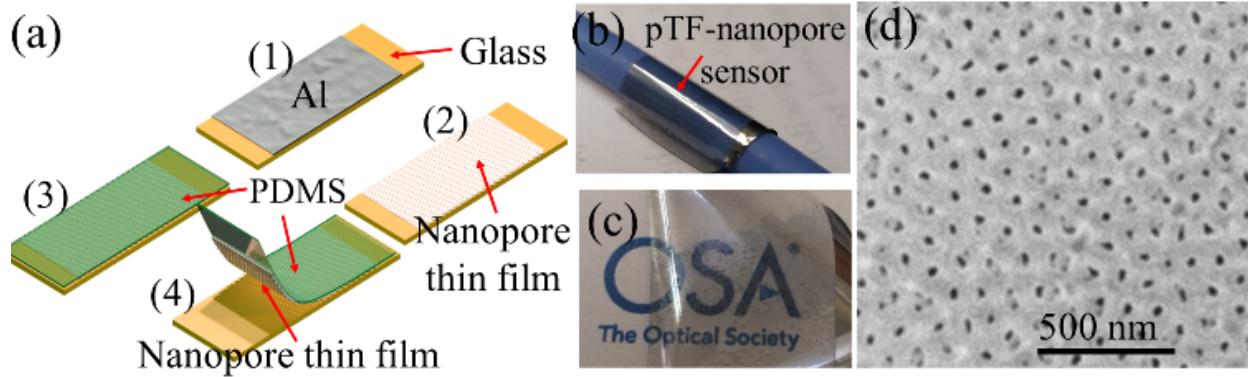


Fig. 5.2. (a) Process flow for fabricating pTF-nanopore sensors, (b) a pen is wrapped by the flexible pTF-nanopore sensor, (c) Text “OSA” can be clearly seen underneath the flexible transparent pTF-nanopore sensor, (d) SEM image of AAO nanopore thin film.

### Operational Principle of the pTF-nanopore Sensor

The experiment setup is schematically shown in Fig. 5.3a-b. A broadband white light source (Ocean Optics) is used as incident light. An optical fiber probe (Ocean Optics) is used to deliver the illuminating light to the pTF-nanopore sensor, and also collect the reflected signal from the sensor, which leads to a spectrometer (Ocean USB 4000) with a resolution of 0.22nm. As shown in Fig. 5.3c, the illumination light on a pTF-nanopore sensor will be reflected by three interfaces: Air/nanopore, nanopore/PDMS, PDMS/Air. The refractive index of each layer in the pTF-nanopore sensor is summarized as the following: air to be  $n_1=1$ , AAO to be  $n_2=1.67$ , PDMS to be  $n_3=1.4$  [18-19]. The thickness  $d_2$  of PDMS thin film is in the range of 40  $\mu\text{m}$ -100  $\mu\text{m}$ , and the thickness  $d_3$  of AAO nanopore thin film is  $\sim 2 \mu\text{m}$ . The resolution of the pTF-nanopore sensor is determined by the quality (Q) factor, which is defined by [21]:  $Q = \frac{\lambda}{\Delta\lambda}$ , where  $\lambda$  is the peak wavelength of the interference fringe and  $\Delta\lambda$  is its FWHM. The increased Q factor indicates the higher resolution of the pTF-nanopore sensor. Numerical simulation has been performed by Rigorous Coupled Wave Analysis (RCWA) method. In the calculations, the nanopore size and

distribution in Fig. 5.2d have been used directly to set up the model [22-23]. The thickness of pTF is set to be  $50\ \mu\text{m}$ , the AAO thickness is set to be  $2\ \mu\text{m}$  with average nanopore size of  $30\ \text{nm}$ . The interference pattern of  $50\ \mu\text{m}$  pTF alone, and the interference pattern of  $2\ \mu\text{m}$  AAO nanopore thin film alone are plotted in Fig. 5.3d. The interference pattern of a pTF-nanopore sensor is also plotted. As shown, the Q factor of the AAO nanopore thin film alone at  $618\ \text{nm}$  is  $\sim 20.5$ . The Q factor of the pTF-nanopore sensor at  $618\ \text{nm}$  becomes  $\sim 439.8$ , the same as that of pTF alone, which has been improved more than 20 folds, indicating the LOD of the pTF-nanopore sensors has been much improved in comparison with AAO nanopore thin film sensors.

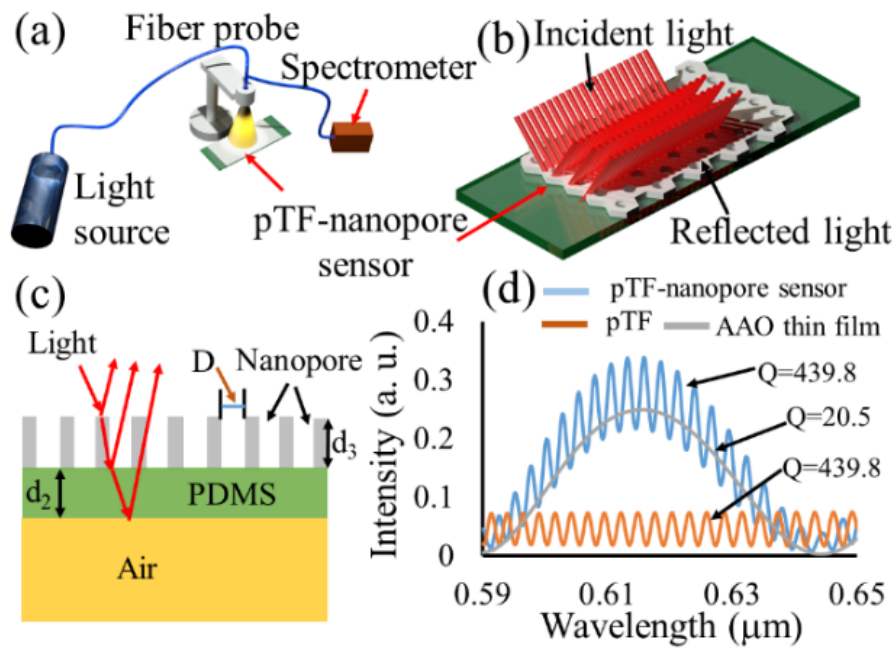


Fig. 5.3. (a) Experimental setup for the pTF-nanopore sensor, (b) close up of a pTF-nanopore sensor with incident light and the reflected light, (c) optical paths in the sensor, (d) the reflected interference patterns from a pTF with a thickness of  $50\ \mu\text{m}$  thin film, from a AAO nanopore thin film with a thickness of  $2\ \mu\text{m}$ , and from a pTF-nanopore sensor by cascading  $50\ \mu\text{m}$  pTF and  $2\ \mu\text{m}$  AAO nanopore thin film, respectively. The resolution of the spectrometer is assumed to be  $0.22\ \text{nm}$ .

### Thick pTF Effect in a pTF-nanopore Sensor

As shown in Fig. 5.3, the thickness of the pTF in a pTF-nanopore sensor determines the Q factor and hence the resolution of the sensor. Meanwhile, in order to measure the transducing signal from

a pTF-nanopore sensor, the resolution of the spectrometer should be at the same level of the sensor. Otherwise, the signal from the sensor cannot be resolved. Note that the resolution of the spectrometer (Ocean USB 4000) is 0.22 nm in the spectrum from 350 nm to 1100 nm. In the following, the transducing signals from pTF-nanopore sensors with a large thickness (3000  $\mu\text{m}$  as an example) of pTF layer is analyzed.

A pTF-nanopore sensor with pTF layer thickness of 3000  $\mu\text{m}$  has been fabricated. The measured transducing signal by the spectrometer is shown in Fig. 5.4a. As shown, no interference pattern due to the pTF layer superposed on the interference pattern of AAO nanopore thin film is observed. Clearly the spectrometer cannot resolve the interference patterns contributed by the pTF layer, which is much smaller than its resolution (0.22 nm). In order to make the interference patterns visible, the resolution of the spectrometer needs to be lowered down.

To verify the assumption, a series of imaginary “spectrometers” with different resolutions is used to numerically analyze the interference patterns from the fabricated sensor, in which the pTF thickness is 3000  $\mu\text{m}$  and the AAO thickness is 2  $\mu\text{m}$ . Fig. 5.4b-d show the calculated results of the pTF-nanopore sensor, assuming the spectrometer has a resolution of 0.01 nm, 0.04 nm and 0.2 nm in a spectral range from 590 nm to 630 nm (only from 590 nm to 594 nm shown for clarity), respectively. As shown in Fig. 4b, if the resolution is set to be 0.01 nm, even though there are massive interference peaks in the spectral range, they can be resolved. If the resolution is set to be 0.04 nm, then each data point will be the average of every four adjacent data points from Fig. 5.4b, leading to Fig. 4c. It is clearly observed in Fig. 5.4c that the number of the interference peaks has been reduced significantly in the same spectral range with much lower contrast. Furthermore, if the resolution is set to be 0.2 nm, each data point will be the average of every twenty adjacent data points from Fig. 5.4b, leading to Fig. 5.4d. As shown in Fig. 5.4d, the interference peaks resulting

from 3000  $\mu\text{m}$  pTF becomes very sparse and are almost gone, and even though the interference peak from AAO nanopore thin film is remained, very similar to the experimental results in Fig. 5.4a measured by the spectrometer with a resolution of 0.22 nm. Hence, the resolution of the spectrometer should be considered as a limiting factor when a pTF-nanopore sensor is under design.

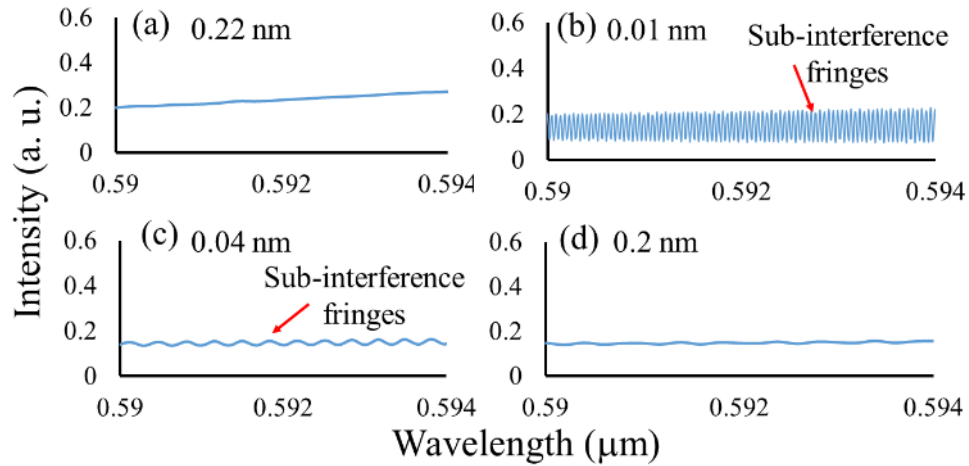


Fig. 5.4. (a) Measured optical signal from a pTF-nanopore sensor with a thickness of the pTF of 3000  $\mu\text{m}$  and a thickness of nanopore thin film of 2  $\mu\text{m}$  by a spectrometer with a resolution of 0.22 nm, (b)-(d) the calculated spectrum when the resolution is set up to be 0.01 nm, 0.04 nm and 0.2 nm, respectively.

### Thin pTF Effect in a pTF-nanopore Sensor

The effect of the thicknesses of pTF in the range of 0  $\mu\text{m}$  to 80  $\mu\text{m}$  on the formation of sub-interference fringes is also studied for a spectrometer with a resolution of 0.22 nm. The reflection spectrum from pTF-nanopore sensors with the pTF thickness ranging from 0  $\mu\text{m}$  to 80  $\mu\text{m}$  but with the same AAO nanopore thin film thickness of 2  $\mu\text{m}$  is shown in Fig. 5.5a. The Q factor increases with the increased pTF thickness, indicating the resolution of the pTF-nanopore sensor can be improved by increasing pTF thickness. Given a spectrometer with a resolution of 0.22 nm, the FWHM can be as low as  $\sim 0.4$  nm and Q factor can be as high as 1,544 at the wavelength of 618 nm. Under this condition, the Q factor reaches 1,544 when the pTF thickness reaches 80  $\mu\text{m}$ . And further increasing pTF thickness will not lead to an increase of resolution anymore. The reflection

spectrum from pTF-nanopore sensors with the pTF thickness changing from 0  $\mu\text{m}$ , 40  $\mu\text{m}$ , 60  $\mu\text{m}$ , and 80  $\mu\text{m}$  has been experimentally examined, shown in Fig. 5.5b. It has been found that no sub-interference fringes superposed on the interference pattern from AAO nanopore thin film when the pTF thickness is 0  $\mu\text{m}$ . As the pTF thickness increases from 40  $\mu\text{m}$  to 80  $\mu\text{m}$ , there are 10, 16 and 20 sub-interference fringes superposed on the interference pattern from AAO nanopore thin film in the wavelength range of 590 nm to 630 nm. As a result, the Q factor of the pTF-nanopore sensors increase. The studies of the thickness of pTF effect on the pTF-nanopore sensors provides a critical guideline to design this type of sensors if the resolution of the spectrometer is given.

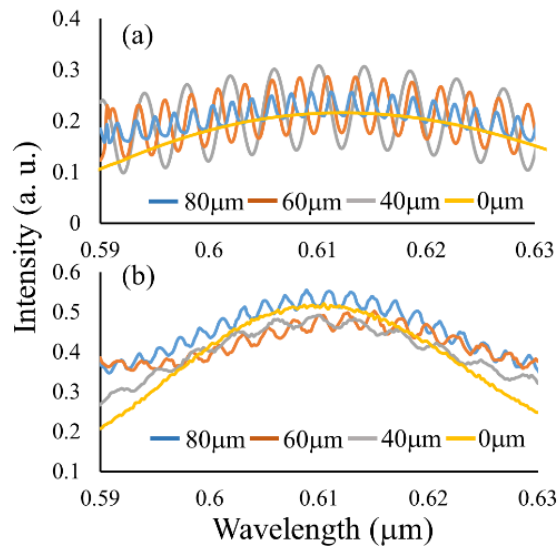


Fig. 5.5. (a) The calculated spectrum of the pTF-nanopore sensors with the pTF of different thicknesses from 0  $\mu\text{m}$  to 80  $\mu\text{m}$ , the thickness of AAO nanopore thin film is fixed at 2  $\mu\text{m}$ , (b) the measured spectrum of the pTF-nanopore sensors with the pTF of thicknesses from 0  $\mu\text{m}$  to 80  $\mu\text{m}$  using a spectrometer with a resolution 0.22 nm.

### Angle Sensing

The angle change can be monitored by the pTF-nanopore sensor. In the experiments, the sensor is positioned onto an optical rotation stage (Edmund Optics) which can change the angle with a step precision of 0.01 degree. Two types of sensors are tested. One sensor (SENSOR1) is the AAO nanopore thin film fabricated on a glass cover slip. The other (SENSOR2) is a pTF-nanopore

sensor and the pTF thickness is  $80\ \mu\text{m}$ . For both sensors, the thickness of AAO nanopore thin film is  $2\ \mu\text{m}$ . Simulation and experimental results for both sensors are shown in Fig. 5.6.

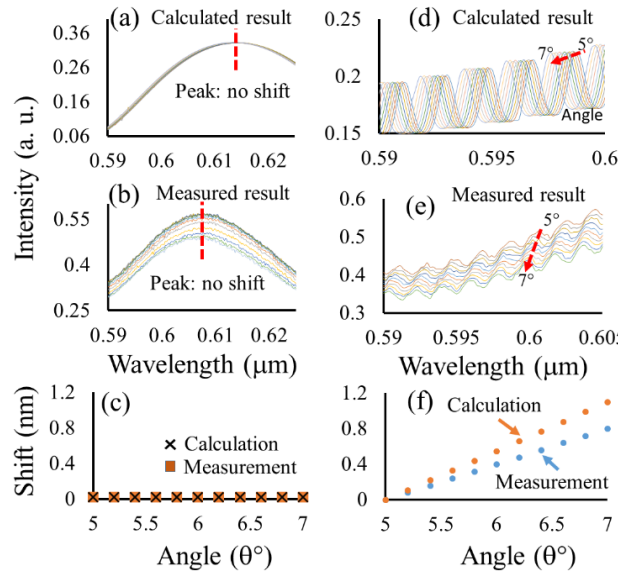


Fig. 5.6. SENSOR1: (a) Calculated spectrum, (b) measured spectrum, and (c) calculated and measured peak shift of the fringes with the angle change. SENSOR 2: (d) Calculated spectrum, (e) measured spectrum, and (f) calculated and measured peak shift of the fringes with the angle change.

As shown in Fig. 5.6a-c for SENSOR1, no sub-interference fringes are superposed on one interference fringe (wavelength spans from  $0.59\ \mu\text{m}$  to  $6.3\ \mu\text{m}$ ) from the AAO nanopore thin film. And no distinguishable peak shift is observed for every  $0.2$  degree angle change from  $5$  to  $7$  degrees. This indicates SENSOR1 is unsuitable for monitoring angle change. In contrast, for SENSOR2, there are 5 sub-interference fringes superposed on one interference fringe (wavelength spans from  $0.59\ \mu\text{m}$  to  $0.6\ \mu\text{m}$ ) from the AAO nanopore thin film. The shift of the peaks of interference fringes can be clearly observed when the angle is changed from  $5$  to  $7$  degrees as shown in Fig. 5.6d-f, resulting from the change of optical path difference from various interfaces (Fig. 5.3c). The angle sensitivity of SENSOR2 is  $\sim 0.4\ \text{nm/degree}$ .

## Temperature Sensing

Two types of pTF-nanopore sensors have been fabricated to detection the temperature change. The thicknesses of nanopore thin film for both SENSOR3 and SENSOR4 are the same of 2  $\mu\text{m}$ . The thicknesses of pTF in SENSOR3 and SENSOR4 are 1.4 mm and 80  $\mu\text{m}$ , respectively. The sensors are placed onto a hotplate and temperature is increased from 25  $^{\circ}\text{C}$  degree to 30  $^{\circ}\text{C}$  with a step of 1  $^{\circ}\text{C}$ .

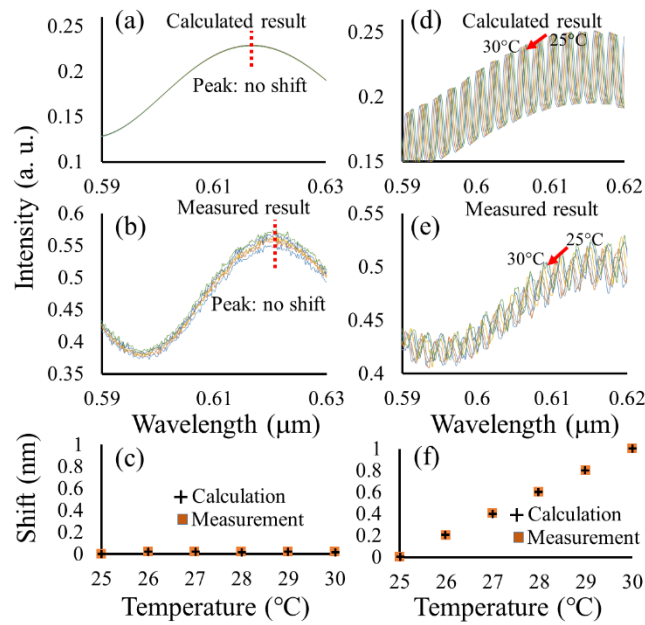


Fig. 5.7. SENSOR3: (a) Calculated spectrum, (b) measured spectrum, and (c) calculated and measured peak shift of the fringes with the temperature change. SENSOR 4: (d) Calculated spectrum, (e) measured spectrum, and (f) calculated and measured peak shift of the fringes with the temperature change.

As shown in Fig. 5.7a-c for SENSOR3, no sub-interference fringes are superposed on one interference fringe (wavelength spans from 0.59  $\mu\text{m}$  to 6.3  $\mu\text{m}$ ) from the AAO nanopore thin film. And no distinguishable peak shift is observed when the temperature changes from 25  $^{\circ}\text{C}$  to 30  $^{\circ}\text{C}$ . This indicates that SENSOR3 is unsuitable for monitoring temperature change. In contrast, for SENSOR4, there are 15 sub-interference fringes superposed on one interference fringe

(wavelength spans from 0.59  $\mu\text{m}$  to 0.62  $\mu\text{m}$ ) from the AAO nanopore thin film. The PDMS has a thermal optical coefficient of  $-4.5 \times 10^{-4}/^{\circ}\text{C}$  [20], hence the temperature change leads to a change of refractive index of PDMS. The shift of the peaks of interference fringes can be clearly observed when the temperature changes as shown in Fig. 5.7d-f, resulting from the change of optical path difference from various interfaces (Fig. 5.3c). The temperature sensitivity of SENSOR4 is 0.2 nm/ $^{\circ}\text{C}$ .

### Summary

A new flexible and transparent pTF-nanopore sensor has been developed based on the multi-cavity Fabry-Perot interference effect. Typical thicknesses of the pTF and nanopore layer in a pTF-nanopore sensor are 80  $\mu\text{m}$  and 2  $\mu\text{m}$ , respectively. The pTF-nanopore sensor has been used for angle measurement and temperature sensing, offering significantly improved optical resolution in comparison with AAO nanopore thin film sensors. Given its high resolution, transparency and flexibility, this type of sensor can be potentially used as a wearable sensor to monitor disease biomarkers at a much lower concentration than that by using the AAO nanopore thin film sensors previously. In addition, this type of sensor can be potentially fabricated as a smart contact lens suitable for monitoring the intraocular pressure in real time, critical for glaucoma diagnosis and treatment.

### References

- [1] S.H. Gong, A. Stolz, G.H. Myeong, E. Dogheche, A. Gokarna, S.W. Ryu, D. Decoster, and Y.H. Cho, "Effect of varying pore size of AAO films on refractive index and birefringence measured by prism coupling technique," *Optics Letters*, vol. 36, pp. 4272, 2011.
- [2] F. Rumiche, H. H. Wang, W. S. Hu, J. E. Indacochea, and M. L. Wang, "Anodized aluminum oxide (AAO) nanowell sensors for hydrogen detection," *Sensors and Actuators, B: Chemical*, vol. 134, pp. 869, 2008.
- [3] Y. Liu, H. H. Wang, J. E. Indacochea, and M. L. Wang, "A colorimetric sensor based on anodized aluminum oxide (AAO) substrate for the detection of nitroaromatics," *Sensors and Actuators, B: Chemical*, vol. 160, pp. 1149, 2011.
- [4] C. Song, C. Chen, X. Che, W. Wang, and L. Que, "Detection of plant hormone abscisic acid (ABA)

- using an optical aptamer-based sensor with a microfluidics capillary interface," *Proceedings of the IEEE International Conference on Micro Electro Mechanical Systems (MEMS)*, pp. 370–373, 2017.
- [5] S. Feng, C. Chen, W. Wang, and L. Que, "An aptamer nanopore-enabled microsensors for detection of theophylline," *Biosensors and Bioelectronics*, vol. 105, pp. 36, 2018.
- [6] T. Zhang, Y. He, J. Wei, and L. Que, "Nanostructured optical microchips for cancer biomarker detection," *Biosensors and Bioelectronics*, vol. 38, pp. 382, 2012.
- [7] T. Yang, X. Wang, W. Liu, Y. Shi, and F. Yang, "Double-layer anti-reflection coating containing a nanoporous anodic aluminum oxide layer for GaAs solar cells," *Optics Express*, vol. 21, pp. 18207, 2013.
- [8] X. Li, Y. He, T. Zhang, and L. Que, "Aluminum oxide nanostructure-based substrates for fluorescence enhancement," *Optics Express*, vol. 20, pp. 21272, 2012.
- [9] C. Song, X. Che, and L. Que, "Nanopore thin film enabled optical platform for drug loading and release," *Optics Express*, vol. 25, pp. 19391, 2017.
- [10] H.J. Kang, D. J. Kim, S.J. Park, J.B. Yoo, and Y. S. Ryu, "Controlled drug release using nanoporous anodic aluminum oxide on stent," *Thin Solid Films*, vol. 515, pp. 5184, 2007.
- [11] W. Lee and S. Park, "Porous Anodic Aluminum Oxide: Anodization and Templated Synthesis of Functional Nanostructures," *Chemical reviews*, vol. 114, no. 15, pp. 7487, 2014.
- [12] G. Liu, Q. Sheng, W. Hou, and M. Han, "High-resolution, large dynamic range fiber-optic thermometer with cascaded Fabry–Perot cavities," *Optics Letters*, vol. 41, pp. 5134, 2016.
- [13] H. Y. Choi, G. Mudhana, K. S. Park, U.C. Paek, and B. H. Lee, "Cross-talk free and ultra-compact fiber optic sensor for simultaneous measurement of temperature and refractive index," *Optics Express*, vol. 18, pp. 141, 2010.
- [14] H. Y. Choi, K. S. Park, S. J. Park, U. C. Paek, B. H. Lee, and E. S. Choi, "Miniature fiber-optic high temperature sensor based on a hybrid structured Fabry–Perot interferometer," *Optics Letters*, vol. 33, pp. 2455, 2008.
- [15] Z. L. Ran, Y. J. Rao, W. J. Liu, X. Liao, and K. S. Chiang, "Laser-micromachined Fabry-Perot optical fiber tip sensor for high-resolution temperature-independent measurement of refractive index," *Optics Express*, vol. 16, pp. 2252, 2008.
- [16] Y. Zhang, X. Chen, Y. Wang, K. L. Cooper, and A. Wang, "Microgap multicavity Fabry-Pérot biosensor," *Journal of Lightwave Technology*, vol. 25, pp. 1797, 2007.
- [17] P. Wierzba, Proc. *SPIE 9816*, 98160V(2015)
- [18] P. Chen, X. Shu, H. Cao, and K. Sugden, "Ultra-sensitive refractive index sensor based on an extremely simple femtosecond-laser-induced structure," *Optics Letters*, vol. 42, pp. 3145, 2017.
- [19] R. Boidin, T. Halenkovič, V. Nazabal, L. Beneš, and P. Němec, "Pulsed laser deposited alumina thin films," *Ceramics International*, vol. 42, no. 1, pp. 1177, 2016.
- [20] Q. Wang, C. Du, J. Zhang, R. Lv, and Y. Zhao, "Sensitivity-enhanced temperature sensor based on PDMS-coated long period fiber grating," *Optics Communications*, vol. 377, pp. 89, 2016.
- [21] B. Hausmann, I. Bulu, P. Deotare, M. McCutcheon, V. Venkataraman, M. L. Markham, D. Twitchen, and M. Loncar, "Integrated high-quality factor optical resonators in diamond," *Nano letters*, vol. 13, no. 5, pp. 1898, 2013.
- [22] A. Hierro-Rodriguez, I. Leite, P. Rocha-Rodrigues, P. Fernandes, J. Araujo, P. Jorge, J. L. Santos, J. M. Teixeira, and A. Guerreiro, "Hydrogen sensing via anomalous optical absorption of palladium-based metamaterials," *Nanotechnology*, vol. 27, pp. 185501, 2016.
- [23] A. Hierro-Rodriguez, P. Rocha-Rodrigues, F. Valdés-Bango, J. Alameda, P. Jorge, J. L. Santos, J. P. Araujo, J. M. Teixeira, and A. Guerreiro, "On the anodic aluminum oxide refractive index of nanoporous templates," *Journal of Physics D: Applied Physics*, vol. 48, pp. 455105, 2015.

## **CHAPTER 6. MULTIFUNCTIONAL SMART SOFT CONTACT LENS DEVICE ENABLED BY NANOPORE THIN FILM FOR GLAUCOMA DIAGNOSTICS AND IN SITU DRUG DELIVERY**

Chao Song, Gil Ben-Shlomo, and Long Que. *Journal of Microelectromechanical Systems* (published), 2019.

### **Abstract**

In this section, we report a new power-free multifunctional soft contact lens device that can measure IOP, achieve extended drug delivery in situ, and detect glaucoma biomarkers, all within the same device. Experiments demonstrate that the contact lens sensor can detect Interleukin 12p70, one possible biomarker for glaucoma, in a concentration as low as 2 pg/ml in artificial tears. The sustained drug release of the contact lens device can last up to 30 days. In ex vivo tests using cadaver pig eyes, the sensor detected IOP in a range of 10 to 50 mmHg with excellent repeatability.

### **Introduction**

Glaucoma, a retinal neurodegenerative disease and a leading cause of blindness worldwide, is expected to affect about 112 million people by 2040 [1, 2]. Elevated intraocular pressure (IOP) is a primary contributing factor to glaucoma and its evaluation is used for diagnosis of the disease and monitoring the response to therapy. To date, patients' IOP is monitored periodically at the ophthalmologist's office, as tonometry requires specialized, expensive equipment and a trained professional to operate. Significant fluctuation in IOP and its increase above the normal range can be missed for months, until the next scheduled appointment, which can lead to substantial and irreversible retinal damage, loss of visual field, and even blindness. Hence, continuous or real-time in-home monitoring of IOP in selected cases of patients with glaucoma is greatly needed. Recently,

the Triggerfish "smart" contact lens sensor for continuous monitoring of IOP has been introduced [3]. The IOP data is transmitted from the lens wirelessly to a small adhesive antenna placed on the face near the eye. The antenna then transmits the data to a portable recorder worn by the patient. However, the fabrication and operation of this and other reported IOP sensors are relatively complicated [4-9], and they require a power supply and some form of powered data transfer. Furthermore, they can measure IOP, but cannot deliver drugs in situ for the treatment of ocular diseases and/or detect their biomarkers in the tear film.

Application of topical anti-glaucoma medications is the first line of treatment for glaucoma and is crucial for prevention of retinal and optic nerve damage in glaucoma patients [10-12]. Nonetheless, topical ocular drug delivery is challenging due to the physiological and anatomical constraints of the eye, and it is difficult to obtain the therapeutic drug concentration at the required site of action. As a result, only <1% of topically administered ocular drugs reaching the aqueous humor and ciliary body (the desired target tissue for anti-glaucoma drugs). This has led clinicians to recommend frequent dosing, which increases the risk for side effects and contributing to noncompliance by patients. Despite the grave consequences of noncompliance (i.e. visual impairment and blindness), it is a common phenomenon among glaucoma patients. To address this issue, recently, the conventional contact lens and the contact lens with integrated microtubes have been used for in situ drug delivery [13-16]. Anti-glaucoma drugs delivered by contact lenses lead to greater bioavailability of the drug, requiring lower concentration and quantity of the drug compared to eye drops. As a result, less side effects were noted in eyes treated by a drug-loaded contact lens compared to eye drops. However, the drug released from the contact lenses only lasted a short period of time (from a few hours up to four days). In addition, the drug release is not controlled and peaks immediately after the application of the contact lens to the eye, and

significantly subsides thereafter [17]. Ideally, a contact lens device should allow extended drug delivery with controlled release and greater bioavailability, thereby increasing efficacy, decreasing adverse effects and improving compliance.

Current glaucoma screening techniques, including IOP measurement, have poor sensitivity and are ineffective for early diagnosis of primary glaucoma (PG) [18, 19]. Given these limited screening methods, there is a great need for new biomarkers of early PG. Among many possible biomarkers [20, 21], of a particular interest is the role of cytokines, which are involved in oxidative stress and inflammation [20, 22]. However, in order to measure, screen, and validate the biomarkers, tears have to be obtained from patients and then analyzed using a high-sensitivity enzyme-linked immunosorbent assay (ELISA) [21, 23-24]. Current methods for tear-biomarker analysis are expensive and require the collection of tears from the patient. Given the limited amount of tears, the procedure of tear-sampling may be challenging and inconvenient to the patient. In recent studies, a graphene-silver nanowire (AgNW) field effect sensor fabricated on a contact lens was used to measure glucose levels in tears [25, 26]. Similarly, utilizing a contact lens device for the screening and measurement of biomarkers in tears could be a simple and efficient approach.

Herein, we report a novel, power-free, multifunctional smart contact lens that can accomplish three challenging missions: potentially real-time repeated IOP monitoring, in situ extended drug delivery, and detection of biomarkers of ocular diseases in tears, all with one single device. To the best of our knowledge, currently no reported technology can achieve these goals using a single device. The unique features of the multifunctional contact lens are summarized as follows: all three functional components of the contact lens (i.e. IOP sensing, extended drug delivery, and ocular disease biomarker detection) are fabricated from the same optically transparent and bio-compatible material-anodic aluminum oxide (AAO) thin film [27-29]; hence, significantly simplifying the

fabrication process and reducing its cost. Moreover, the IOP monitoring and detection of biomarkers for ocular diseases in the tear film are passive, and do not require a power source for their operation. Signals from these sensors are read by a portable spectrometer [28] or a smartphone-based spectrometer, and thus can be easily transmitted to the clinician, even from remote areas.

### **Contact Lens Device Description**

The sketch of the contact lens is shown in Fig. 6.1a. There are three functions embedded in the silicone elastomer polydimethylsiloxane (PDMS)-based contact lens. The AAO thin film patterns can be arranged in the central region (CR) and surround the central region (SCR) of the contact lens. The AAO thin film patterns are used as IOP sensors, as sensors to detect the ocular-disease biomarkers, and used as drug containers for extended in situ drug delivery. Note that all three functions are enabled by the same AAO nanopore structures. Hence, the fabrication process of this device is significantly simpler and cheaper than other reported contact lens sensors. The contact lens was designed so that there is a central region of about 4 mm in diameter in front of the pupil with no AAO thin film (Fig. 6.1a). However, it is noteworthy that due to the high transparency of the AAO thin film, it can also be positioned in front of the pupil without causing any visual deficit. The operational principles of the three functions are illustrated in Fig. 6.1b-d. For the biomarker detection (Fig. 6.1b), a biomarker-specific antigen is placed on the AAO surface. Once present in the tear-film, the biomarker binds to the antibody. As a result, the optical signal reflected from the AAO thin film shifts and can be evaluated by a spectrometer [30-32]. For in situ drug delivery (Fig. 6.1c), the drug is loaded into the AAO nanopores; once the contact lens is placed onto the

eye, the drug releases to the tear film, then into the eye. For the IOP sensing (Fig. 6.1d), the AAO thin film changes its curvature as a function of IOP, resulting in optical signal shift [28].

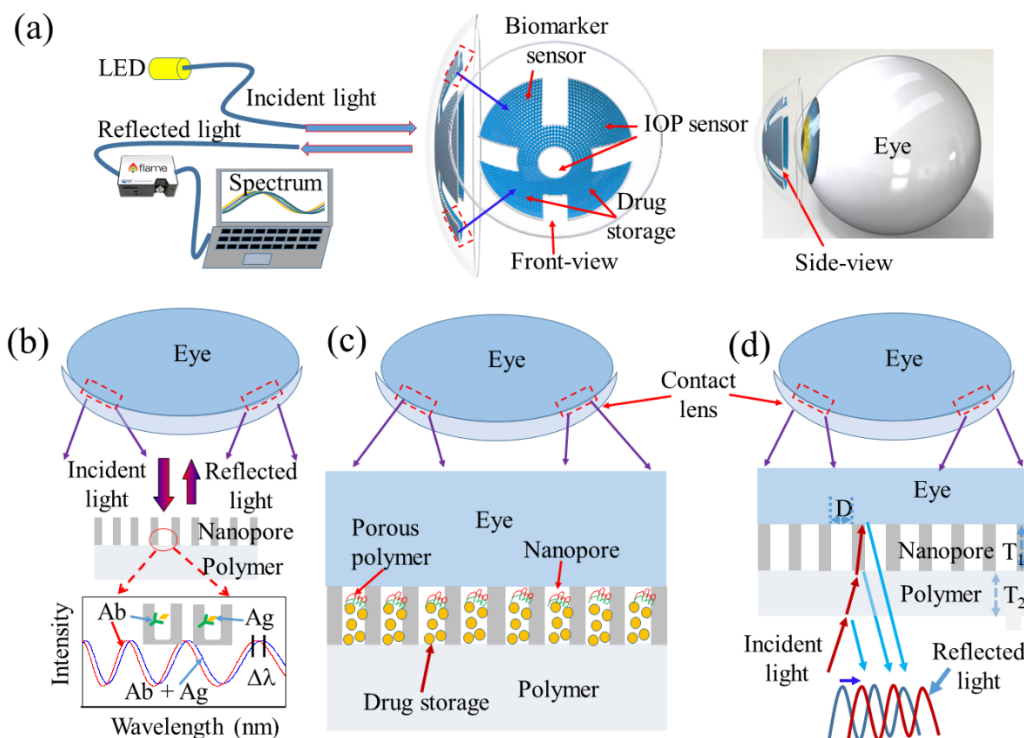


Fig. 6.1. (a) Schematic illustration of the smart contact lens: a layer of transparent bio-compatible nanopore thin film pattern integrated within the contact lens, used as pressure sensors for monitoring the intraocular pressure (IOP), for drug storage/delivery, and as biomarker detection sensors. (b) Close-up of the biomarker detection sensor: binding between the antibodies (Abs) and biomarker (antigens: Ags) causes the shift of the peaks of the optical signals. (c) Close-up of the drug storage and release: nanopores serve as nanocontainers to store the drug, and are covered by a thin layer of porous silicone that serves as a diffusion barrier for extended drug release. (d) Close-up of the IOP sensor: the peaks of reflected optical signal from contact lens device shift when the IOP changes.

## Material and Methods

### Chemicals and Materials

(1) For contact lens fabrication: PDMS and its cure agent were purchased from Dow Corning. The 3-D mold material for fabricating the AAO patterns is Methacrylic ester. (2) For biomarker detection: 11-Mercaptoundecanoic acid (HSC10COOH, 99%), 8-Mercapto-1-Octanol (HSC8OH,

98%), N-(3-Dimethylaminopropyl)-N'-ethylcarbodiimide hydrochloride (EDC), N-Hydroxysuccinimide (NHS), ethanolamine (EA), Phosphoric acid (PPA) and PBS buffer were purchased from Sigma-Aldrich (Milwaukee, WI) and used without further purification. Deionized (DI) water was obtained from a DI water purification system (Millipore, FRANCE). TheraTears® Artificial tears (Akron; IL, USA) were purchased from Walgreens. IL-12p was purchased from R & D Systems, Inc. (3) For drug release demonstration: fluorescein sodium salt (FSS) was purchased from Sigma, Inc. Timolol was purchased from SANDOZ, Inc.

### **Optical Measurement for Biomarker**

The detection setup of the nanopore-based sensors is the same as those previously reported [30]. Specifically, a broadband light source from a tungsten halogen lamp is coupled to a specifically-designed optical fiber probe (Ocean Optics, Inc., Dunedin, FL, USA), which illuminates the sensor surface perpendicularly. The reflected signals (transducing signals) were collected by the same optical fiber probe, leading to an optical spectrometer (Ocean Optics, Inc.), which can detect optical spectrum from 350 nm to 1050 nm.

### **Florescence Images and Analysis**

Fluorescent images were taken using a fluorescence microscope equipped with a mercury arc lamp source (Olympus, Inc.), which has the following filter sets: FITC (excitation filter: 475-490 nm; barrier filter: 500-540 nm); and TRITC (excitation filter: 545-565 nm; barrier filter: 580-620 nm). For FSS, the FITC filter set was used for fluorescence measurement. The excitation optical spectrum was from 475 nm to 490 nm. A MatLab program has been written to read the files of fluorescence images, which are then converted to gray scale images from the color images. A horizontal cutline was obtained through the fluorescence image and the corresponding intensity was obtained and then plotted.

## Results

### **Fabrication of Contact Lens and Characterization of Optical and Mechanical Properties**

The fabrication process can be divided into two parts: contact lens fabrication and AAO sensor fabrication. For the contact lens fabrication, the fabrication process flow is illustrated in Fig. 6.2a. Briefly, PDMS is prepared with a volume ratio of 9:1 to curing agent with thorough mixing and degassing for 2 hours. A chrome steel ball is then positioned on a hotplate which has been preheated to 100 °C. Then, the liquid PDMS is poured onto the ball. Due to its high viscosity, liquid PDMS slowly flows down along the surface of the ball and is cured in 3 minutes. After 3 minutes, a tube with a circular rim is firmly pressed against the ball to cut through the PDMS, and a contact lens with a circular boarder is obtained as shown in Fig. 6.2b. Using this fabrication process, the typical thickness of the contact lens is  $\sim 120$   $\mu\text{m}$ .

The fabrication process flow of the AAO sensors is illustrated in Fig. 6.2c-e. A covered glass slide is cleaned with Acetone, IPA and DI water, and dehydrated with nitrogen gas in sequence. Then, highly purified (99.99%) aluminum is deposited onto the cover glass slide with an E-beam evaporator. Al thin film is converted into AAO thin film by a two-step anodization process by immersing it in 0.3M oxalic acid at 5.8 °C for 3 hours [33]. Typical AAO thin film thickness is  $\sim 2$   $\mu\text{m}$ . Liquid PDMS with volume ratio 15:1 to curing agent is then spin-coated onto the AAO thin film at a spinning rate of 3000 rpm for 30 seconds. The PDMS/AAO/glass substrate is then baked at 65 °C for 3 hours to complete the PDMS curing process. Typical PDMS thickness is  $\sim 30$   $\mu\text{m}$ . Then, PDMS/AAO thin film is gently peeled off the glass substrate. Due to the barrier layer underneath the AAO thin film [34], the nanopores on the peeled PDMS/AAO thin film are not totally opened (e.g. they are covered by the barrier layer formed in the anodization process) [35].

In order to remove the barrier layer, AAO etchant is applied on the AAO thin film for 30 min, followed by a rigorous rinse by flowing DI water. This way, the nanopores in the AAO thin film are totally opened. A mold fabricated by 3D printing (Fig. 2d) is utilized to cut the PDMS/AAO thin film into desired patterns (Fig. 6.2e). Then the patterned PDMS/AAO thin film is bonded to the PDMS contact lens to form the new contact lens device as shown in Fig. 6.2f-g. Photos of a fabricated PDMS contact lens device is shown in Fig. 6.2h-i. A SEM image showing the nanopore in the AAO thin film is given in Fig. 6.2j.

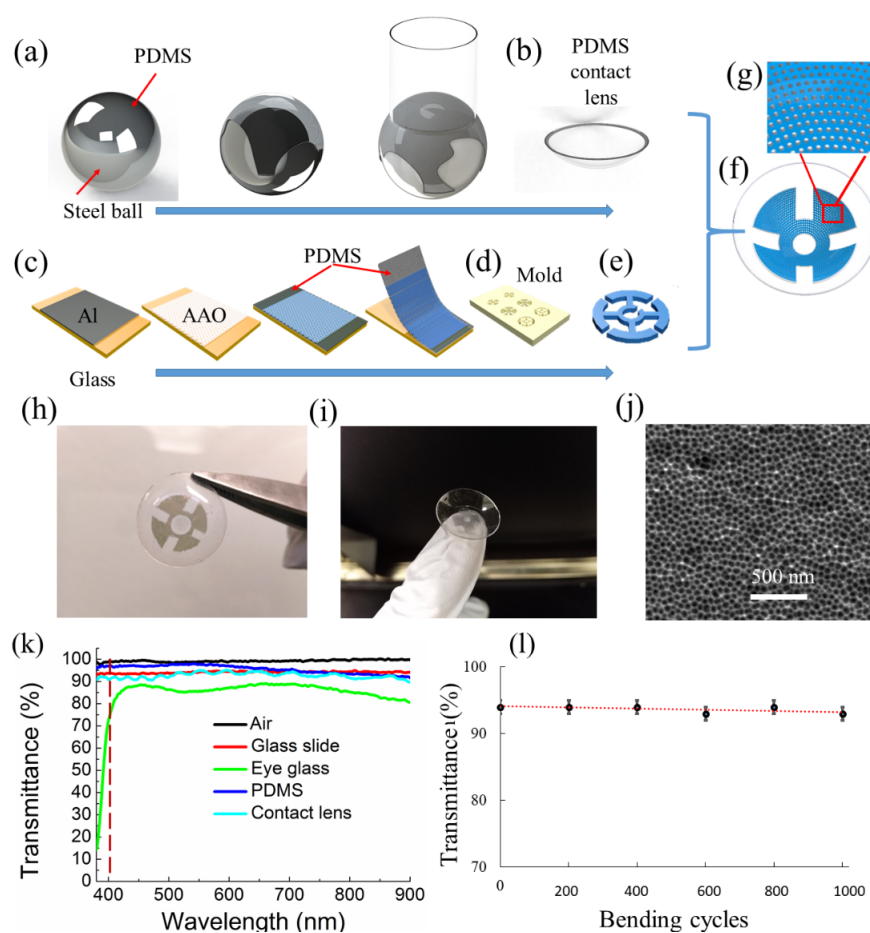


Fig. 6.2. (a-b) Process flow to fabricate the contact lens; (c-e) process flow to fabricate the patterned AAO nanopore thin film sensors; (f-g) sketch of the smart contact lens device; (h) photo of a fabricated smart contact lens device. In this design, the AAO thin film in the pupil region of the contact lens are made highly transparent compared to AAO thin film around the pupil region; (i) photo of a fabricated smart contact lens device. In this design, there is no AAO thin film in the pupil region; (j) SEM images of the AAO thin film of the sensors on contact lens; (k) Measured transmittance for contact lens device and other materials; (l) measured transmittance of contact lens device after being bent/stretched up to 1,000 cycles.

The optical transparency of the fabricated contact lens is evaluated. As shown in Fig. 6.2k, the transmittance of the AAO/PDMS contact lens is  $\sim 92\%$ . For comparison, the transmittance for eye glasses is  $\sim 85\%$  and for PDMS is  $\sim 95\%$ . These measurements indicate that the highly transparent AAO thin film is a suitable material to be integrated with the PDMS-based contact lens device with negligible effect on transparency. Nonetheless, a clear area of 4 mm in diameter at the central visual axis (i.e. in front of the pupil) is left without AAO thin film to allow even greater transparency. The effect of the mechanical deformation of the contact lens on its transmittance has also been evaluated. The measured transmittance under 1000-cycle bending and stretching is shown in Fig. 6.2l. After 1000-cycle bending and stretching, it has been found that the transmittance shows negligible changes and no cracks can be found in the AAO thin film, indicating its high mechanical flexibility and optical transparency suitable for an IOP sensor.

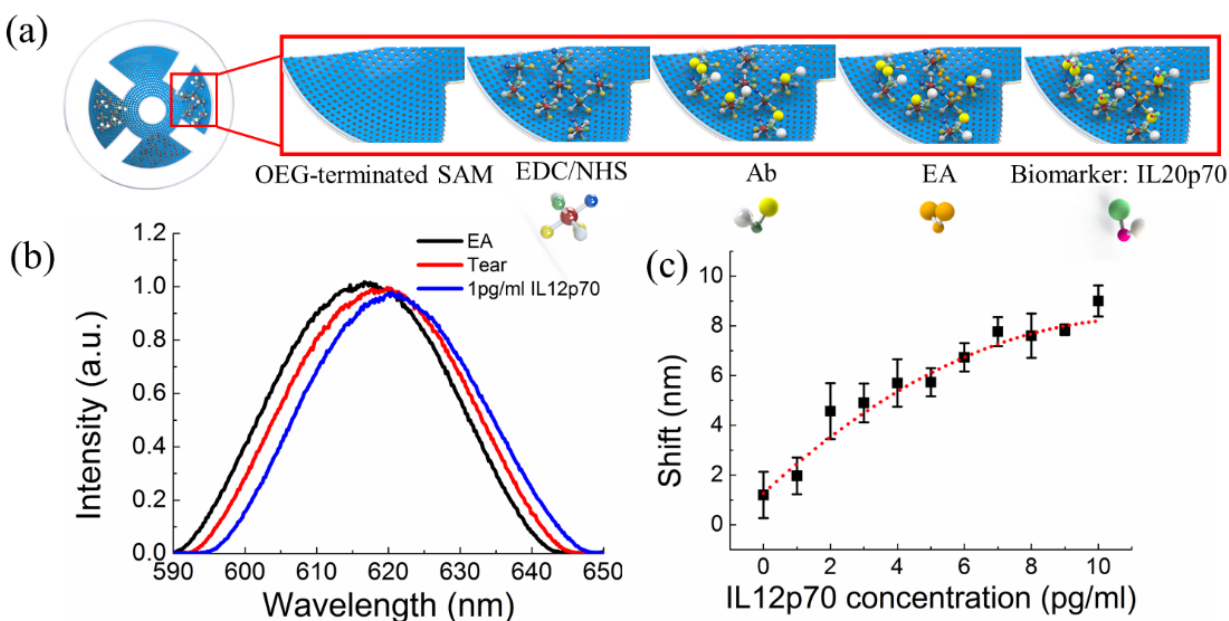


Fig. 6.3. (a) Schematic illustration of the chemical functionalization steps of the sensor surface for detecting biomarker IL20p70; (b) representative measured optical signals showing the optical signal shift after artificial tear and 1pg/ml IL 12p70 in artificial tear is applied on the contact lens sensor, respectively; (c) Measured signals for IL20p70 at different concentrations in artificial tear.

### **In Vitro Detection of Biomarker in Artificial Tears by Means of the Novel Contact Lens**

Biomarker detection in the tear film can assist the diagnosis of early glaucoma, which can potentially provide a complementary diagnosing method to the widely used IOP measurement method. To date, there are no known highly reliable liquid biomarkers for glaucoma diagnosis, even though many potential promising ones have been identified [20, 22-24]. One possible biomarker is cytokine Interleukin 12 (IL-12p70), since recent studies have found that the mean concentrations of IL-12p70 in tear film were significantly lower for the diagnosed primary open-angle glaucoma (POAG) group compared to the control group ( $3.94 \pm 2.19$  pg/mL in control vs  $2.31 \pm 1.156$  pg/mL in POAG;  $P=0.035$ ) [21]. This indicates that measuring the concentration of IL12p70 in the tear film could aid with the early diagnosis of glaucoma, in addition to IOP measurement. As aforementioned, quite a few promising biomarkers have been reported; ideally, all of them can be screened and validated in the tear film for accurate diagnosis. In this technical demonstration, we have only detected IL-12p70 by the nanopore thin film sensor embedded in the contact lens as an example. The same principle can be applied for other biomarkers by functionalizing different types of antibodies or aptamers on the sensor surface.

The biomarker is monitored by measuring the optical reflection signal from the nanopore thin film sensor embedded in the contact lens, similar to our previous work [30], before and after the biomarker is applied to the sensor. The binding of the biomarker with the functionalized surface of the sensor results in a change of the optical path difference (OPD). The higher the concentration of the biomarker, the larger the shift of the optical signal.

To this end, the surface of the sensor needs to be functionalized with human IL-12p70 antibody first. The detailed procedure is illustrated in Fig. 6.3a. The contact lens sensor surface coated with 10 nm Au is functionalized with human IL-12p70 antibody through 1-ethyl-3-(3-

dimethylaminopropyl) carbodiimide (EDC)/N-hydroxysulfosuccinimide (NHS) chemistry. Briefly, the sensor surface is immersed in the 10 mM HSC10COOH/HSC8OH overnight at 4 °C and then washed with pure ethanol and Millipore DI water. After the surface is dried, it is immersed in a mixed solution of NHS and EDC (NHS 0.2 M, EDC 0.05 M) for 2 hours. The sensor surface is then washed with DI water and immersed in the 5  $\mu$ M IL-12p70 antibody solution overnight. This is followed by applying 100 $\mu$ L 1 M ethanolamine (EA) to block the unoccupied HSC10COOH/HSC8OH sites activated by the EDC/NHS. Finally, the sensor surface is rinsed with the PBS buffer to remove non-specifically adsorbed proteins. At this stage, the sensor is ready for measuring the biomarker IL-12p70.

Mouse IL-12p70 diluted in artificial tears (TheraTears, Akron) with a concentration ranging from 0 pg/ml to 10 pg/ml was applied onto the sensor surface for 2 hours incubation in sequence, and the shifts of the reflected light were collected. As shown in Fig. 6.3b-c, by increasing the concentration of IL-12p70 from 0 pg/ml to 10 pg/ml, the shift increases from 1.2 nm to 9 nm. This indicates that the sensitivity of the contact lens sensor is  $\sim 0.78$  nm/(pg/ml) for IL-12p70 detection. Note that the shift of the artificial tears (0 pg/ml of IL-12p70) is 1.2 nm, indicating the possible non-specific binding of the minerals in the artificial tears with the antibodies of IL-12p70, which can be nulled by subtracting the shift due to the artificial tear.

## **Drug Release**

In previous studies, loading a drug to a contact lens was achieved by immersing a commercially available contact lens in a drug solution; hence, impregnating the lens with the drug. Drug release from the drug-impregnated lens was achieved by simple passive diffusion. Thus, drug release lasted for only a short period of time, from a few hours up to four days. In order to achieve an extended drug release, and especially maintain the release of a constant dose of the drug (within

the therapeutic range), the nanopores in the AAO thin film have been used to store the drugs, thereby enabling a sustained drug release and therapeutic effect. In this demonstration, Timolol, a widely used anti-glaucoma drug [15], was mixed with a fluorescein dye (fluorescein sodium saline: FSS) solution, and then loaded into the nanopores of the AAO thin film (Fig. 6.4a). The surface of the AAO thin film is hydrophilic due to a brief oxygen plasma treatment, which facilitates the load of the drug/FSS into the nanopores. Specifically, 500  $\mu\text{l}$  FSS is diluted into 10  $\mu\text{g}/\text{ml}$  and then mixed with Timolol, then the solution is applied onto the AAO thin film, allowing to air-dry under normal room conditions. After the surface is dried, the contact lens is immersed into artificial tear to mimic the aqueous environment of the ocular surface (i.e. tear film). Under this condition, the release of the drug/FSS is mainly by passive diffusion of the drug/FSS to the artificial tear [14]. As the drug/FSS is being released from the AAO thin film, the fluorescence intensity of the AAO thin film is decreased. At pre-determined time points (see below), the contact lens was removed from the artificial tear bath and imaged by a fluorescence microscope (Olympus, Inc.).

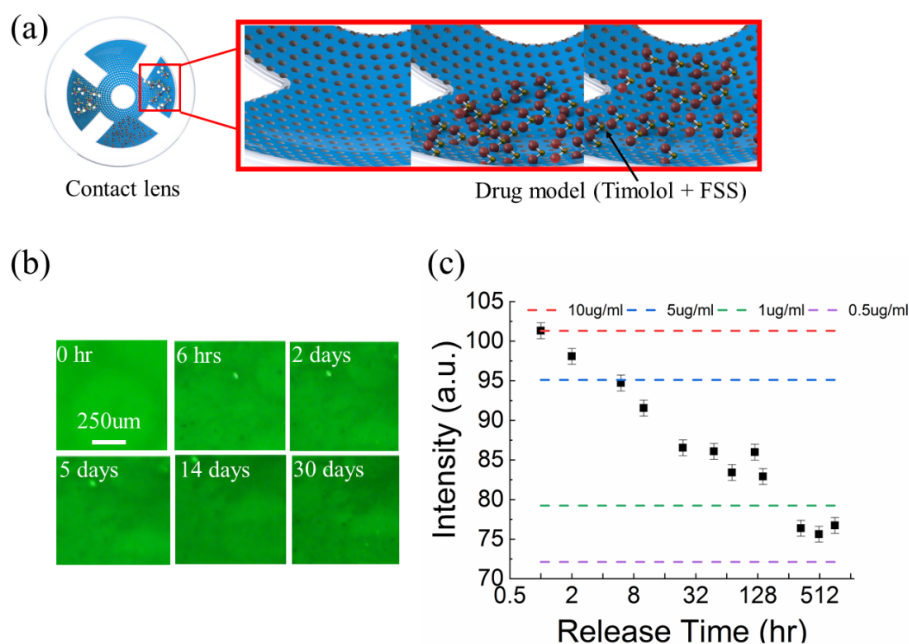


Fig. 6.4. (a) Sketch: drugs (timolol + FSS as drug model) loaded to the contact lens device and its close-up; (b) fluorescence images at different release time points; (c) fluorescence intensity and corresponding concentration of drug at different release time points.

A series of representative fluorescence images for different time points are shown in Fig. 6.4b. As shown in these images, the fluorescence intensity of the AAO thin film decreases gradually after being immersed into artificial tear for 6 hrs, 2 days, 5 days, 14 days, and 30 days, respectively, corresponding to the drug/FSS release into the artificial tear. The corresponding average fluorescence intensity was obtained by using the imaging analysis toolbox in Matlab, which is shown in Fig. 6.4c. As shown, after 30 days, the fluorescence intensity decreased  $\sim 25\%$ . In order to quantify the drug release over time, calibration experiments have been performed. In the calibration experiments, 10ug/ml, 5ug/ml, 1ug/ml, 0.5ug/ml, 0.1ug/ml FSS solution was applied onto the AAO thin film and fluorescence images were taken after the contact lens surface was allowed to air-dry under normal room conditions. The fluorescence intensity and its corresponding concentration range of FSS were then plotted to calculate the drug release over time (Fig. 6.4c). Our results show that  $\sim 90\%$  of the drug was released after 30 days. It is anticipated that if the drug has been totally released, the fluorescence intensity should be close to zero, given small fluorescence emission from AAO and PDMS [36]. These experiments prove that extended drug release from a contact lens device can be achieved by using nanopores as part of a contact lens device as a drug depot that allows long term drug release.

### **Ex Vivo Monitoring of Intraocular Pressure (IOP)**

As demonstrated previously, the flexible AAO nanopore thin film can be used as a pressure sensor [28]. It is well known that increased IOP is a major risk factor for, and one of the clinical signs of, glaucoma. Frequent measurement of IOP is therefore critical for diagnosing glaucoma and monitoring response to therapy. Herein, the ex vivo evaluation of IOP using a contact lens with AAO nanopore thin film is demonstrated. Changes in IOP lead to changes of corneal curvature. When a contact lens is applied onto the cornea, a change to the corneal curvature results

in a change to the contact lens curvature as well. This change in contact lens curvature will lead to a change in optical reflection, or a shift of signal, from the contact lens. Specifically, the light reflection angles from the contact lens is changed. Different reflection angles result in different optical paths and different interference spectrums. The IOP can be calculated as a function of spectrum shift (Fig. 6.5). In this part of the experiment, the reflection spectrum was measured from SCR sensors on the contact lens.

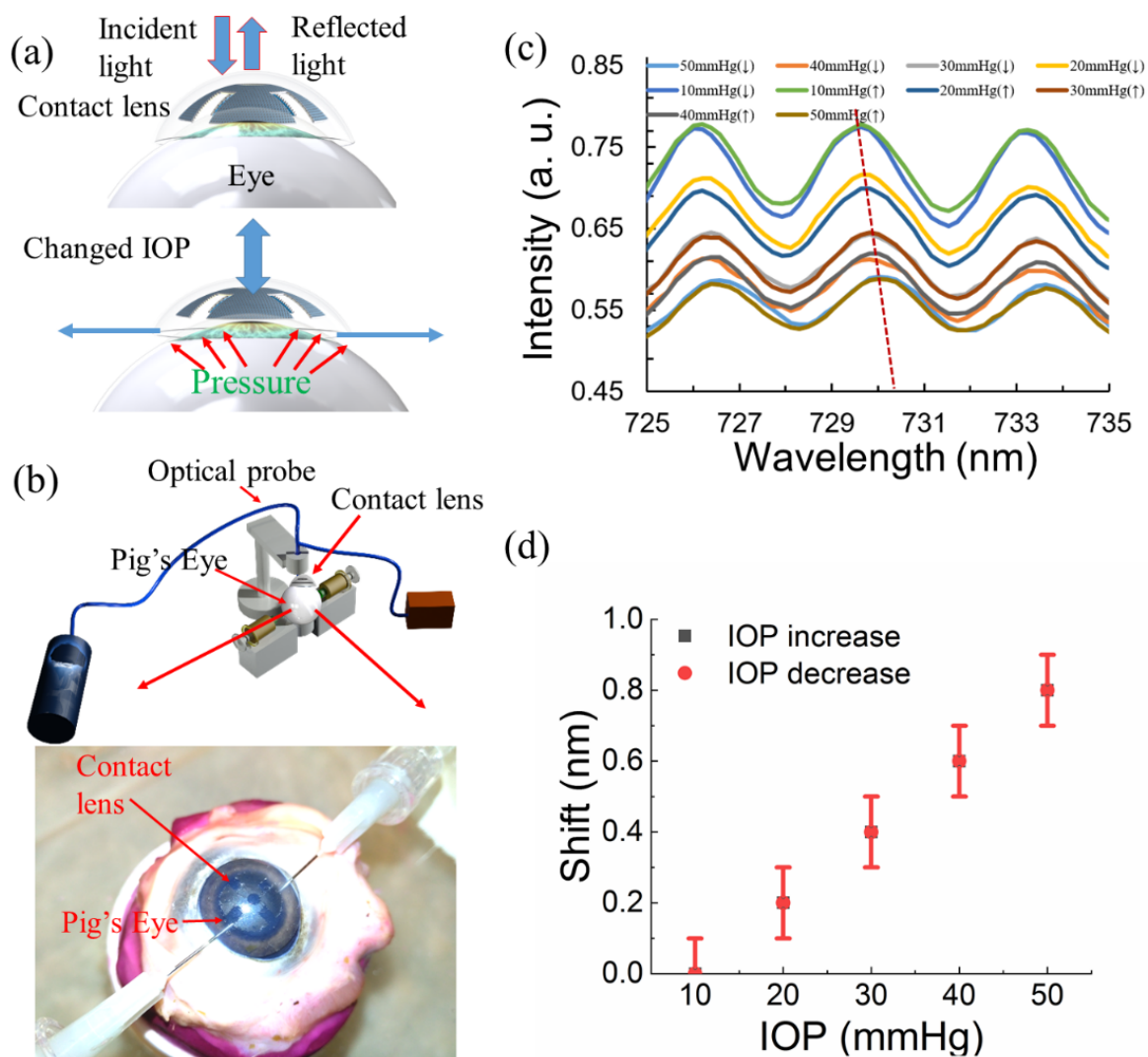


Fig. 6.5. (a) The change of corneal curvature due to IOP consequently leads to curvature change of the contact lens; as a result, the reflected optical signal from the contact lens changes; (b) Measurement setup: a contact lens is placed onto a cadaver pig's cornea, and signal shift is measured by means of an optical probe (Ocean Optics, Inc.); (c-d) measured optical signals with changing IOP, the IOP starting at 10 mmHg.

Manometry on a cadaver pig eye was used, as previously described [37], to evaluate the optical signal shift from the contact lens in response to IOP changes (Fig. 6.5b). Briefly, the cadaver eye was secured on a ring of clay at the same height as a digital manometer. The anterior chamber of the eye was cannulated at the limbus, at the 3 and 9 o'clock positions, using a 27-gauge needle. One needle was connected to a digital manometer and the other was connected to a 1 L 0.9% NaCl reservoir bag. Leakage around the needles was not observed following channelization of the anterior chamber. The IOP, controlled by adjusting the height of the reservoir bag, was increased from 10 to 50 mmHg at 10 mmHg intervals. The fabricated contact lens was applied onto the cornea and was repeatedly lubricated with physiological saline solution throughout the experiment.

An optical fiber probe (Ocean Optics, Inc.) connected to a spectrometer (Ocean Optics, Inc.) was then set up perpendicular to the contact lens to deliver illumination and collect light reflection (Fig. 6.5b). The spectrometer was connected to a computer which displayed and recorded the reflection spectrum. The results are shown in Fig. 6.5c: by increasing the IOP from 10 mmHg to 50 mmHg, the peaks of the reflection spectrum shifted by 0.8 nm to a longer wavelength. By decreasing the IOP from 50 mmHg to 10 mmHg, the peaks of the reflection spectrum shifted by 0.8 nm to a shorter wavelength. For both cases, measurements showed excellent repeatability for the spectrum shift. The contact lens IOP sensor has a sensitivity of 0.02 nm/mmHg (Fig. 6.5d), similar to that of a recently reported IOP sensor [25].

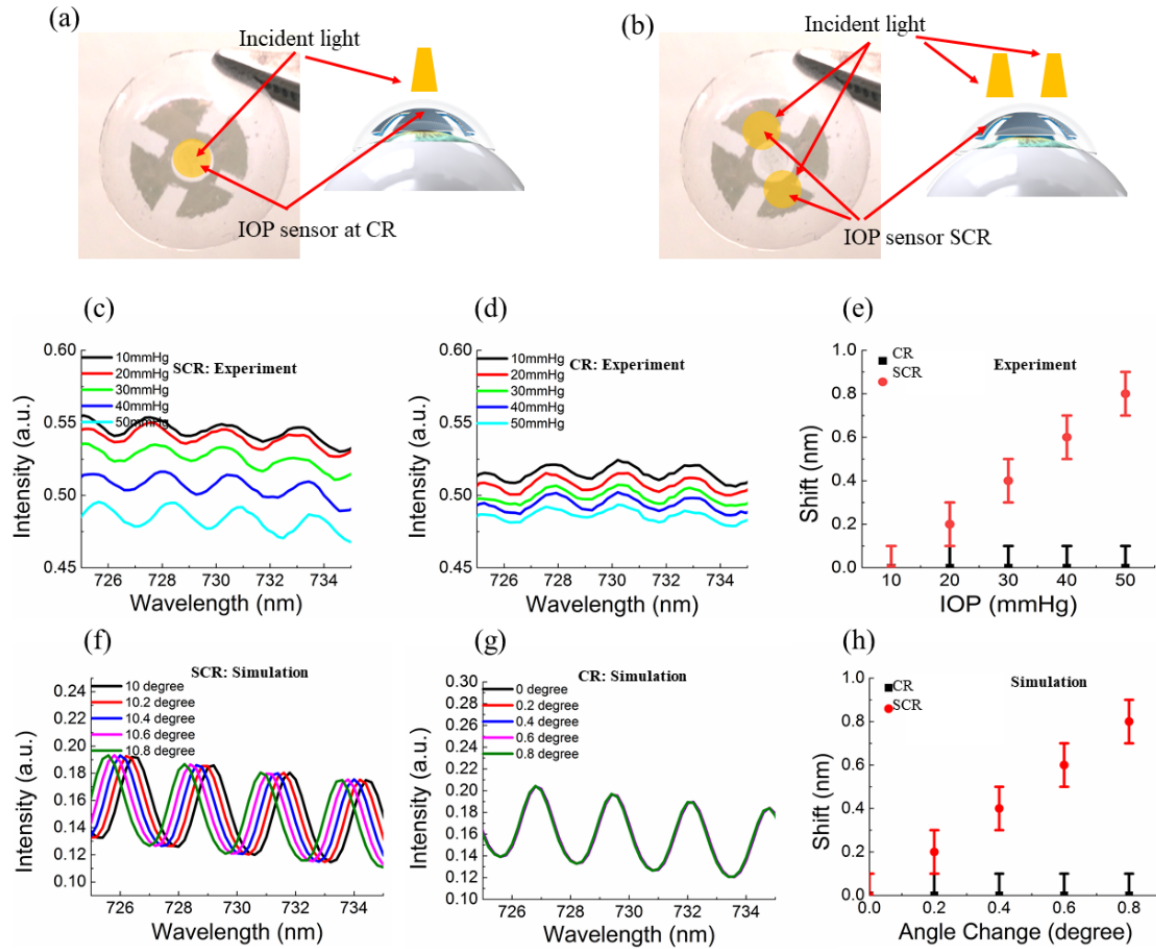


Fig. 6.6. (a) Sketch showing light path to the IOP sensor at the CR for the measurement; (b) sketch showing light path to the SCR IOP sensor for the measurement; (c) Measured optical signal from SCR IOP sensor on the contact lens; (d) Measured optical signal from the CR IOP sensor; (e) Measured shift of the optical signal under different IOPs for CR and SCR sensors; (f-h) the simulated results for CR and SCR IOP sensors under different IOPs (equivalent to different incident angle of incident light).

### IOP Sensors at the Central Region and Surrounding the Central Region on Contact Lens

In this section, the spectrum shift as a function of IOP was evaluated by CR and SCR sensors. The experimental design was similar to that described above and in Fig. 6.5. However, in this experiment, the reflected light was measured from sensors at the CR and SCR as illustrated in Fig. 6.6a-b. The results are presented in Fig. 6c-e. Our results indicate that the optical signals from the CR sensors show a very small shift as a response to IOP change, while a much larger shift was observed from the SCR sensors. The contact lens IOP sensor is essentially equivalent to an angular

sensor as demonstrated in our lab previously [28]. Hence, in the simulation, the responses of the contact lens were modeled by changing the incident angle of the light as shown in Fig. 6.6f-h, which matches the experimental results where the angle changes from  $0^\circ$  to  $0.8^\circ$ . These results suggest that the IOP sensors in the CR are less sensitive to the IOP changes than the SCR sensors. This is due to the fact that the IOP sensors in the CR have a much smaller curvature than that of the IOP sensors in the SCR. As a result, the incoming light to the SCR sensors has a larger incident angle than that of the sensors in the CR. In addition, the curvature in the CR changes much less than that of the SCR with the same change in IOP. Hence, the CR sensors are much less sensitive to IOP changes (i.e., smaller optical signal shift) than the SCR sensors.

### **Discussions and Conclusion**

The three functions of the smart contact lens have been demonstrated herein. It has been found that (1) one of the possible glaucoma biomarkers (IL-12p70) can be detected in artificial tears successfully; (2) the sustained drug release can last at least 30 days, and (3) the IOP can be monitored with excellent repeatability. Overall, the new smart contact lens device with the three functions opens the possibility for quantitative analysis of the protein biomarkers in tears, the repeated real-time IOP monitoring, and the extended in situ drug delivery.

For future in vivo biomarker evaluation in the tear for both healthy people and glaucoma patients, the procedure is summarized as follows. After the sensors on contact lens are functionalized with a specific antibody [24], it will be worn by a healthy people or a patient for one hour. Then, it will be removed from the eye and rinsed rigorously with buffer solution before taking the measurements. With different antibodies, the concentration profile of the proteins in tear film can be obtained as a function of time. This way, the possible biomarkers for glaucoma or other ocular diseases can be identified and validated. For the extended drug release, different drugs or a

combination of drugs can be loaded to the contact lens to examine their clinical efficacy. It should be noted that the release of drugs loaded into the contact lens can be further triggered by the IOP in glaucoma patients. In other words, the release rate of the drug is only dependent on the diffusion process if IOP remains within the normal range. However, the release rate will increase when the IOP increases since the contact lens will be stretched; as a result, the release rate from the nanopores will be increased. Similarly, the drug release rate will decrease when the IOP decreases. This drug release mechanism is similar to a strain-triggered drug release reported before [38], which means that the drug release rate of the contact lens device can be self-regulated based on the IOP, increasing the drug release (hence the dose) when the IOP spikes. Furthermore, we have concluded that the SCR IOP sensors should be used for IOP monitoring (rather than the CR sensors), as they are more sensitive to IOP changes.

It should be noted that while the IOP can cause the changes of the corneal curvature, other factors (eyeball swelling, eyeball temperature change, etc.) can also cause the same changes. Hence, the diagnosis of glaucoma cannot be very accurate by measuring IOP only. As demonstrated, the reported contact lens device can also measure the glaucoma biomarkers in tears. It is anticipated that by combining the IOP measurements and the glaucoma biomarker measurements, more accurate diagnosis of glaucoma can be achieved. In addition, for future in vivo IOP measurements or possible clinic use of this reported contact lens device, an optical reader and the related accessories also need to be developed.

### References

- [1] H. Quigley and A.T. Broman, "The number of people with glaucoma worldwide in 2010 and 2020," *British Journal of Ophthalmology*, vol. 90, no. 3, pp. 262-267, 2006.
- [2] Y.C. Tham, et al., "Global Prevalence of Glaucoma and Projections of Glaucoma Burden through 2040: A Systematic Review and Meta-Analysis," *Ophthalmology*, vol. 121, no. 11, pp. 2081-2090, 2014.
- [3] [https://www.optometrists.co.uk/examinations/Triggerfish\\_Glaucoma\\_monitoring\\_Contact\\_lens/](https://www.optometrists.co.uk/examinations/Triggerfish_Glaucoma_monitoring_Contact_lens/)

- [4] I. Araci, et al., "An implantable microfluidic device for self-monitoring of intraocular pressure," *Nature Medicine*, vol. 20, pp. 1074, 2014.
- [5] V. Çağdaş, Y. Shih, B. Otis, T. Shen and K. Böhringer, "A wireless intraocular pressure monitoring device with a solder-filled microchannel antenna," *Journal of Micromechanics and Microengineering*, vol. 24, no. 4, pp. 045012, 2014.
- [6] R. Haque and K.D. Wise, "A 3D implantable microsystem for intraocular pressure monitoring using a glass-in-silicon reflow process," in *2011 IEEE 24th International Conference on Micro Electro Mechanical Systems (MEMS)*, pp. 995-998, 2011.
- [7] M. Kouhani, A. Weber, and W. Li, "Wireless intraocular pressure sensor using stretchable variable inductor," in *2017 IEEE 30th International Conference on Micro Electro Mechanical Systems (MEMS)*, pp. 557-560, 2017.
- [8] L. Matteo, E. Pitchon, A. Bertsch, P. Renaud, A. Mermoud, "Wireless contact lens sensor for intraocular pressure monitoring: assessment on enucleated pig eyes," *Acta Ophthalmologica*, vol. 87, no. 4, pp. 433-437, 2009.
- [9] P. Chen, D. Rodger, S. Saati, M. Humayun, and Y. Tai, "Implantable parylene-based wireless intraocular pressure sensor," in *2008 IEEE 21st International Conference on Micro Electro Mechanical Systems (MEMS)*, pp. 58-61, 2008.
- [10] A. Heijl, M. Leske, B. Bengtsson, L. Hyman, B. Bengtsson, M. Hussein, "Reduction of intraocular pressure and glaucoma progression: Results from the early manifest glaucoma trial," *Archives of Ophthalmology*, vol. 120, no. 10, pp. 1268-1279, 2002.
- [11] M. Kass, D. Heuer, E. Higginbotham, C. Johnson, J. Keltner, J. Miller, R. Parrish II, M. Wilson, and M. Gordon, "The ocular hypertension treatment study: A randomized trial determines that topical ocular hypotensive medication delays or prevents the onset of primary open-angle glaucoma," *Archives of Ophthalmology*, vol. 120, no. 6, pp. 701-713, 2002.
- [12] P. Newman-Casey, A. Robin, T. Blachley, K. Farris, M. Heisler, K. Resnicow, and P. Lee, "The Most Common Barriers to Glaucoma Medication Adherence," *Ophthalmology*, vol. 122, no. 7, pp. 1308-1316, 2015.
- [13] J. Creech, A. Chauhan, and C.J. Radke, "Dispersive Mixing in the Posterior Tear Film Under a Soft Contact Lens," *Industrial & Engineering Chemistry Research*, vol. 40, no. 14, pp. 3015-3026, 2001.
- [14] C. Li, and A. Chauhan, "Modeling Ophthalmic Drug Delivery by Soaked Contact Lenses," *Industrial & Engineering Chemistry Research*, vol. 45, no.10, pp. 3718-3734, 2006.
- [15] C. Peng, A. Ben-Shlomo, E. Mackay, C. Plummer and A. Chauhan, "Drug Delivery by Contact Lens in Spontaneously Glaucomatous Dogs," *Current Eye Research*, vol. 37, no. 3, pp. 204-211, 2012.
- [16] X. Ding, C. Song, and L. Que, "Fabrication of contact lens device with integrated microtubes for in situ extended drug delivery for ocular disease treatment," *Proc. Transducers'2019*, pp. 306-309, 2019
- [17] J. Hillman, "Management of acute glaucoma with pilocarpine-soaked hydrophilic lens," *The British Journal of Ophthalmology*, vol. 58, no. 7, pp. 674-679, 1974.
- [18] L. Kerrigan–Baumrind, H. Quigley; M. Pease, D. Kerrigan, R. Mitchell, "Number of Ganglion Cells in Glaucoma Eyes Compared with Threshold Visual Field Tests in the Same Persons," *Investigative Ophthalmology & Visual Science*, vol. 41, no. 3, pp. 741-748, 2000.
- [19] A. Sommer, J. Tielsch, J. Katz, H. Quigley, J. Gottsch, J. Javitt, K. Singh, "Relationship between intraocular pressure and primary open angle glaucoma among white and black americans: The baltimore eye survey," *Archives of Ophthalmology*, vol. 109, no. 8, pp. 1090-1095, 1991.
- [20] R. Vohra, J.C. Tsai, and M. Kolko, "The Role of Inflammation in the Pathogenesis of Glaucoma," *Survey of Ophthalmology*, vol. 58, no. 4, pp. 311-320, 2013.
- [21] L. Agnifili, et al., Chapter 1 - Molecular biomarkers in primary open-angle glaucoma: from noninvasive to invasive, in *Progress in Brain Research*, G. Bagetta and C. Nucci, Editors. 2015, Elsevier. p. 1-32.
- [22] D. Gupta, J. Wen, J. Huebner, S. Stinnett, V. Kraus, H. Tseng, and M. Walsh, "Cytokine biomarkers in tear film for primary open-angle glaucoma," *Clinical Ophthalmology (Auckland, NZ)*, vol. 11, pp. 411-416, 2017

- [23] S. Hagan, E. Martin, and A. Enríquez-de-Salamanca, Tear fluid biomarkers in ocular and systemic disease: Potential use for predictive, preventive and personalized medicine. vol. 7. no. 1, pp. 15, 2016.
- [24] N. von Thun und Hohenstein-Blaul, S. Funke, and F.H. Grus, "Tears as a source of biomarkers for ocular and systemic diseases," *Experimental Eye Research*, vol. 117, pp. 126-137, 2013.
- [25] J. Kim, M. Kim, M. Lee, K. Kim, S. Ji, Y. Kim, J. Park, K. Na, K. Bae, H. Kim, F. Bien, C. Lee, and J. Park, "Wearable smart sensor systems integrated on soft contact lenses for wireless ocular diagnostics," *Nature communications*, vol. 8, pp. 14997, 2017.
- [26] J. Park, J. Kim, S. Kim, W. Cheong, J. Jang, Y. Park, K. Na, Y. Kim, J. Heo, C. Lee, J. Lee, F. Bien, J. Park, "Soft, smart contact lenses with integrations of wireless circuits, glucose sensors, and displays," *Science Advances*, vol. 4, no. 1, p. eaap9841, 2018.
- [27] C. Song, X. Che, and L. Que, "Nanopore thin film enabled optical platform for drug loading and release," *Optics Express*, vol. 25, no. 16, p. 19391-19397, 2017.
- [28] C. Song, X. Ding, and L. Que, "High-resolution, flexible, and transparent nanopore thin film sensor enabled by cascaded Fabry-Perot effect," *Optics Letters*, vol. 43, no. 13, pp. 3057-3060, 2018.
- [29] C. Song, P. Deng, X. Ding and L. Que, "A Flexible Nanopore Thin-Film-Enabled Device for Pressure Sensing and Drug Release," *IEEE Transactions on Nanotechnology*, vol. 17, no. 5, pp. 962-967, 2018.
- [30] C. Song, P. Deng, and L. Que, "Rapid multiplexed detection of beta-amyloid and total-tau as biomarkers for Alzheimer's disease in cerebrospinal fluid," *Nanomedicine: Nanotechnology, Biology and Medicine*, vol. 14, no. 6, pp. 1845-1852, 2018.
- [31] S. Feng, C. Chen, W. Wang, L. Que, "An aptamer nanopore-enabled microsensor for detection of theophylline," *Biosensors and Bioelectronics*, vol.105, pp. 36-41, 2018.
- [32] S. Alzghoul, M. Hailat, S. Zivanovic, L. Que, G. Shah, "Measurement of serum prostate cancer biomarkers using a nanopore thin film based optofluidic chip," *Biosensors and Bioelectronics*, vol. 77, pp. 491-498, 2016.
- [33] H. Yin, X. Li, and L. Que, "Fabrication and characterization of aluminum oxide thin film micropatterns on the glass substrate," *Microelectronic Engineering*, vol. 128, pp. 66-70, 2014.
- [34] G. Poinern, N. Ali, and D. Fawcett, "Progress in nano-engineered anodic aluminum oxide membrane development," *Materials*, vol. 4, no. 3, pp. 487-526, 2011.
- [35] H. Masuda and K. Fukuda, "Ordered metal nanohole arrays made by a two-step replication of honeycomb structures of anodic alumina," *Science*, vol. 268, no. 5216, pp. 1466-1468, 1995.
- [36] S. Cesaro-Tadic, G. Dernick, D. Juncker, G. Burman, H. Kropshofer, B. Michel, C. Fattinger and E. Delamarche, "High-sensitivity miniaturized immunoassays for tumor necrosis factor  $\alpha$  using microfluidic systems," *Lab on a Chip*, vol. 4, no. 6, pp. 563-569, 2004.
- [37] K. Tofflemire, C. Wanga, J. Jensb, N. Ellinwoodb, R. Whitleya, G. Ben-Shlomoa, "Evaluation of three hand-held tonometers in normal canine eyes," *The Veterinary Journal*, vol. 224, pp. 7-10, 2017.
- [38] J. Di, S. Yao, Y. Ye, Z. Cui, J. Yu, T. Ghosh, Y. Zhu, and Z. Gu, "Stretch-triggered drug delivery from wearable elastomer films containing therapeutic depots," *ACS nano*, vol. 9, no. 9, pp. 9407-9415, 2015.

## CHAPTER 7. GENERAL CONCLUSIONS AND FUTURE WORK

With all current work be done, two AD biomarkers have been successfully detected with label-free AAO biosensors. Contact lens targeting glaucoma diagnosis and treatment has also been fabricated and verified in prospective of proof of principle. To push such sensors to real life application, there is still way to go.

For the diagnosis of AD, the ultimate goal of AAO based microfluidics device will be to realize the point-of-care (POC) diagnostics. Toward this goal, several aspects need further studies and development in the future. The very first thing would be, when performing biomarker detection, plasma sample would be used instead of cerebrospinal fluids samples. This is mainly due to the much easier access of plasma sample rather than cerebrospinal fluid samples. However, biomarkers like A $\beta$ 42 and Ttau shows much lower concentration in plasma compared to cerebrospinal fluid. This would pose new challenge onto microfluidics devices in terms of sensitivity and detection of limit. Furthermore, there are other reported biomarkers related to AD such as pTau, which could result in tangles of helical and straight filaments, leading to similar consequences of A $\beta$ 42 deposition onto brain tissues.

For the development of contact lens device for glaucoma diagnosis and treatment, the first step work of multifunctional contact lens will be in vivo drug release test of this contact lens on animals, especially on dogs. This step is crucial because of its importance for potential realistic applications. The contact lens drug delivery method would replace tear drop drug delivery method in such experiments to perform longitudinal observation of treatment. Another improvement could be made to contact lens is the pressure sensing method change. In future design, several MEMS microstructures might be fabricated onto contact lens. By measuring the displacement of these

microstructures, pressure sensing could be realized. All these improvements can make the contact lens device more promising for future point-of-care (POC) measurement.

A mutual future work of AD and contact lens project is the development of smartphone based miniaturized measurement system. Such system can be used at home or the source-limited settings by the patients themselves with help from family members if needed, and is very critical for realizing point-of-care (POC) diagnostics. In addition, with such system, regularly repeated monitoring of AD and glaucoma under drug treatment can be realized.